AIAA 2024-2025 Undergraduate Team Aircraft Design

Final Design Report

Team Viserion - Lobo

Jack Whitehouse, Connor Gordon, Miles Walters, Madeline Rodriguez,
Patrick Swiatek, Nicholas Baker, Amber Miller, Daniel Mena

AE 443 - Aircraft Systems Design II

Department of Aerospace Engineering

University of Illinois at Urbana-Champaign

May 7, 2025

Team Member Contributions

Team Member	Primary Discipline(s)	Secondary Discipline(s)	AIAA Number	Signatures
Amber Miller	Stability and Control	Cost	1810996	
Connor Gordon	Aerodynamics	Low Observability, Acoustics/Emissions	1811059	
Daniel Mena	Systems	Avionics	1340952	
Jack Whitehouse	Team Lead	Configuration	1799606	
Madeline Rodriguez	Mass Properties	Ordnance	1809774	
Miles Walters	Structures, Loads and Dynamics	Landing Gear	1356622	
Nicholas Baker	Performance	Certification, Repair and Maintenance	1241848	
Patrick Swiatek	Propulsion	Interior/Payload	1404923	
Dr. Jason Merret	Faculty Advisor	-	155270	

Team Viserion

Dr. Jason Merret

Contents

Nomenclature

A	Cross-sectional or reference area (ft^2)
A_e	Nozzle exit area (ft^2)
A_t	Nozzle throat area (ft^2)
a	Speed of sound (ft/s)
b	Wingspan (ft)
c	Chord length (ft)
C_D	Coefficient of drag
C_L	Coefficient of lift
C_M	Coefficient of moment
CG	Center of gravity (in)
CG_{MAC}	Center of gravity as a percentage of MAC
Cp	Specific heat at constant pressure (BTU/lb-R)
Cv	Specific heat at constant volume (BTU/lb-R)
D	Drag force (lb)
d	Diameter (in)
δ	Stroke or deflection (in)
ΔP	Pressure difference (psi)
ΔT	Temperature difference (R)
Δt	Time step (s)
Δx	Distance increment (ft or in)
Δz	CG change along z-axis (in)
E	Modulus of elasticity (Young's Modulus) (GPa)
F	Force (lb)
F_x	X component of the resultant pressure force
F_y	Y component of the resultant pressure force
FH	Flight hours (hr)
g	Gravitational acceleration (ft/s^2)
h	Enthalpy (BTU/lb)
ho	Air density (slugs/ft^3)
I	Moment of inertia (in^4)
k	Thermal conductivity (BTU/hr-ft-R)
κ_p	Power coefficient of RAT
ksi	Kilopounds per square inch
L	Lift force (lb)
L/D	Lift-to-drag ratio
m	Mass (lbm)
M	Mach number
M	Moment
M_y	Bending moment (ft-lb)
$MTOW$	Maximum takeoff weight (lb)
N	Load factor
η	Efficiency
η_{tot}	Total efficiency
n	Polytropic or regression exponent (context dependent)
OEW	Operating empty weight (lb)
ϕ	Roll angle (deg)
P	Pressure (psi)
P_E	Euler buckling load (lb)
P_e	Electrical power (W or kW)
q	Dynamic pressure (psf)
Q	Heat transfer rate (BTU/hr)
R	Range (nmi)
ρ	Air density (slugs/ft^3)
Re	Reynolds number
r	Radius (in or ft)
S	Wing reference area (ft^2)
SFC	Specific fuel consumption (lb/lbf-hr)
SF	Safety factor
s	Entropy (BTU/lb-R)
σ	Stress (psi)
τ	Shear stress (psi)
t	Thickness (in)
T	Thrust (lb)
T_o	Ambient temperature (R)
T_t	Total temperature (R)
T_{inlet}	Turbine or inlet temperature (R)
TWR	Thrust-to-weight ratio
θ	Pitch angle (deg)
V	Velocity (kt)
V_{inlet}	Inlet velocity (ft/s)
V_{stall}	Stall speed (kt)
W	Weight (lb)
ω	Angular velocity (rad/s)
z	Distance from neutral axis (ft)
ψ	Yaw angle (deg)
$\dot{m}$	Mass flow rate (lbm/s)
$\dot{m}_{ox}$	Oxidizer mass flow rate (lbm/s)
$\dot{m}_{fuel}$	Fuel mass flow rate (lbm/s)
OF	Oxidizer-to-fuel ratio

Acronyms

AC = Alternating Current
$ACMP$ = Alternating Current Motor Pump
$AESA$ = Active Electronically Scanned Array
$AIAA$ = American Institute of Aeronautics and Astronautics
AIM = Air Intercept Missile
$AMRAAM$ = Advanced Medium-Range Air-to-Air Missile
APU = Auxiliary Power Unit
AR = Aspect Ratio
ATC = Air-Traffic Control
AVL = Athena Vortex Lattice
$BPCU$ = Bus Power Control Unit
$CA1$ = Combat Allowance 1
$CA2$ = Combat Allowance 2
CAD = Computer-Aided Design
CG = Center of Gravity
$COTS$ = Commercial-Off-The-Shelf
DCA = Defensive Counter-Air
DC = Direct Current
DRR = Design Readiness Review
ECU = Engine Control Unit
EDP = Engine Driven Pump
EPC = External Power Connector
EW = Empty Weight
FAA = Federal Aviation Administration
FCU = Fuel Control Unit
FEA = Finite Element Analysis
FL = Flight Level
GCU = Generator Control Unit
GE = General Electric
GPU = Ground Power Unit
IDG = Integrated Drive Generator
LOI = Letter of Intent
LFL = Landing Field Length
LRE = Launch & Recovery Element
MAC = Mean Aerodynamic Chord
MCE = Mission Control Element
$MTOW$ = Maximum Takeoff Weight
$NATO$ = North Atlantic Treaty Organization
NRV = Non-Return Valve
$OBIGGS$ = On-Board Inert Gas Generating System
PAO = Polyalphaolefin
PDI = Point Defense Interception
PDR = Preliminary Design Review
$PESA$ = Passive Electronically Scanned Array
PSF = Pounds per Square Foot
PTU = Pressure Transfer Unit
RAT = Ram Air Turbine
$RCCB$ = Residual-Current Circuit Breaker
RFP = Request for Proposal
RWR = Radar Warning Receiver
$SABR$ = Scalable Agile Beam Radar
SFC = Specific Fuel Consumption
$STBY$ = Standby
$TACAN$ = Tactical Air Navigation
$TOFL$ = Takeoff Field Length
TR = Transformer Rectifier
$TSFC$ = Thrust Specific Fuel Consumption
UAV = Unmanned Aerial Vehicle
UHF = Ultra High Frequency
UTS = Ultimate Tensile Strength
VHF = Very High Frequency
$VLOS$ = Visual Line of Sight
$WUTTO$ = Warm-Up Taxi Take-Off

List of Figures

List of Tables

Lobo Compliance Checklist

Requirement	Required Value	Lobo Value	Section Reference
RFP Requirements			
Dash Speed at 35,000 ft	Mach 1.6 and 1.2	Up to Mach 1.6	§6.H
Combat Air Patrol Endurance	Four hours	Mission One 4-hour loiter segment	§7.F
Remote Piloting	Required	Aircraft designed for remote operation	§14.B
Maintenance Accessibility	Required	Hatches/panels and ground equipment interfaces	§17
Max Load Factor (UTS)	+10.5 g, -4.5 g	+10.5 g, -4.5 g	§10.A
Max Load Factor (Yield)	+7 g, -3 g	+7 g, -3 g	§10.A
Structure Dynamic Pressure Withstand	2,133 psf (Mach 1.2 @ SL)	Designed for 2,133 psf with 1.5 safety factor	§10.A
Aircraft Durability	2,000 hr service life	2,000 hr service life	§17, §18.C
Fuel Requirements	JP-8 / Jet-A, self-sealing	Fuel system designed for JP-8, all tanks self-sealing with 11 mm clearance from fuselage	§13.C
Longitudinal Stability Margin	−10% to 10%	Mission CG paths within limits	§8.D
Takeoff Distance	≤ 8,000 ft	2,918 ft	§7.B
Landing Distance	≤ 8,000 ft	2,945 ft	§7.B
All-weather Operation	Required	OBIGGS, lightning wicks, sealed systems	§13.G
Intercept Mission Radius	200 nmi	425 nmi	§7.F
Missile Armament	AIM-120	2 x AIM-120	§15
Radar Type	AESA Radar	AN/APG-83 SABR AESA	§14.F
Launch and Recovery Method	NATO Runways	3.75 g-rated gear; 15° AOA clearance	§12
Engine Auxiliary Load	50 kW power, 2% mass flow	F110-GE-129 meets 50 kW under 2% flow constraint	§5.B
Flyaway Unit Cost	≤ $25M	$24M	§18
Derived Requirements			
Cruise Speed at 35,000 ft	Mach 0.9	Mach 0.9	§§6.H
Service Ceiling	≥ 50,000 ft	55,000 ft	§7.A
MTOW	≤ 32,000 lb	31,120 lb	§3, §11
Operational CG Envelope	40.06–62.14% MAC	42.2–61.0% MAC	§11
Max Braking Load	23,430 lb	23,430 lb	§10.C.3
Hydraulic System Redundancy	Dual + standby	A/B systems + standby + PTU	§13.D
Cooling System Capability	Handle avionics load	PAO liquid cooling + 30 cold plates	§13.F
Survivability after Damage	Retain structure/control	Composite layup, non-catastrophic frame damage	§9.D
RAT Emergency Power	≥ 50 kW @ 35k ft, 350 KTAS	50 kW	§13.G
Steering Radius	≤ 15 ft	10 ft	§12
Radar Cross Section (qualitative)	Reduced	Composite skin, angled fuselage	§2.C

Executive Summary, JW

The Lobo is a low-cost, high-performance unmanned interceptor designed in response to increasing threats to U.S. airspace and the need to supplement or replace legacy fighters reaching end-of-life by 2045. With modern adversaries fielding stealthy cruise missiles and high-speed aerial threats, the U.S. requires a rapid-response asset capable of patrolling domestic airspace at low operating cost while retaining high maneuverability and engagement capability.

Designed with affordability, survivability, and flexibility in mind, the Lobo is a swept-wing, single-engine aircraft with a maximum takeoff weight (MTOW) of 31,120 lb. It features a 30 deg swept wing, an F110-GE-129 engine, and remotely piloted fly-by-wire architecture. The aircraft carries two AIM-120 missiles and carries a 14,875 lb internal fuel load distributed across four discrete tanks for stability management and engagement range flexibility. The chosen propulsion system, the F110-GE-129, provides 29,000 lb of thrust and supports a dash speed of Mach 1.6.

The Lobo features capabilities including a maximum service ceiling of over 50,000 ft, sustained load factor of 7.0 g (10.5 g ultimate), and a maximum range of 1,200 nmi. Further, Lobo meets or exceeds all requirements outlined in the AIAA Request for Proposal (RFP) [1]. Current unit cost is estimated at $23.5M, below the $25M flyway requirement.

Developed to leverage commercial-off-the-shelf components such as the AN/APG-83 SABR radar for missile guidance, the Lobo blends survivability features such as recessed inlets and radar-deflective shaping enabling it to engage targets while maintaining a low radar cross-section.

Shown below, Fig. 1 provides a high level systems overview of the Lobo including the weapons systems, engine, landing gear, and control surfaces.

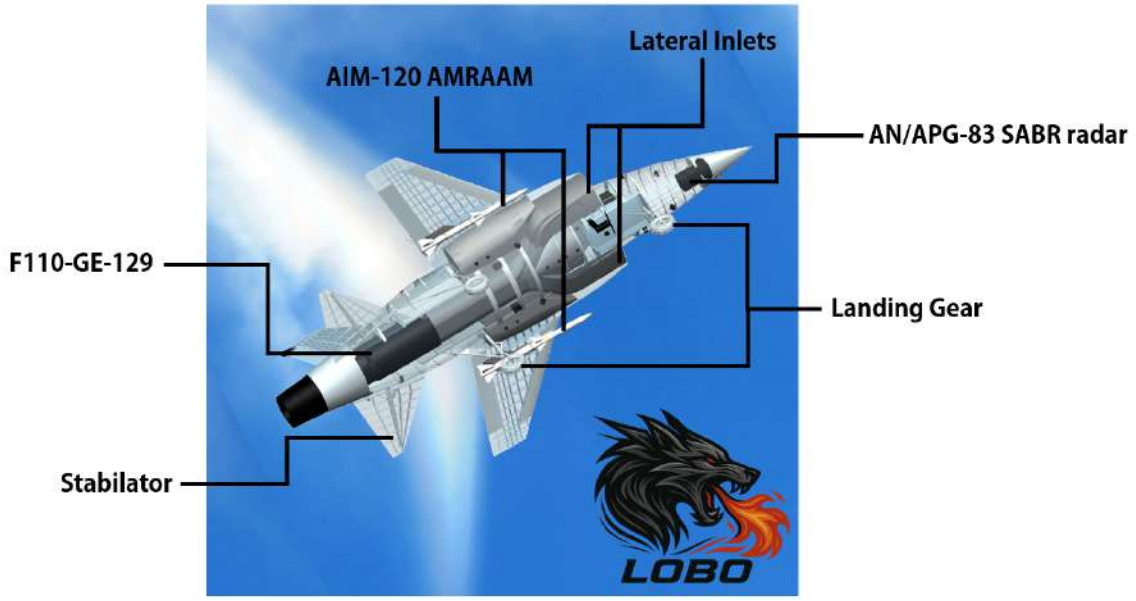

Fig. 1 Lobo executive diagram.

1. Introduction, JW

In light of rising global tensions and the expected retirement of current 4th generation fighter aircraft by 2045, the U.S. Air Force requires an affordable, rapidly deployable interceptor to defend domestic airspace from threats ranging from hijacked airliners to autonomous cruise missiles. The Lobo was designed in response to this need and mission. As a high-performance and remotely piloted interceptor, the Lobo can patrol, engage, and survive in contested airspace at a significantly reduced cost compared to manned alternatives.

About the Lobo

The Lobo is a unmanned, single-engine, blended-body interceptor with a 30 deg swept wing, fuselage-embedded F110-GE-129 engine, and internal fuel capacity of 14,875 lb. Its maximum takeoff weight is 31,120 lb, with a top speed of Mach 1.6 and operational ceiling above 50,000 ft. Armed with two AIM-120 missiles, the Lobo can engage a wide variety of threats while maintaining easily accessible internal systems for convenient repairs. The Lobo differentiates itself from other alternatives by including radar-deflective geometry, fly-by-wire remote piloting, and use of off-the-shelf systems like the AN/APG-83 SABR radar. This positions the Lobo to deliver mission capability at reduced cost and with minimal risk to both the platform and personnel.

Why the Lobo?

Our target customer is the Department of Defense, particularly the Air Force, who is seeking a cost-effective, scalable aircraft for homeland air defense and fleet supplementation. With an estimated unit cost of $23.5M, the Lobo meets all the requirements outlined in the AIAA RFP [1]. Further, a unique aspect of our design philosophy is our concentration on fleet-level capability, not just single aircraft performance. Each Lobo is intended to fly cooperatively with others in a network or formation depending on the mission needs. This enables the Lobo to improve target engagement by creating mutual sensor fusion with other Lobo aircraft or next generation air superiority vehicles. This approach allows for significantly improved operational flexibility in both peacetime deterrence and potential wartime operations.

Mission Capabilities

The Lobo program aims to produce 1,000 aircraft capable of widespread coverage of U.S. coastal airspace. The remotely piloted Lobo has been designed to achieve performance suitable for flexible deployment from existing NATO runways, shelters, and austere bases. The Lobo is capable of performing three primary missions: **Defensive Counter-Air (DCA) Patrol**, **Point Defense Interception (PDI)**, and **Intercept/Escort**. The primary mission objective of the Lobo is to quickly and flexibly respond to a variety of combat scenarios, shielding high value targets without concern for operator safety.

Lobo Configuration

Table 2 summarizes the finalized sizing characteristics for the Lobo, including wing geometry, weight breakdowns, and performance metrics. These results are the product of configuration trade studies, aerodynamic analysis, and propulsion-performance iteration. An isometric rendering of the Lobo is shown in Fig. 2 for visual reference.

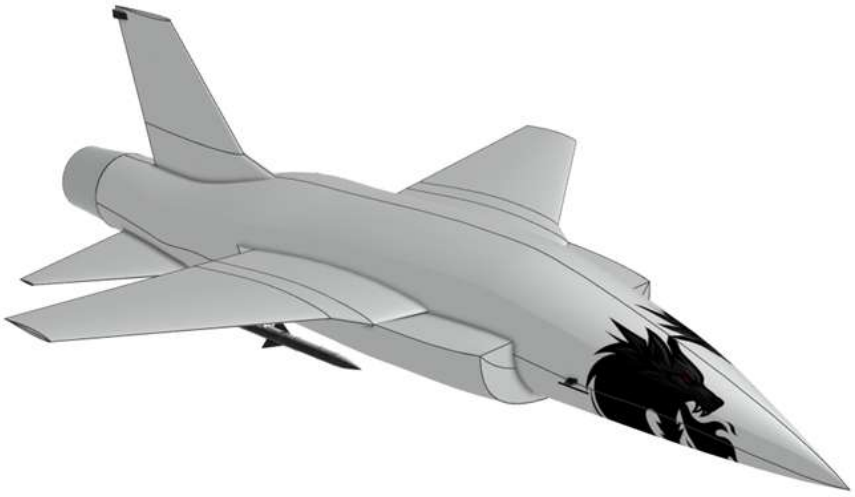

Fig. 2 Rendering of Lobo interceptor.

Table 2 Lobo Configuration and Sizing

Parameter	Value	Justification
Wingspan (b)	32.5 ft	Designed to allow carrier operations in future variants
Reference Wing Area (S_{Ref})	276 ft^2	Chosen by weight optimization trade study and similarity analysis
Aspect Ratio (AR)	3.79	Adjusted to improve performance and decrease fuel sizing requirements
Overall Wing Sweep (Λ)	30 deg	Chosen based on similarity to improve supersonic wave drag controllability
Taper Ratio (λ)	0.25	Adjusted via similarity analysis to minimize wing weight
Fuselage Length (L_{fus})	47 ft	Chosen to provide systems integration volume based on similarity analysis
Horizontal Tail Area (S_{ht})	104 ft^2	Based on static margin, control and pitch stability requirements
Vertical Tail Area (S_{vt})	108 ft^2	Based on control requirements and yaw stability analysis
Nominal Takeoff Distance	1,370 ft	Derived from performance calculations and minimized
Landing Distance	5,320 ft	Derived from performance calculations and minimized
Cruise Mach Number	0.85	Chosen to minimize fuel burn during cruise
L/D_{max}	12.5	Efficiency requirement for loiter and takeoff
$C_{L,max}$	2.05	Derived from aerodynamic analysis including high lift devices
Sea-level SFC	0.875	Derived from engine selection
Empty Weight	15,570 lb	Derived from weight calculation in performance tool
Maximum Takeoff Weight	31,120 lb	Weight estimation based on structural weights and fuel volume requirements

2. Concept of Operations, JW CG

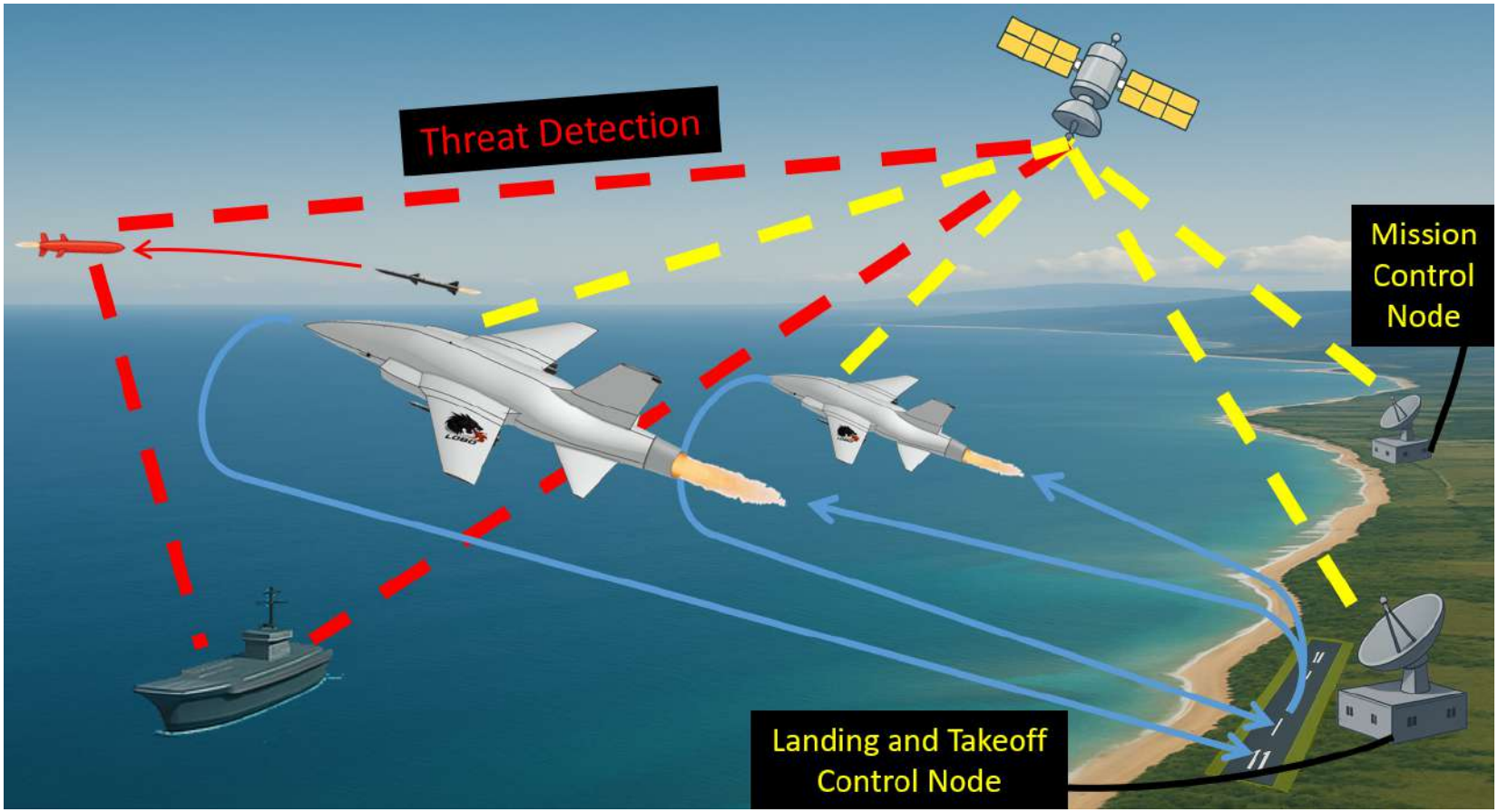

Fig. 3 Lobo OV-1 diagram.

Above, Fig. 3 presents the Lobo's high level concept of operation diagram, which includes mission launch from a NATO airbase, airborne handoff to the MCE, cruise, engagement of hostile targets, and recovery.

A. Requirements

The AIAA RFP [1] provides a set of requirements the Lobo must meet to ensure mission success. These are categorized as RFP specified vehicle or mission requirements and those derived from operational or system constraints. Tables 3 and 4 list these categories respectively.

Table 3 RFP Requirements and Design Impacts

Requirement	Value	Design Impact
Dash Speed at 35,000 ft	Mach 1.6 and 1.2	Drove selection of the F110-GE-129 engine and swept wing configuration
Combat Air Patrol Endurance	Four hours	Influenced internal fuel tank total volume and segmentation along with aerodynamic optimization for minimum loiter fuel burn
Remote Piloting	Required	Drove inclusion of VHF/UHF satellite links, quantum-resistant encryption, and dual ground stations
Maintenance Accessibility	Required	Informed access hatch locations and system layout
Structural Load Factors	+7 / -3 g, F.S. = 1.5	Drove structural design and material selection
Dynamic Pressure Tolerance	2,133 psf	Constrained inlet and structure design for low-altitude flight
Aircraft Durability	2,000 hr service life	Informed material selection, stress analysis assumptions, and maintenance costs
Fuel Requirements	JP-8 / Jet-A, self-sealing	Constrained fuel system materials, fuel volume percentage, and tank design
Longitudinal Stability Margin	-10% to 10%	Required static stability or stability control via advanced flight computer
Runway Compatibility	Operate from NATO 8,000 ft runways	Influenced landing gear, and landing/takeoff performance requirements
All-Weather Capability	Required	Influenced ECS design and sensor robustness
Flyaway Cost	$25M (Target)	Simplified structure and low empty weight target, limited ordnance and systems total cost; current flyaway cost is $22.3M
Intercept Mission Radius	200 nmi	Informed fuel volume and propulsion efficiency tradeoffs
Weapons Carriage	AIM-120	Defined ordnance type and informed wing structure at hardpoint locations
Engine Auxiliary Load	50 kW power, 2% mass flow	Affected engine sizing

The most challenging RFP requirement remains the cost target of $25 million. This constraint impacted every design decision and subsystem. The cost of avionics, landing gear, ordnance, structural design, materials selection, manufacturing and maintenance, etc. were in the forefront of every decision made in designing the Lobo in order to meet this requirement.

Table 4 Derived Operational Requirements and System Constraints

Requirement	Description	Design Impact	Derived From
Fuel System Redundancy	Crossfed tanks with dual pumps and NRVs	Increases survivability under combat damage	MIL 516C 8.3.4
Maintenance Accessibility	Tool-less panel access to systems and engine	Reduces downtime and supports <$25M flyaway cost	Maintainability Cost Target
Avionics Cooling Requirement	Must cool sensors and processors during long loiter	Led to PAO liquid cooling system integration	MIL 516C 12.1.2
Battery Emergency Power	Must power all systems for descent and landing from service ceiling	Dictated battery sizing and placement	MIL 516C 12.1.1
Visual Situational Awareness	Pilot must maintain situational awareness without cockpit visuals	Necessitated inclusion of DAS cameras	MIL 516C 11.1.1.5 / 11.1.2
90° Roll in Under 1.3 s	Required for maneuverability and directional control	Drove aileron and tail sizing	MIL-HDBK-1797
Crosswind Landing Capability	Must land with 11.5° sideslip and asymmetric load	Drove rudder sizing and vertical tail authority	Roskam / Raymer Stability
Takeoff Rotation Capability	Must rotate at VR during takeoff roll	Drove stabilator authority and CG constraint	Roskam / Nelson
Low OEW Priority	OEW must be minimized for convergence in required fuel sizing	Influenced structural simplification and GFE use	Performance Convergence

B. Operations

Figure 5 illustrates the execution of each mission profile for the Lobo. After takeoff and climb to cruising altitude, the Lobo can perform one of the three primary missions outlined in Fig. 4. During DCA Patrol, the Lobo loiters at 35,000 ft for up to four hours, monitoring the airspace for threats. For PDI, the Lobo dashes at Mach 1.6 to intercept and neutralize incoming threats within a 200 nmi radius. In the Intercept/Escort mission, the Lobo provides protection for high-value assets over a 300 nmi range. After completing a mission, the Lobo returns to base, lands, and prepares for its next engagement.

The Lobo is designed to operate in coordinated three-aircraft teams to for improved mission effectiveness, survivability, and adaptability to evolving threats as shown in Fig. 5 point 11. Each team can consist of a combination of three of the following loadouts depending on mission requirements:

- **Lead Strike**: A fully fueled Lobo tasked with initiating engagement on the target before they can get near U.S. soil, equipped with advanced radar and 2x AIM-120 AMRAAM Missiles.
- **Agile Support**: A lighter, more maneuverable Lobo with decreased fuel capacity for quicker roll and turn rate and quick response to nearby emerging threats or in case of escalation.
- **Loitering Support**: A high-endurance Lobo stationed at a safe standoff distance, providing the ground station with real-time threat monitoring, targeting pod for assisting next generation fighters, and reserve firepower if escalation is required.

As a result, the Lobo can then achieve formations that allows for various engagement strategies.

Fig. 4 Mission Profile Tables

((a)) DCA Patrol Mission Profile

Phase	Segment
WUTTO	Payload Loading
1-2	Taxi and Takeoff
2-3	Climb to FL350
3-4a	Cruise 300 nmi (FL350)
4a-4b	Patrol (FL350)
4b-4c	Dash 100 nmi (FL350)
4c-4d	CA1 at FL350
4d-4e	CA2 at FL350
4e	Payload Drop
4e-7	Cruise Back 200 nmi (FL350)
7-8	Cruise Back 200 nmi (FL350)
8-9	Descent
9-10	Reserves (30 min @ SL)

((b)) PDI Mission Profile

Phase	Segment
WUTTO	Payload Loading
1-2	Taxi and Takeoff
2-3	Climb to FL350
3-5a	Dash Out 200 nmi (FL350)
5a-5b	CA1 at FL350
5b-5c	CA2 at FL350
5c	Payload Drop
5c-7	Cruise Back 200 nmi (FL350)
7-8	Cruise Back 200 nmi (FL350)
8-9	Descent
9-10	Reserves (30 min @ SL)

((c)) Intercept/Escort Mission Profile

Phase	Segment
WUTTO	Payload Loading
1-2	Taxi and Takeoff
2-3	Climb to FL350
3-6a	Dash Out (FL350)
6a-6b	Escort 300 nmi (FL350)
6b-7	Accelerate
7-8	Cruise Back 200 nmi (FL350)
8-9	Descent
9-10	Reserves (30 min @ SL)

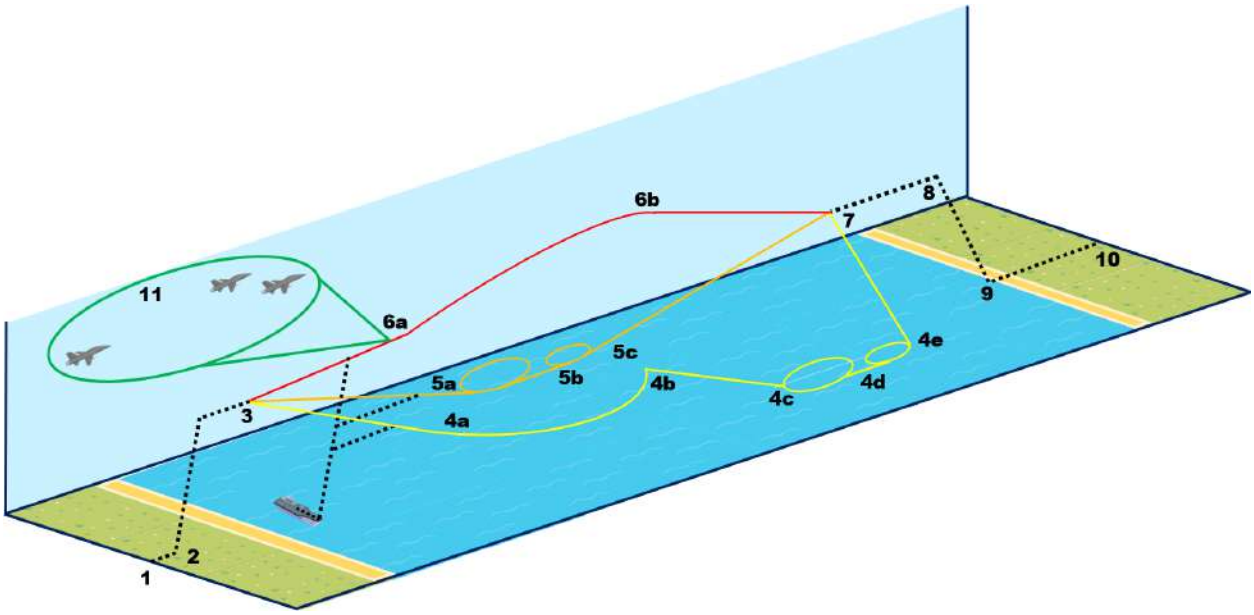

Fig. 5 Concept of operations diagram.

C. Low Observability

In its role as an interceptor capable of neutralizing a multitude of threats, from large chartered or hijacked jets to small cruise missiles, it is necessary for the Lobo to address these threats without disruption. For this to occur, the Lobo must be able to advance within combat range of a threat without being detected. With the advent of more advanced aircraft capable of entering United States' airspace and threatening national security, it is crucial the Lobo must take measures against these threats. To do this, the Lobo is designed to have a minimal radar cross-section, allowing the Lobo to safely advance to within combat range. The powerplant utilizes a bypass ratio of 0.74, which helps to reduce the thermal signature compared to a turbojet engine. Additionally, lateral inlets are utilized to prevent the thermal signature of the powerplant from being visible from the front of the aircraft. To assist in preventing detection on enemy radar, a leading-edge wing sweep of 40 deg provides minimal radar reflection of the wing. The integrated systems onboard the Lobo were also placed using low observability considerations, including a radar tilt 15 deg upward to minimize the Lobo's radar cross section.

Although not designed to engage with advanced fifth-generation fighter aircraft, the Lobo's low observability provides it with the capacity to deter these threats by advancing to within combat range undetected. The Lobo will have the ability to ambush an enemy fighter, which is effective in fleet formation. Although one Lobo is not capable of engaging with a fifth-generation fighter, multiple aircraft catching a threat off guard would be able of preventing it from advancing on national airspace, providing distraction until advanced allied interceptors can provide backup. To ensure the Lobo could reasonably distract a threat, it is capable of high speed maneuvers, including a high rate of climb and a fast instantaneous turn rate.

The Lobo's low observability allows it to operate in tandem with the United States' advanced fighters, providing more support and firepower without compromising the fighters' location.

D. Alternative Use Cases

Beyond its primary mission profiles, the Lobo offers significant operational utility and is capable of deploying in alternative roles as either a designed variant, or simply outfitted with a different loadout.

1. Carrier-Based Operations

The Lobo's wingspan and length, sea level thrust capability, and short takeoff performance lends itself well to the potential of a naval variant. Capable of utilizing carrier elevators and satellite communication links, a naval variant of the Lobo would expand its deployment capabilities beyond homeland defense operations. Outfitted with reinforced landing gear and an arrestor hook, this Lobo could conduct interception missions from a carrier deck, significantly shortening the time to intercept as can be seen in Fig. 5. Further, a Navy variant Lobo would be capable of operating in a fleet defense role, rapidly responding to airborne threats during operations in foreign waters. The ability to operate

from carriers significantly would extend the Lobo's operational envelope, allowing it to support naval and joint force missions in the future. However, enabling carrier operations would introduce several design challenges. The Lobo's structure would require reinforcement to withstand the high sink rates and arrestment loads of carrier landings, and its landing gear would need to be redesigned for durability and integration of a tailhook. As a result, we estimate that a navalized Lobo variant would incur an increased flyaway cost of approximately $27M.

2. High-Speed Reconnaissance

Without modification however, the Lobo's high-speed capabilities and advanced sensor suite lend itself well for tactical reconnaissance missions. With a reduced or removed payload for improved range and maneuverability, the aircraft can quickly investigate enemy airspace to gather real-time intelligence and identify threats, all without taking the risk of a pilot's life. This role is particularly beneficial for pre-strike reconnaissance, battle damage assessment, or locating targets.

3. The future of the Lobo

The Lobo was designed with these alternative use cases in mind in order to secure long-term relevance across multiple regimes of operation. The Lobo's airframe, systems architecture, and future use cases ought not be limited to a single mission type, but serve as a platform for the future expansion of remotely piloted air superiority. This flexibility improves the program's return on investment by enabling the same airframe to be deployed in homeland defense, naval fleet defense, or high-speed reconnaissance missions with minimal design modification. It also strengthens the case for procurement by different branches of the military by opening the door for joint-service adoption and increased production volume - lowering overall costs. By supporting varied missions in the future, the Lobo helps reduce the number of specialized aircraft required in the service, ultimately lowering training, maintenance, and logistics overhead.

3. Vehicle Sizing, JW NB AM

A. Similarity Analysis

The first task performed by the team to begin the design of an Lobo was the preliminary design and geometry sizing. Similarity analysis was performed on several interceptor vehicles including historical aircraft as well as pilotless aircraft beginning to enter the market. The aircraft selected for this analysis were the General Dynamics/Lockheed Martin F-16C Eagle, the Northrop F-5E Tiger, and the Anduril Fury. The F-16C was chosen as it is currently the smallest and least expensive fighter in service by the United States Air Force, the target customer. The F-5E Tiger was selected due to its small size, maneuverability, and supersonic capabilities. The final aircraft selected for this similarity analysis was the Anduril Fury, a fully autonomous fighter jet, scheduled to begin manufacturing in 2026. The Fury was selected due to its low cost and remote piloting, as those are requirements for the design of the Lobo. The F-16C and F-5E are both

fully capable of meeting the interception performance requirements for the RFP, so the sizing of these aircraft is relevant to wing design. Although the Fury is not capable of supersonic flight, it is included due to its potential to represent the future of military aircraft. For each of these aircraft, the wingspan, reference area (S_{Ref}), aspect ratio (AR), wing sweep, airfoil, taper ratio, and fuselage length were found. These results are shown below in Table 5. These results were then corroborated through the sizing analysis tool developed for the Lobo.

Table 5 Similarity Analysis Aircraft Parameters

Aircraft	**F-16C** [2]	**F-5E** [3]	**Fury** [4]
Wingspan (ft)	31.0	26.7	17.0
Reference Area S_{Ref} (ft^2)	300	186	50
Aspect Ratio (AR)	3.20	3.86	5.75
Sweep (°)	50	24	30
Airfoil	NACA 64A204	NACA 65A004.8	–
Taper Ratio	0.28	0.19	0.20
Fuselage Length (ft)	49.3	47.4	24.0
Wingspan/Fuselage Ratio	0.63	0.56	0.71

Additionally, similarity analysis was conducted during the selection process of the design's engine. While a more in-depth analysis is provided in the propulsion section of the report, the F110-GE-129 engine was ultimately selected due to it having a bypass ratio within the desired range, afterburners, a low dry and wet TSFC value, and the capability to be scaled up to reach dry thrust requirements.

B. Lobo Sizing Tool

A sizing tool was used to create the basis for the first design iteration for the Lobo. This was created using the F-16C as a seed aircraft. Preliminary design equations from Raymer [5] were used to estimate the weight and performance of a new aircraft. A simple sweep over wing area and aspect ratio was conducted. Contour plots were created for empty weight and ramp weight and are shown in Fig. 6. It can be seen that a wing area of 250 ft^2 and an aspect ratio of 4.0 minimizes empty weight. Ramp weight is minimized by a wing area of 500 ft^2 and an aspect ratio of 5.0. The RFP [1] has a constraining requirement that the aircraft cost must be below 25 million USD. This means empty weight should take high precedence to minimize building costs. Operating costs should also be a major consideration, so fuel weight or ramp weight should also be minimized in conjunction with empty weight. The team was able to formulate a first design iteration based on this data and information from the similarity analysis. The current design is just outside what is considered possible based on the preliminary sizing. This indicates that as the team moves through design iterations using higher fidelity estimation methods, the group can move away from using the preliminary data.

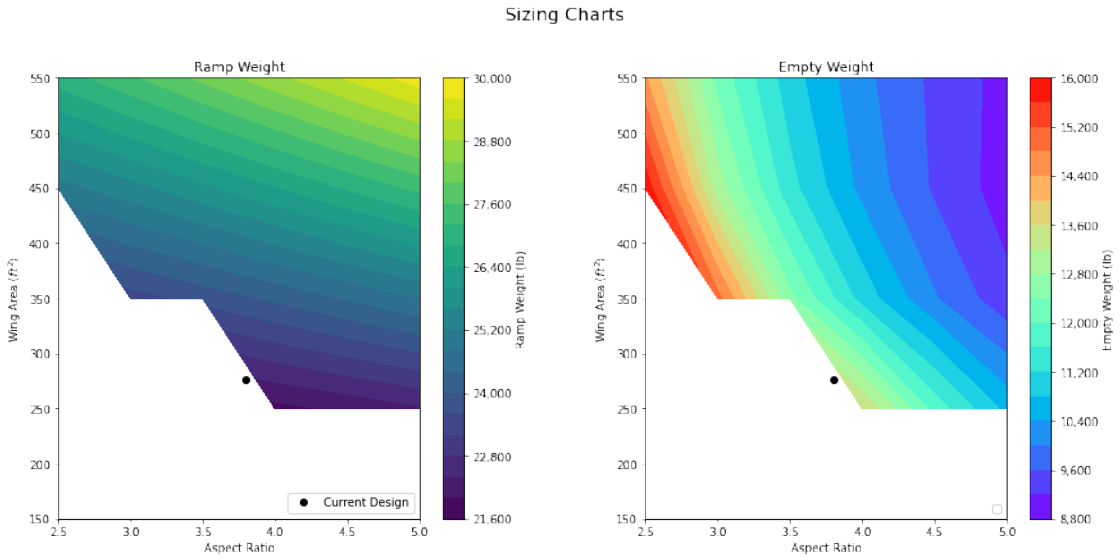

Fig. 6 Initial sizing charts.

It is also important to visualize the requirements. This can be done by the use of a constraint diagram. This diagram is shown in Fig. 7. This graph is created by using the basic equations associated with the requirements, rearranging them to have $\frac{T}{W}$ and $\frac{W}{S}$ as the variables. Basic constraints like TOFL, LFL, cruise, dash, and climb can be plotted. It can be seen that the current design is within the feasible region of the graph. Another item to note is that for future refining of the design, the team can look to move the design to the corners of the feasible region marked on the diagram. These points represent points that minimize the aircraft weight.

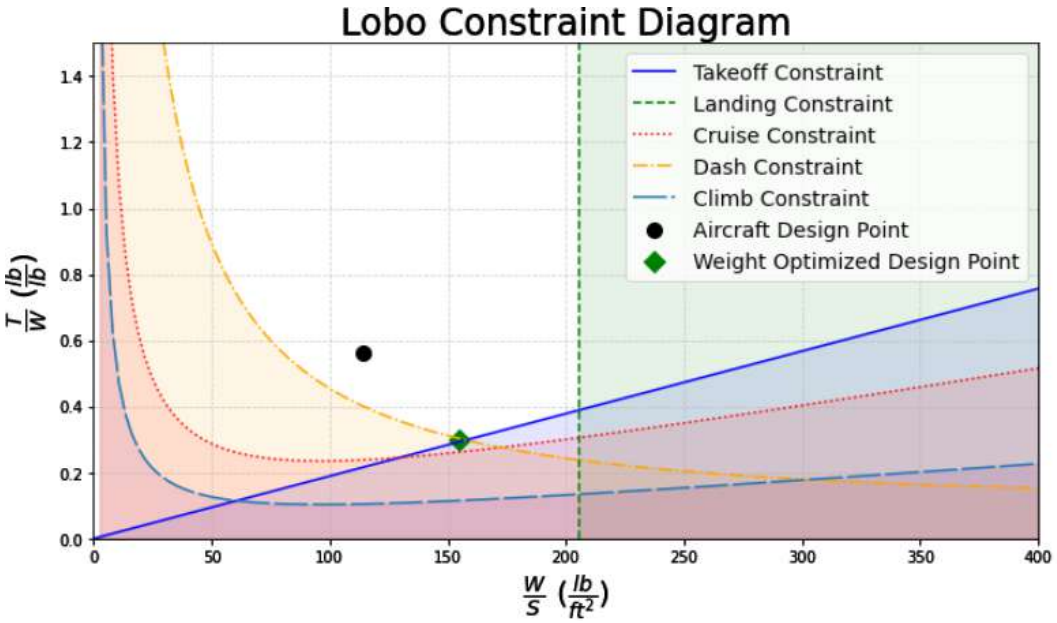

Fig. 7 Constraint diagram.

C. Trade Studies

A trade study was done on the wing sweep and wing taper ratio. This was conducted by using the existing geometry of the aircraft and sweeping through the possible values of sweep and taper. Starting with the wing sweep, it was found that lower values for wing sweep deliver lower EWs and lower MTOWs. Changing the value of wing sweep that is currently set at 30 deg to zero deg in fact reduces the empty weight of the aircraft by about 300 lb. This is due to the fact that the only place wing sweep shows up in the sizing tool is in the wing weight equation. This analysis was done in conjunction with a separate aerodynamics study. Even though lower values of wing sweep come back with lower weights, the analysis does not account for wave drag. Shock formation simulations for the aircraft showed that under 25 deg of wing sweep, the wing would be within the shock created by the nose for a Mach number of 1.6. The group ended with a wing sweep of 30 deg due to this trade study. This can be visualized in Fig. 8.

Another trade study that was conducted was on taper ratio. Similarly, the lower the taper ratio is, the lower the EW and MTOW will be. This is because the taper ratio is a major driver in the wing weight equation. This means that if the taper ratio is reduced from 0.25 to nearly zero, the empty weight decreases by 500 lb. This has to be taken into consideration in conjunction with structures considerations however. A very small taper ratio could make it difficult to design a structurally sound wing tip. A similarity analysis was conducted, and it was determined that a taper ratio of less than 0.2 was not practical. The group landed on a value of approximately 0.29 to maximize weight saving while minimizing future structural design concerns. The resulting data point of this trade can be seen in Fig. 8.

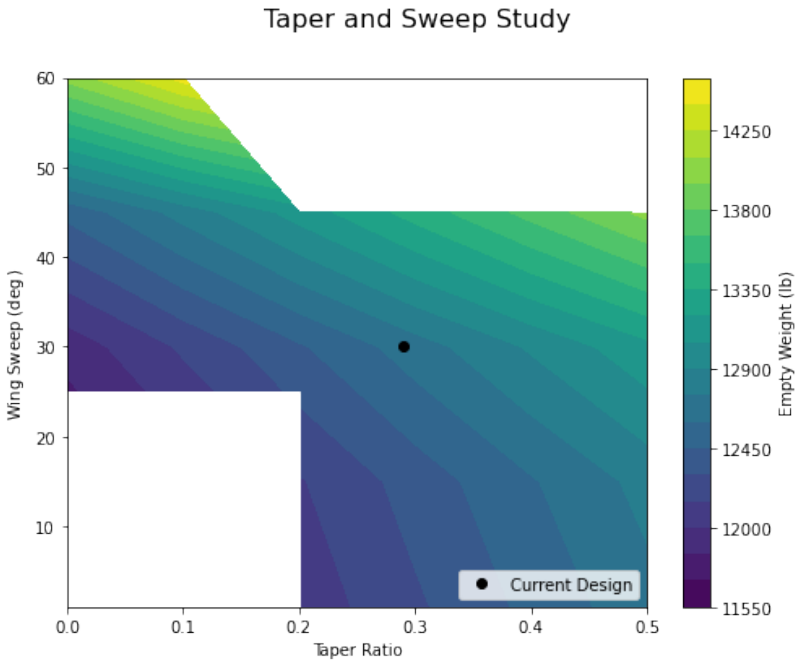

Fig. 8 Empty weight study for wing taper ratio and wing sweep.

D. Tail Sizing

Using equations from Roskam Part Seven [6] and data from the Mass Properties and Stability and Control sections, scissor diagrams were generated for each segment in Mission One as seen in Fig. 9. The horizontal tail area was set at 38% the area of the wing, or 104 ft^2, such that the tail met the static margin constraints outlined in the RFP [1] throughout all subsonic portions of mission one. In addition, stall recovery was checked and added to the scissor diagrams to ensure the tail has enough control authority to prevent stall.

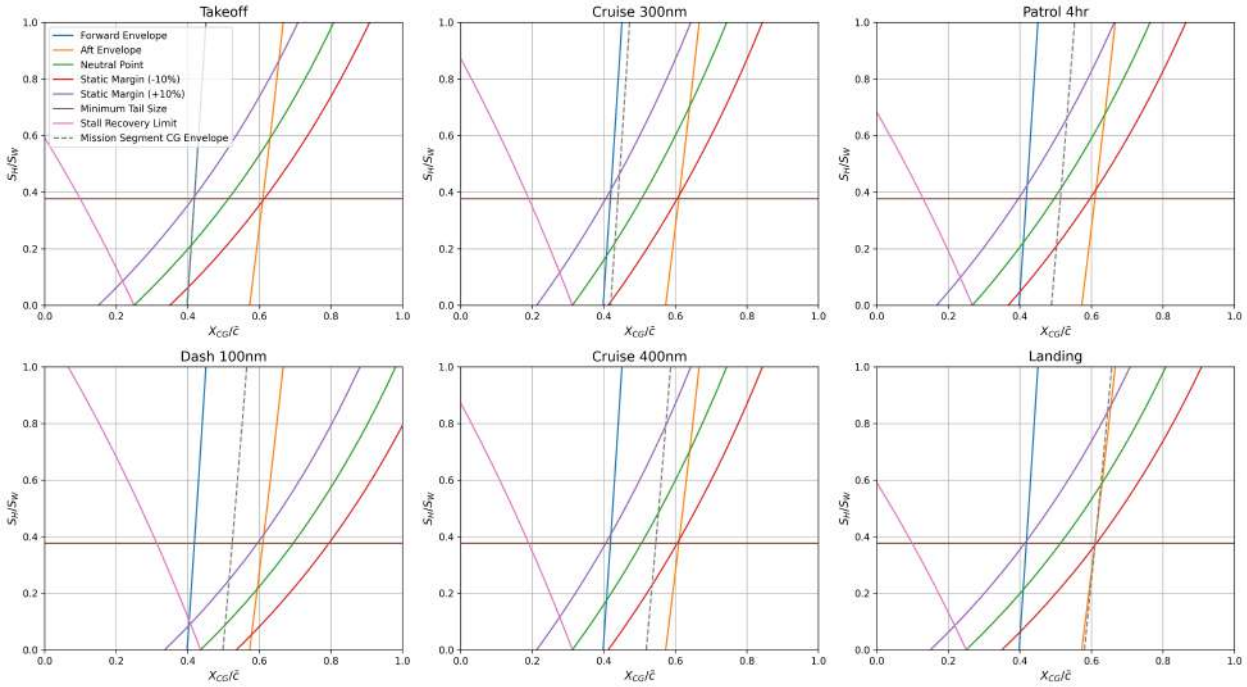

Fig. 9 Scissor plots.

A trade study was conducted on the taper ratio, quarter chord sweep, leading edge location, and aspect ratio of the horizontal stabilizer equations from Roskam Parts Six [7] and Seven [6] in order to determine a viable combination of parameters that yielded the least trim drag during the Patrol phase of mission one, as reducing trim drag primarily in this mission segment would most substantially reduce fuel consumption. The results of this trade study are plotted on contour maps on Fig. 10. Regions where the aircraft does not satisfy the static margin constraints were removed from the contour maps. The selected parameters for the horizontal and vertical stabilizer are found on Table 6.

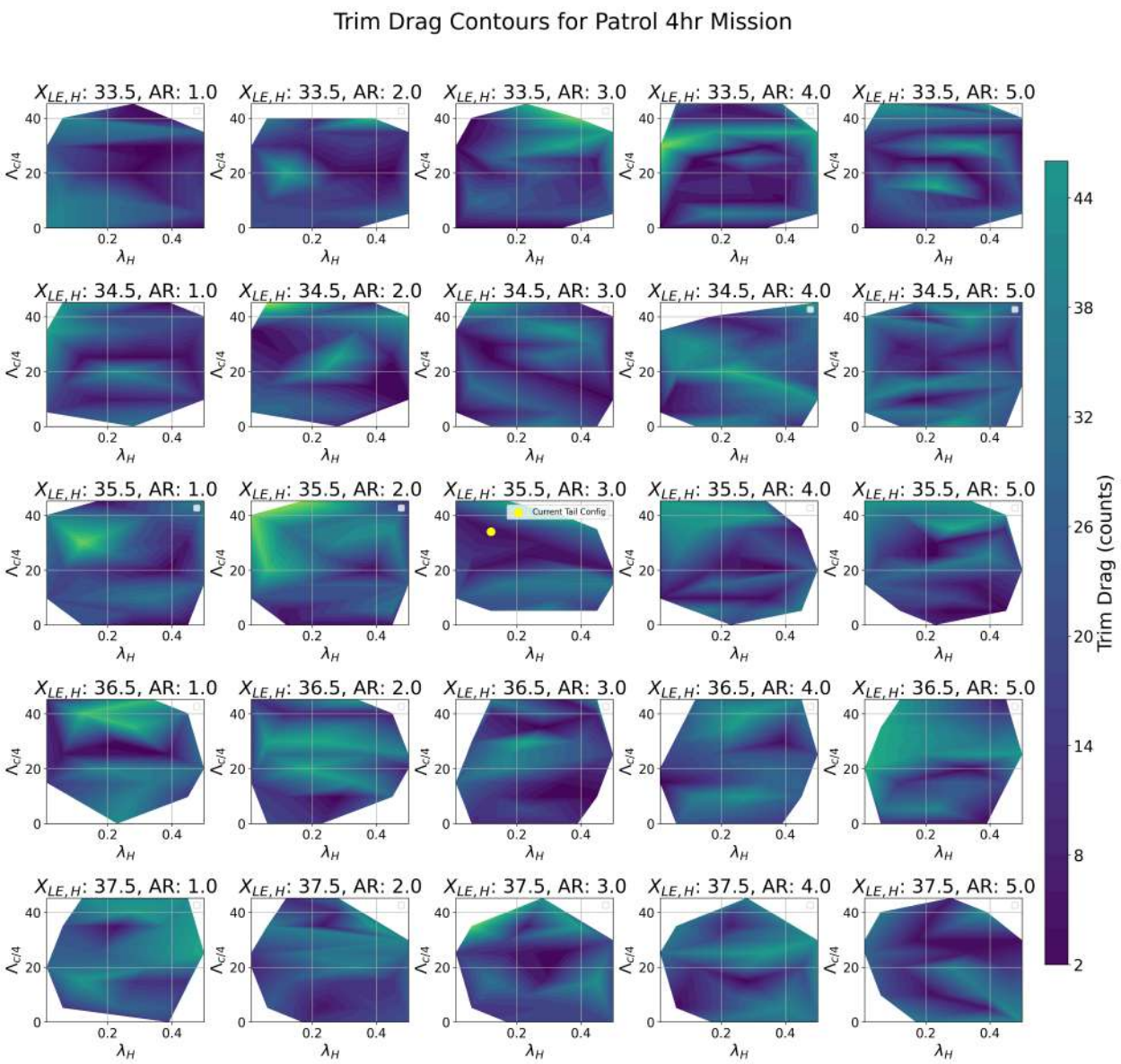

Fig. 10 Trim drag contour plot for mission one patrol segment.

Table 6 Tail Dimensions

	H. Stabilizer	V. Stabilizer	V. Stab. (Sec 1)	V. Stab. (Sec 2)
Span (ft)	18	7.63	1.8	5.83
MAC (ft)	5.92	7.53	-	-
Ref Area (ft^2)	104	108.1	17.75	36.27
AR	3	2.16	-	-
Airfoil	NACA 0008	NACA 0008	-	-
X Location (LE, ft)	35.75	33.36	-	-
Root Chord (ft)	10.42	-	11.5	8
Tip Chord (ft)	1.35	-	8	4.5
Sweep (1/4c, deg)	34	-	60	35
Volume Coeff.	0.47	0.10	-	-

4. Configuration, JW

During the design process, two primary configurations shown in Fig. 11 were considered for the Lobo: a swept-wing design with a horizontal tail and a delta-wing design without a horizontal tail. Both were evaluated based on performance, stability, controllability, and mission requirements.

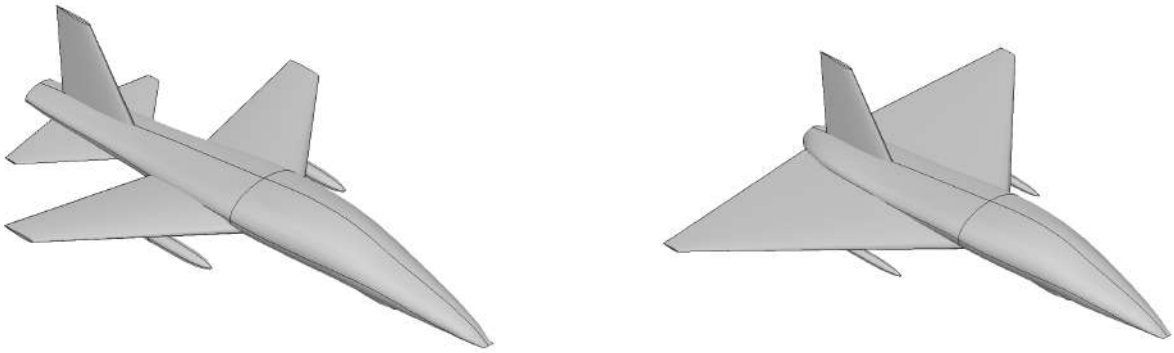

((a)) Option One Configuration **((b)) Option Two Configuration**

Fig. 11 Comparison of configuration options.

Option 1: Swept Wing with Horizontal Stabilizer

- **Wing:** Swept wing with a trailing edge sweep, aspect ratio of 4.0, span of 30 ft, and wing area of 225 ft^2.
- **Fuselage:** 47 ft, providing additional fuel storage and internal volume.
- **Tail:** H-stab configuration for improved stability and control.

Option 2: Delta Wing without Horizontal Stabilizer

- **Wing:** Delta wing with a 350 ft^2 area, aspect ratio of 3.35, and span of 35 ft, improved maneuvering envelope.
- **Fuselage:** 36 ft, reducing drag and weight compared to Option 1.
- **Tail:** V-stab only, eliminating the H-stab to reduce weight and drag.

A. Trades

The swept-wing design with an H-stab offers a higher aspect ratio, improving aerodynamic efficiency and extending range and endurance. However, this comes at the cost of added weight. Its longer 47 ft fuselage increases fuel capacity, enhancing mission duration, but also introduces more drag and structural weight. The inclusion of a horizontal tail provides improved stability and control authority for high-speed maneuvering, though it increases both weight and complexity.

The delta-wing configuration, on the other hand, has a larger wing area, which enhances lift and maneuverability, particularly for takeoff and high turn rate maneuvers. However, this also results in increased drag and decreased

performance in other operating regimes, such as extended cruise or loiter. The absence of an H-stab reduces stability and controllability, necessitating a larger wing and complex control surfaces to compensate. While the shorter 36 ft fuselage reduces weight and drag, it limits fuel storage and overall internal volume which is a major challenge for this design.

B. Selected Configuration

After evaluating these trade-offs, the trapezoidal swept-wing design with a horizontal stabilator was chosen for its balance of performance, stability, and mission flexibility. The higher aspect ratio of 3.79 improves aerodynamic efficiency during cruise and loiter, directly contributing to improved range, endurance, and lower overall weight. The wing, swept at angle of 30 deg about the quarter chord, minimizes drag caused by supersonic flight. The longer 47 ft fuselage allows for greater fuel storage for longer mission durations. The H-stab was retained for its improved stability and control, which are critical for high-performance interception missions. This configuration was ultimately selected due to its predictable stability across a wide range of speeds, reducing the need for complex airfoil design. The landing gear utilizes a tricycle design with one wheel per gear, inspired by the F-5, F-16, and F-18. It will retract into the fuselage with doors, and feature steering on the nose wheel. A CAD model of the Lobo configuration was developed in Siemens NX in order to refine the outer geometry and to perform volume checks and integrate systems. Below, Fig. 12 shows the selected Lobo configuration 3-view with major dimensions of the aircraft and its external components and systems.

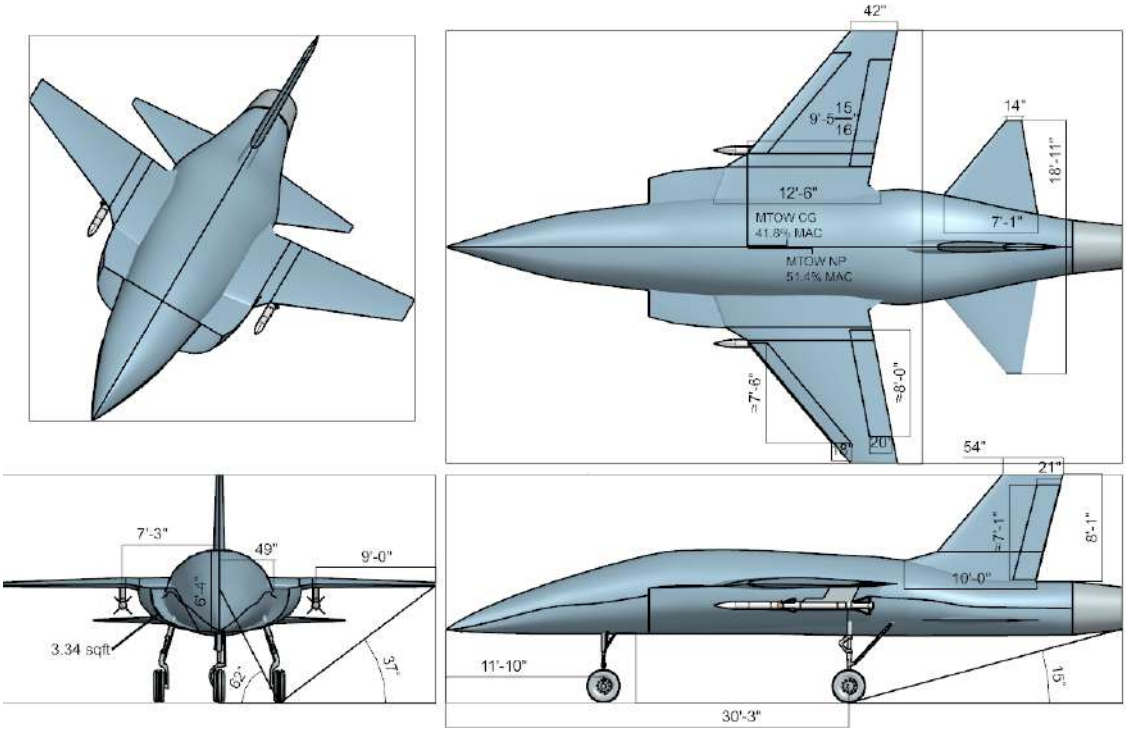

Fig. 12 Lobo configuration 3-view.

C. Internal Layout

The internal layout of the Lobo was designed to minimize space utilization while ensuring proper center of gravity location during all phases of flight. A major design consideration was the placement of the fuel tank, avionics, landing gear, and inlets such a way that the maximum cross sectional area of the fuselage is utilized without compromising structural component volume. The following subsections detail the arrangement of key internal components. A diagram of the internal configuration is provided below in Fig. 13.

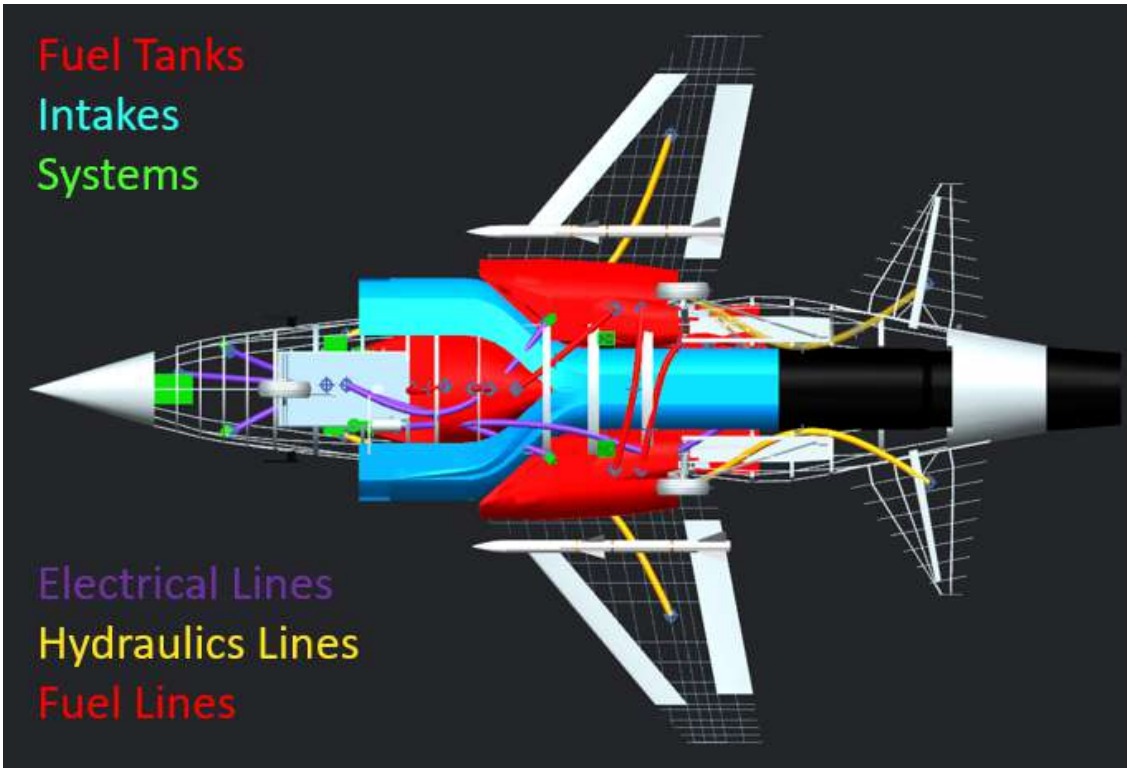

Fig. 13 Internal layout diagram.

1. Fuel System and CG Management

The primary fuel tank is located near the center of the fuselage between the wings which is the best location for weight distribution to maintain stability across different fuel loads. The tank is segmented into eight sections, allowing for active center of gravity management as fuel is consumed. This design is compact and seeks to minimizes shifts in CG location that could otherwise affect stability and control authority.

The fuel tank is also designed to inhabit otherwise difficult to utilize fuselage volume as it fills gaps between the stowed landing gear and intake ducts. This ensures that the available space is used efficiently while keeping one of the aircraft's heaviest components near the aircraft's longitudinal center of mass.

To deliver fuel to the engine, tubing is routed from the front of the fuel tank to the fuel strainer and filter. Drawing

fuel from the front of the tank was done to control mass distribution and stability characteristics during flight. The strainer and filter are positioned just ahead of the engine fan face, before the compressor section. This placement ensures that the fuel system components remain in a region away from high-temperature engine zones.

2. Avionics and Flight Systems

The avionics and flight control systems are housed in the forward fuselage, directly behind the radar dome. This placement provides easy access for maintenance and allows for short, efficient wiring runs between the flight computer, sensors, and communication systems.

The avionics bay is placed in the aft end of the forward fuselage area and tucked underneath part of the primary fuel tank. Three hydraulic reservoirs surround the bay with one placed directly behind the radar dome and the other two fitted between the fuselage and avionics bay sides.

3. Landing Gear Stowage and Retraction Mechanism

For landing gear placement, the forward placement of the nose gear is used to enhance ground handling and overall stability during taxi, takeoff, and landing operations. The main gear is mounted near the aft end of the fuel tanks. This location aligns closely with the wing-fuselage junction, one of the strongest structural regions. The placement ensures the landing gear can withstand the high loads experienced during aircraft operations. Additionally, placement near the aircraft's CG helps support a balanced weight distribution.

The Lobo features a tricycle landing gear configuration, designed to retract into the fuselage while minimizing impact on internal volume. The retraction mechanism proceeds as follows:

- **Nose Gear:** Rotates up and aft into a compartment beneath the fuel tank.
- **Main Gear:** Rotates inward at a 25 deg angle while moving aft to stow inside the fuselage and beneath the fuel tank.

This design allows for a landing gear of length capable of providing at least 15 deg of nose-up rotation during takeoff with a safety margin, and allows for the future implementation of a stronger and structurally larger landing gear required for carrier-based operations.

4. Inlets and Engine

Lateral inlets extend from beneath the wings along the sides of the fuselage. The exposed upper surface of the inlet is blended into the wing, creating a leading edge root extension. An S-duct configuration is used to guide airflow inward, allowing the ducts to be blended into the fuselage and merge near the center of gravity. A straight duct continues to the engine which is mounted toward the rear of the aircraft.

5. Propulsion, PS

A. Engine Selection

Based on RFP [1] requirements, engines capable of efficient transonic and supersonic performance were required. From this analysis, turbojets and turbofans were deemed the most appropriate to consider for the design process. While turbojets offer higher performance at supersonic speeds, the design missions specified in the RFP [1] favor the transonic regime where turbofan engines demonstrate superior efficiency. By selecting low-bypass turbofan engines, a balanced tradeoff between the high-speed performance required for supersonic maneuvers and fuel efficiency during transonic flight segments can be found.

Single-engine and twin-engine configurations were considered during the design process. Although the twin-engine configuration offers redundancy in the case of damage, failure, or malfunction of an engine, the RFP [1] requirement for a fully autonomous vehicle reduces the criticality of this advantage. While survivability remains a design consideration, the absence of a human pilot lessens the necessary redundancy typically prioritized. Given this, the team determined that the justification for a twin-engine configuration is less compelling, and instead targeted the advantages of a single-engine approach in terms of a maintenance simplicity and overall cost savings. This latter point being a key factor in meeting the strict budget requirement outlined in the RFP [1].

An engine trade study was conducted to evaluate different engine candidates. The following four engines were considered for the design: the F118-GE-100, the F110-GE-129, the F110-GE-132, and the F100-PW-229. Engine data can be found in Table 7. In accordance with RFP [1] requirements, only engines that could be purchased off-the-shelf were examined which helped eliminated any large development costs and further reduced maintenance and support costs.

Table 7 Comparison of Turbofan Engines for Sea Level Conditions

Engine	Takeoff Thrust Dry (lb)	Takeoff Thrust Wet (lb)	Weight Dry (lb)	SFC Dry (lb/lb-hr)	SFC Wet (lb/lb-hr)	Bypass Ratio	Fan Diameter (in)
F118-GE-100 [8]	20,187	-	3,163	0.66	-	0.76	36.1
F110-GE-129 [8]	17,595	29,474	3,940	0.67	1.85	0.74	36.1
F110-GE-132 [9][10][11]	17,000	32,000	4,050	0.75	2.09	0.68	36.1
F100-PW-229 [8]	17,800	29,100	3,830	0.74	2.05	0.39	34.8

After sizing, a dry thrust requirement of at least 17,000 lb was determined. All of the candidate engines met this requirement. Additionally, the team determined that selecting an engine with installed afterburners would provide significant performance benefits particularly during supersonic flight and high-thrust combat scenarios. As a result, the F118-GE-100 was eliminated as an option due to the lack of an afterburner. The remaining engines demonstrated sufficient wet thrust capability.

A key consideration for the team during the engine selection process was reducing the overall weight of the aircraft. While selecting a lighter engine contributed to this goal, a greater impact could be made by reducing the amount of fuel required. This became increasingly important once the team evaluated the amount of fuel burn occurring during the

aircraft's loiter phase of the defensive counter-air patrol mission. To address this, engines with lower fuel consumption were prioritized to help minimize fuel weight. Among the remaining engines, the F110-GE-132 exhibited the highest dry and wet SFC while the F100-PW-229 closely followed. In contrast, the F110-GE-129 had the lowest SFC values in both categories. As a result, the F110-GE-132 and F100-PW-229 were both eliminated due to unfavorable SFC values.

Therefore, the F110-GE-129 was selected based on the trade study results as it met the key criterion of a low specific fuel consumption while also offering afterburning capability and sufficient thrust output.

B. Engine Specifications and Performance

The F110-GE-129 engine, shown in Fig. 14, is an afterburning, low-bypass turbofan engine produced by General Electric Aviation used primarily for fighter aircraft. Compared to its predecessor, the F110-GE-100, the F110-GE-129 offers an improved thrust-to-weight ratio along with a 30% increase to thrust in low-altitude combat regions [12]. Table 8 contains the specifications for the engine [8].

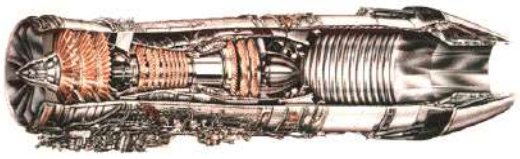

Fig. 14 F110-GE-129 engine cutaway.

Table 8 F110-GE-129 Specifications

Engine Design	
Length (in)	187.6
Fan Diameter (in)	36.1
Max Diameter (in)	46.5
Weight (lb)	3,940
Static Airflow (lbm/s)	270
Pressure Ratio	31.2
Bypass Ratio	0.74
Burner Temperature (K)	2,944
Number of Spools	2
Engine Performance at Sea Level Conditions	
Dry Thrust (lbf)	17,595
Wet Thrust (lbf)	29,474
Dry SFC (lb/lb-hr)	0.67
Wet SFC (lb/lb-hr)	1.85
T/W	4.47

Based on these engine specifications, the team conducted simulations in GasTurb to generate performance data across a range of relevant flight conditions. Simulations were run for Mach numbers from 0 to 1.6 and for altitudes ranging from sea level up to 50,000 ft.

To align with RFP [1] requirements specific off-take loads and bleed conditions were incorporated into the GasTurb simulation. This included a 75 kW power extraction to support electrical and hydraulic systems and a 2% engine mass flow bleed for the avionics liquid cooling system and environmental control systems. Furthermore, an additional 0.5%

bleed was utilized for internal inlet boundary layer removal.

The GasTurb simulations were run based on a military specification pressure recovery schedule. To better represent the characteristics of the team's specific inlet design (a detailed description of which is provided in a later section), a pressure recovery schedule for the inlet was refined using a methodology from Nicolai. First, a diffuser loss coefficient of 0.096 was selected from Nicolai's Fig. 15.4 based on the inlet's length-to-height ratio of 6.32. With this value, the pressure recovery schedule was determined from Nicolai's Fig. 15.5. Finally, Equation 16.1 from Nicolai was applied to adjust the GasTurb output to reflect the updated pressure recovery [8]. Figure 15 illustrates the change in pressure recovery schedule for the adjusted data.

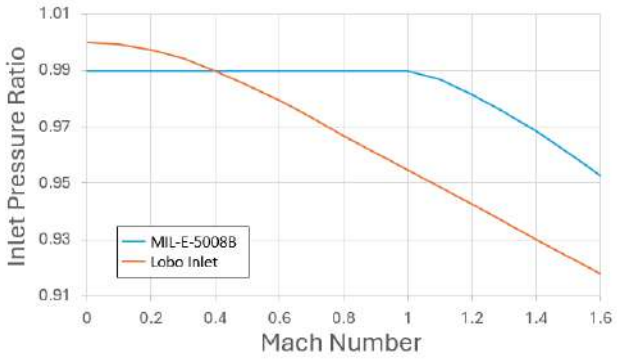

Fig. 15 Comparison of pressure recovery schedules.

Net thrust versus specific fuel consumption was plotted at an altitude of 35,000 ft across a range of Mach numbers (see Figs. 16 and 17). The plots illustrate engine performance for both afterburner off and afterburner on settings. Each design point is colored to correspond with its respective flight condition curve.

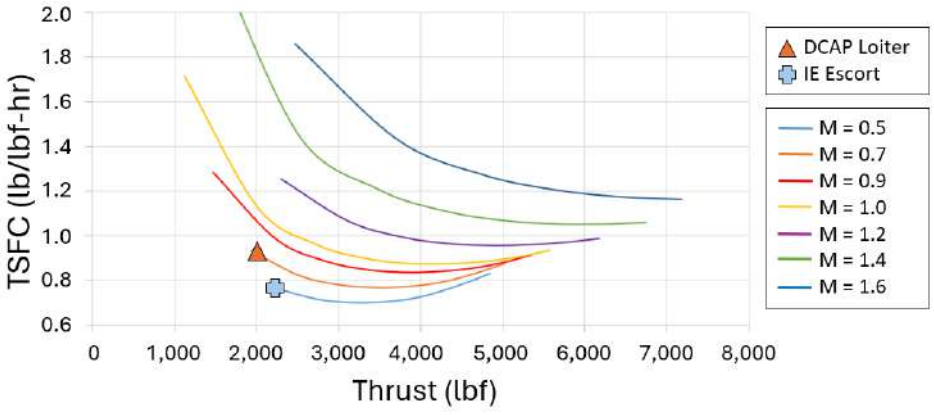

Fig. 16 Net thrust versus specific fuel consumption at 35,000 ft with afterburner off.

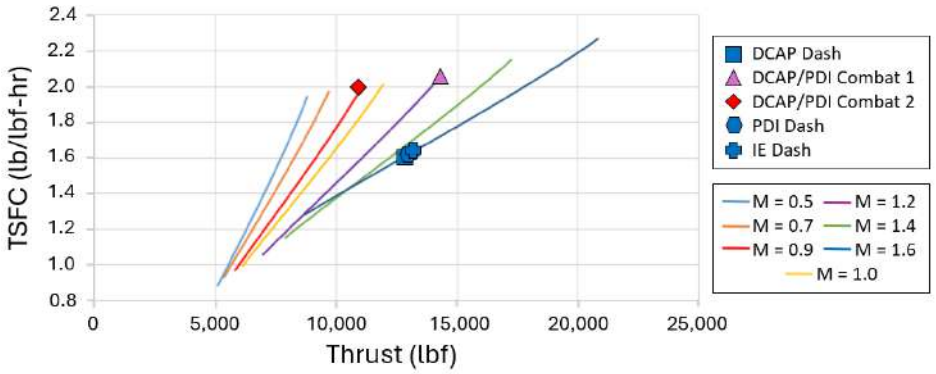

Fig. 17 Net thrust versus specific fuel consumption at 35,000 ft with afterburner on.

Additionally, thrust performance at maximum dry and maximum wet power settings was plotted as a function of Mach number for a range of altitudes (See Figs. 18 and 19). The plots illustrate engine behavior and performance across the flight envelope, making it easier to identify trends that are critical for mission planning and design optimization. Certain design points required only a fraction of the available thrust at both maximum dry and wet power settings, demonstrating that the engine maintains excess power throughout the flight envelope.

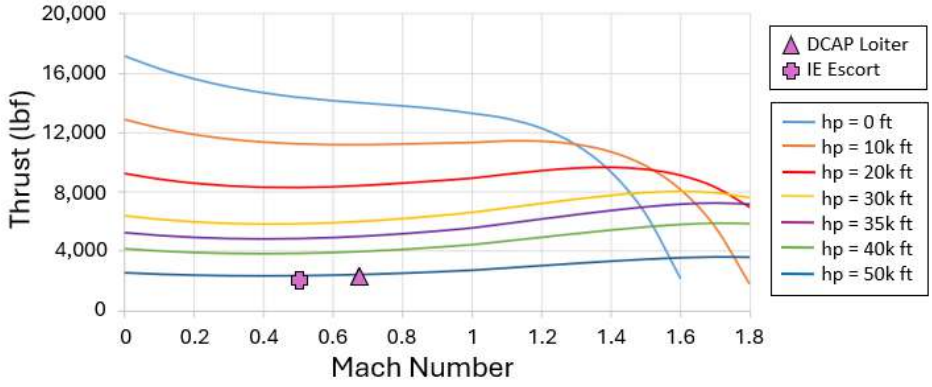

Fig. 18 Mach number versus net thrust at power condition 50.

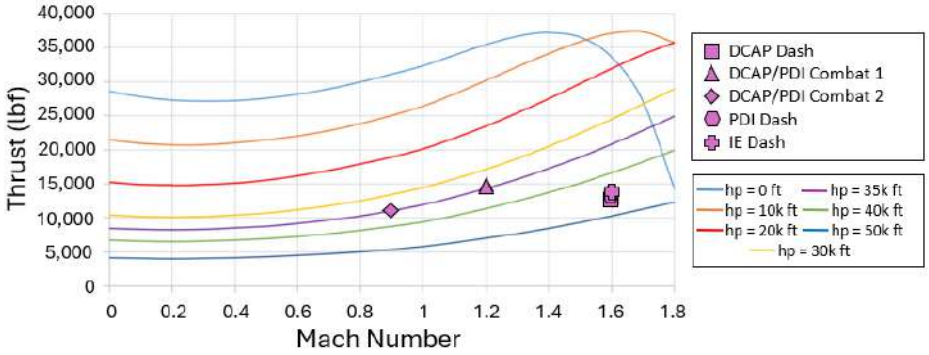

Fig. 19 Mach number versus net thrust at power condition 100.

Figure 20 depicts net thrust versus specific fuel consumption at Mach numbers of 0.5, 0.7, 0.9, and 1.2 providing insight into engine behavior across key segments of the flight envelope. These plots highlight how thrust and fuel efficiency vary with throttle setting at each Mach number. This information was used to identify optimal operating points during mission segments such as loiter and escort.

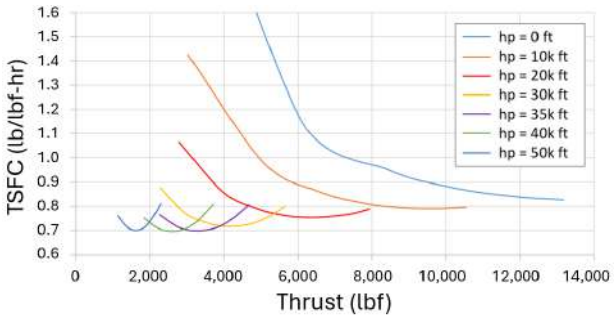

((a)) Mach Number 0.5

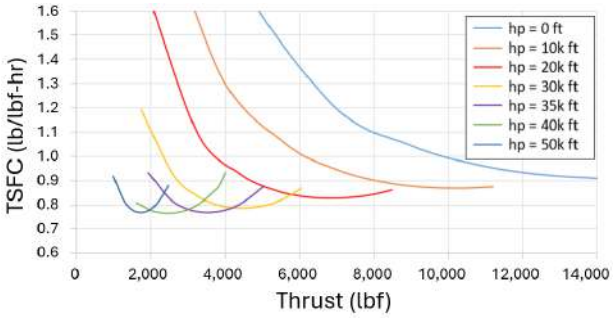

((b)) Mach Number 0.7

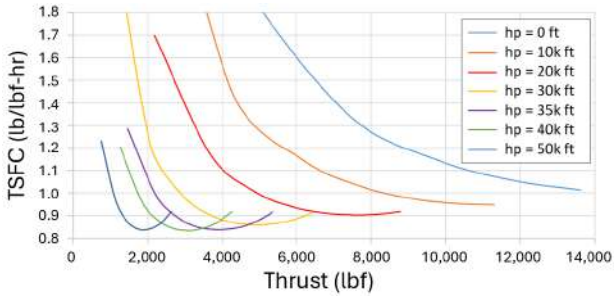

((c)) Mach Number 0.9

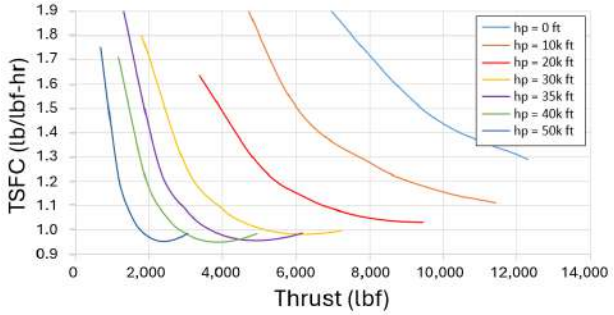

((d)) Mach Number 1.2

Fig. 20 Net thrust versus specific fuel consumption at constant Mach number for varying altitudes.

It is worth noting that the GasTurb simulations tended to be less reliable at low throttle settings, particularly when engine burner temperatures fell below certain thresholds. To address this limitation, sea-level flight test data from the F-16 operating at around Mach 0.3 was used to guide performance trends in the low power regime [13]. Although the dataset corresponds to the F100-PW-229 engine, the characteristics of the engine were deemed sufficiently representative of the F110-GE-129 engine.

Using the dataset, the relationship between thrust and fuel flow was extrapolated to approximate the expected engine performance of the F110-GE-129 at low throttle settings. This pattern was then generalized for other Mach numbers and altitudes. While this method does introduce some degree of approximation, it yields more realistic fuel flow estimates at low power conditions than GasTurb simulations alone. In future design iterations, the accuracy of this method could be improved upon with access to performance data for the F110-GE-129 engine. Figure 21 provides an example of the extrapolation process using the F-16 dataset for Mach 0.3 at sea-level.

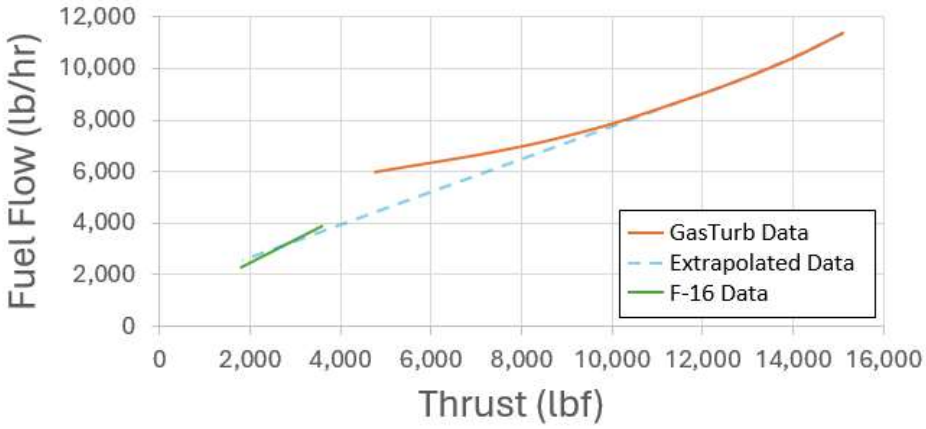

Fig. 21 Data extrapolation for Mach 0.3 at sea-level.

C. Inlet Design

To ensure reliable engine performance across a wide range of mission conditions, careful attention was given to the inlet configuration, sizing, and integration. Achieving consistent, distortion-free airflow was essential for maintaining thrust performance and sustaining engine efficiency.

1. Inlet Trade Study

Two inlet configurations were evaluated during the design process: a chin-mounted inlet and lateral-mounted inlets. The chin inlet offers more simplified ducting helping create a more symmetric airflow into the engine. The configuration is however susceptible to flow separation at high angles of attack as well as debris flying into the intake during takeoff. Lateral inlets, by contrast, provide superior performance at high angles of attack. This is an important consideration for combat-oriented aircraft where maneuverability is key. The primary drawbacks of the lateral inlets revolve around the aerodynamic complexity they create. This includes the risk of uneven airflow forming during certain flight maneuvers, and a greater need to manage fuselage-inlet interactions such as boundary layer effects.

Considering aircraft design goals and objectives, the team determined lateral inlets were the most appropriate configuration. Prioritizing aircraft combat ability, the improved high-angle-of-attack capability and overall agility of the lateral inlets outweighed the additional integration and airflow management concerns.

In addition to selecting inlet configuration, the team explored multiple inlet types to pair with the lateral inlets. Three candidates were evaluated: the pitot inlet, cone inlet, and 2D variable geometry inlet. The pitot inlet is simple and performs well in the subsonic and transonic regimes. Alternatively, the cone inlet offers improved supersonic performance, but it adds additional weight, complexity, and poor performance away from design conditions. The 2D variable geometry inlet offers excellent performance across a large range of Mach numbers through adjustable internal ramps. Similarly to the cone inlet, it does, however, add additional weight and complexity.

To support a final decision, a trade study was conducted using GasTurb's intake mapping tools. Thrust data was

collected across a range of Mach numbers at 35,000 ft altitude representing the aircraft's operational envelope. Each inlet configuration was compared against a standardized military specification baseline to assess performance. A comparison was conducted between lateral- and chin-mounted configurations using a pitot inlet, while additional evaluations were performed for cone and 2D variable geometry inlet types within a lateral inlet configuration. The results can be found in Table 9.

Table 9 Percent Change in Thrust Relative to Military Specification Baseline Across Inlet Configurations

Flight Regime (Mach Range)	Pitot Inlet Lateral Configuration	Pitot Inlet Chin Configuration	Cone Inlet Lateral Configuration	2D Variable Inlet Lateral Configuration
Subsonic (0.0 – 0.8 M)	-5.71%	-5.95%	-18.80%	-7.67%
Transonic (0.8 – 1.2 M)	-2.73%	-2.49%	-13.72%	-3.57%
Low Supersonic (1.2 – 1.6 M)	-5.71%	-7.28%	-8.36%	-2.53%

The results of the study reinforced the selection of a lateral inlet configuration as performance differences between lateral- and chin-mounted designs were minimal in the subsonic and transonic regimes. Notably, the lateral configuration showed a slight advantage in the low supersonic regime. When combined with the maneuverability benefits necessary for combat, the lateral inlets were confirmed as the preferred configuration. Regarding inlet type, the cone inlet was ruled out due to its poor performance in the lower Mach regimes which make up a significant portion of the aircraft's mission profile. Although the cone inlet would perform better at higher speeds, the aircraft is not expected to fly at speeds necessary to leverage this advantage. The 2D variable geometry inlet showcased strong performance across all Mach regimes with particularly notable results in the low supersonic regime. With that said, the added mechanical complexity conflicted with the RFP's directive to prioritize simplicity where possible. Ultimately, the team selected the pitot inlet as it balanced performance and structural simplicity while also aligning well with the aircraft's expected operational envelope. It was however acknowledged that if the aircraft design prioritized low supersonic operation to a higher priority, and if the budget and integration complexity constraints were more relaxed, the 2D variable inlet would have been the leading candidate.

2. Inlet Geometry

To define the inlet geometry, the team began by calculating the required inlet capture area necessary to deliver sufficient airflow into the engine. Proper sizing is essential as an incorrect design can cause the engine to either suck or spill air in or out of the inlet. In both cases, engine performance will drop due to increased aerodynamic drag and a significant reduction in available thrust. Additionally, the inlet capture area must account for secondary air requirements such as for cooling or bleed. The inlet was optimized for the aircraft's loiter design point of Mach 0.65 at 35,000 ft. This phase of the mission has the highest fuel consumption and places the greatest demand on engine airflow. To determine the necessary capture area, the team applied two methods. The first, based on Nicolai's Equation 15.2, used a mass

flow approach [8]. With collected engine GasTurb data, a capture area of 5.78 ft^2 was calculated. The second method, using Nicolai's Equation 15.3, applied compressible flow relations and produced a slightly larger capture area value of 6.68 ft^2 for an engine fan face Mach number of 0.6 [8]. To maintain sufficient airflow under all conditions, the team conservatively selected the larger capture area value. Since the design incorporates two lateral inlets, this total capture area value was evenly divided resulting in an area of 3.34 ft^2 per inlet.

To determine the inlet length, the team referenced Fig. 15.4 from Nicolai [8]. Based on the loiter design point of Mach 0.65, a diffuser length-to-height ratio of 6.32 was identified corresponding to a diffuser loss coefficient of 0.096. Using the calculated capture area, this resulted in an inlet length of 18.45 ft.

3. Inlet Integration and Flow Management Features

Due to space constraints within the fuselage, the design required a relatively sharply curved S-duct geometry. The configuration is depicted in Fig. 13. The design introduced concerns regarding potential flow distortion and uneven airflow into the engine. To assess its feasibility, the team examined the F-35's aggressive lateral inlet S-duct as a reference [14]. It was observed that the ratio between the vertical and horizontal duct curvature was similar to that of the current design. This similarity helped validate that the geometry of the proposed duct layout falls within the range of operational implementations.

To mitigate distortion effects, several design strategies were implemented. Quarter-circle duct segments were used for inlet entrances to help maintain a more uniform airflow that enters the system. Additionally, the inlets were aligned nearly level with the engine in the vertical plane which limited distortion potential to the horizontal plane. Following the convergence of the two lateral inlet ducts, a long straight section of duct was introduced to promote flow realignment and improve uniformity at the fan face. Recognizing that this extended duct section would contribute to increased boundary layer buildup, the team, as previously mentioned, introduced an additional 0.5% bleed for internal inlet boundary layer removal.

A challenge associated with lateral inlet configurations is their tendency to ingest low-energy boundary layer air from the fuselage surface. This reduces the total pressure recovery and introduces additional flow distortion. To mitigate these effects, the team incorporated a boundary layer diverter into the inlet design. The diverter functions by separating the slower-moving boundary layer flow from the freestream air thus improving airflow uniformity and enhancing overall inlet efficiency. This feature is particularly important during subsonic cruise and high angle of attack conditions. To size the diverter, the team applied Nicolai's Equations 16.19 and 16.20 to estimate boundary layer thickness [8]. Designing for the most demanding condition, the Mach 0.5 escort design point at 35,000 ft resulted in a required diverter height of 4.82 in.

Given that the calculated inlet capture area of 6.68 ft^2 is reasonably close to the F-16's inlet capture area of appropriately 5.15 ft^2, elements of the F-16 inlet system were examined to inform the design process. A particularly

relevant feature was the F-16's auxiliary inlet doors which open during low-speed, high-power conditions such as takeoff [15]. This system ensures that the engine receives adequate mass flow during phases of flight where demand is elevated. Drawing from this precedent, the team implemented a similar auxiliary airflow mechanism to support engine requirements during takeoff. This solution improves inlet performance and preserves aerodynamic efficiency, removing the need to oversize the inlet during off-design conditions.

For the exhaust design, the team selected a variable area nozzle. By either expanding or contracting the exit area, the nozzle area will change to better optimize for thrust at different speeds further improving engine performance. Additionally, due to the usage of an afterburner engine, an exhaust nozzle that has a variable shape and area is necessary to handle the excess thrust.

6. Aerodynamics, CG

A. Methodology

In the design of a supersonic fighter aircraft, the wing and aerodynamic design are critical in ensuring the aircraft can meet the requirements outlined in the RFP [1]. The design of the wing was driven by the transonic loiter segment and the supersonic dash in the Defensive Counter-Air Patrol Mission discussed in Section 2. Each design decision made in the design of the wing was selected with a trade between aircraft performance and cost.

B. Airfoil Selection

To begin the design of the wing for the Lobo, it was necessary to first select an airfoil that could provide the necessary performance in both the subsonic and supersonic regimes. It was determined in the initial design stage that the selected airfoil should be thin to minimize wave drag for the transonic and supersonic flight regimes the Lobo will operate in, as wave drag on the airfoil increases with square of the t/c [8]. Therefore, it was determined that the maximum t/c of the airfoil should not exceed that of the airfoils used in the application of other supersonic fighter aircraft. To determine the range of tested t/c values for the candidate airfoils, similarity analysis was used. Table 10 below shows the airfoils used on several current and historical supersonic fighters [16]. It was determined that the selected airfoil should belong to the laminar family of NACA 64- or 65- series airfoils, as minimizing skin friction drag is paramount in a high-speed aircraft. Further, these airfoils have been previously mass-produced for supersonic fighters, enabling a more streamlined manufacturing process in fulfilling the order of 1000 aircraft.

Table 10 Airfoils used by Current and Historic United States Supersonic Fighters

Aircraft	**Airfoil**	**Thickness** (t/c)
F-16C	NACA 64A204	4%
F-5E	NACA 65A004	4%
F-14A	NACA 64A209	9%
F-15C	NACA 64A006	6%
F/A-18 E/F	NACA 65A005	5%

To determine the minimum t/c of the candidate airfoils, the increased wing weight and cost that would arise from a thin airfoil was considered, giving a minimum t/c of 6%. Through this similarity analysis, it was also determined that the airfoil selected should be aft-loaded, with a maximum thickness location of 40-50% of the chord. The camber of the selected airfoil should also be kept low, as camber increases wave drag. At maximum, supersonic fighters use an airfoil with a maximum camber of 1.1%, which was used as the maximum camber for a candidate airfoil. The selected candidate airfoils and their geometry selected for the trade study are shown below in Table 10, with values obtained from the UIUC Airfoil Database [16].

Table 11 Candidate Airfoils for Trade Study

Airfoil	Maximum Camber	Maximum Camber Location (% Chord)	Thickness (t/c)	Maximum Thickness Location (% Chord)
NACA 64-208	1.1%	50%	8%	40%
NACA 64-008A	0%	-	8%	40%
NACA 65-206	1.1%	50%	6%	50%
NACA 64-206	1.1%	50%	6%	40%
NACA 65-209	1.1%	50%	9%	50%

SU2's 2-D RANS (Reynolds Averaging Navier-Stokes) solver was used to perform an analysis of the selected airfoils. This solver is a useful tool that provides quick calculations of the C_l and C_d values of the airfoils while considering both inviscid and viscous effects on the airfoil, allowing accurate modeling of subsonic and supersonic conditions. To accurately analyze the airfoil's performance in both the subsonic and supersonic regime, each airfoil was tested at a nominal subsonic case of Mach 0.3 at sea level and a Reynolds number of 17.0×10^6, as well as at the maximum aircraft speed of Mach 1.6 at FL350 and a Reynolds number of 30.5×10^6. The C_l and C_d values of the airfoil in both regimes is shown below in Figs. 22 and 23.

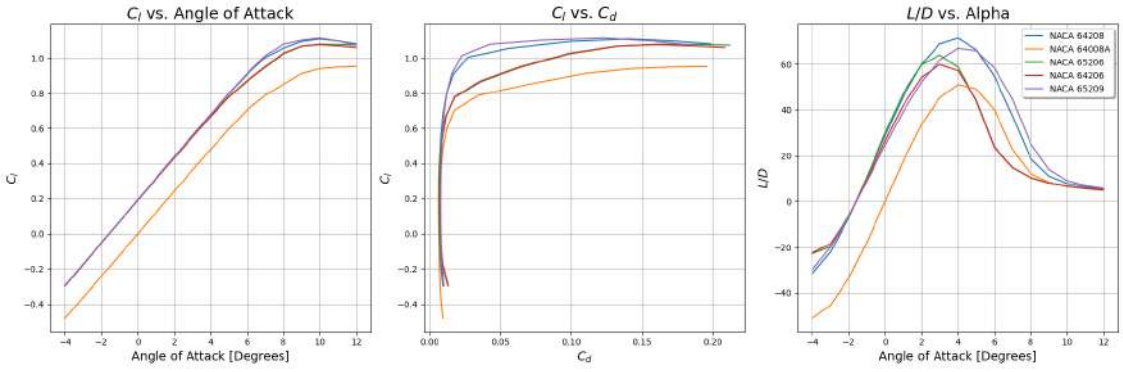

Fig. 22 Candidate airfoils subsonic SU2 data [Re = 17.0×10^6**].**

As can be seen by the above plots, at subsonic speeds, cambered airfoils offer a higher C_l than symmetric airfoils, something desired for the Lobo's design to loiter for long periods of time. It is also seen that in the subsonic regime, thicker airfoils such as the NACA 64-208 and NACA 65-209 provide more lift for the same amount of drag, again

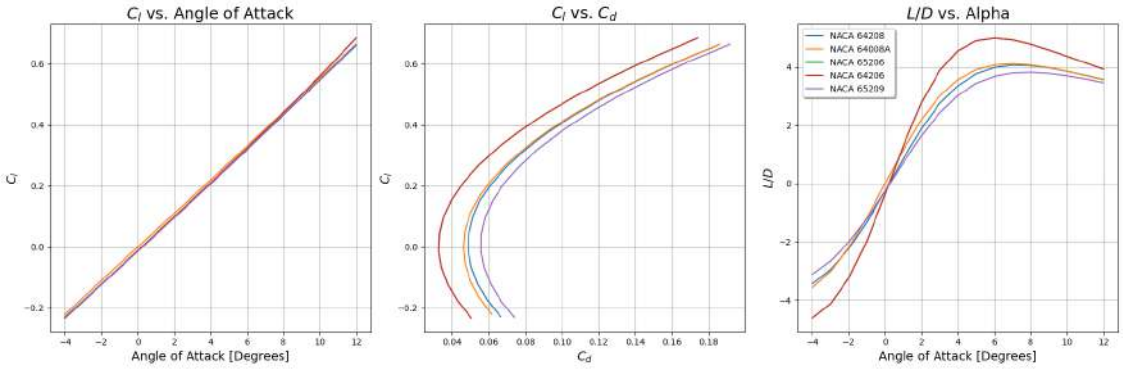

Fig. 23 Candidate airfoils supersonic SU2 data [Re = 30.5×10^6**].**

advantageous for sustained periods of subsonic loitering. When considering the subsonic flight regime, through the trade study it was determined that a thicker cambered airfoil is beneficial for the Lobo.

In the supersonic regime, it is found that all candidate airfoils, regardless of camber or t/c, generate the same amount of lift for a given angle of attack. However, supersonic drag is minimized for thin airfoils with a smaller t/c. Additionally, symmetric airfoils provide less drag at supersonic speed than a cambered airfoil of the same t/c.

To select an airfoil, subsonic loiter, the larger segment of the Lobo's flight was used to justify selecting a thicker airfoil, which would allow for increased performance in this flight regime. The NACA 64-208 was selected over the NACA 65-209 due to a reduction in supersonic drag. Although wave drag is an important consideration for a fighter with supersonic capabilities, it was determined that increased wave drag is something that could be traded for increased subsonic performance, as the Lobo will only need to reach speeds of Mach 1.6 for brief portions of the mission. A trade study determined that increased supersonic drag will increase fuel burn less than the increased subsonic drag. Because the loiter portion of the Lobo's mission is the largest driver of fuel weight, increasing aerodynamic efficiency in this flight regime was of highest importance. A cross-section of the selected NACA64-208 is shown below in Fig. 27.

C. Wing Design

Because the Lobo is designed to be a small, high-performance, low-cost homeland defense interceptor, it was necessary to size the wing to provide adequate performance without increasing cost. In initial design, it was noted that, as Raymer explains, the wing and wing structure are notable drives of aircraft weight [5]. Therefore, wing size should be minimized without compromising aircraft performance. This would reduce the Lobo's weight, requiring less fuel and therefore reducing the aircraft's flyaway and operational costs.

To determine the wing planform design for the Lobo, a combination of similarity analysis and initial sizing iterations were used. To determine the final wing area, an iterative process was used in the preliminary design of the wing. To guide this process, similarity analysis was used to determine the tested bounds of each iterative design, with the F-16C wing area of 300 ft^2 used as the maximum wing area to minimize cost [2].

The wing sweep and taper ratio initial sizing trade study discussed in Section 3 was used to guide the variation of these parameters. 32.5 ft was set as the maximum wingspan, which would allow the Lobo to fit in an aircraft carrier elevator without folding its wings, allowing for carrier-based operations in future variants. This wingspan was determined by the F/A-18 E/F's folded wingspan [2].

The main tool used in this iterative process was Computational Fluid Dynamics (CFD). In this process, each wing iteration was tested in SU2 using an Euler solver, which was selected over Vortex Lattice Methods for this iteration due to the need to approximate the lift for the transonic cruise mission segment. From initial performance evaluations, it was determined that the largest fuel burn came from the Lobo's patrol segment. For this reason, each iterative wing would be evaluated in this flight regime. In this regime, the required angle of attack and resultant L/D was found to determine the most efficient wing for patrol that could meet the outlined constraints in Section 2. Other considerations including the feasibility of structural design also were a driving factor in the final wing design, as a highly tapered wing would require increased structure at the wing tip, increasing wing weight. Through this iterative process, several key wing parameters were determined including reference area, wingspan, taper ratio, aspect ratio, and wing sweep. A tip incidence of -2 deg was added to create washout, which prevents tip stall and keeps the control surfaces usable at high angles of attack. The Lobo's wing geometry is shown in Table 12 and Fig. 24 below.

Table 12 Lobo Wing Geometry

S_{ref} **[ft^2]**	276
AR	3.79
Wingspan [ft]	32.5
Taper Ratio (λ)	0.29
Root Chord (C_{root}) **[ft]**	12
Tip Chord (C_{tip}) **[ft]**	3.5
$c/4$ **Sweep [deg]**	30
MAC [ft]	9.455
Tip Incidence [deg]	-2

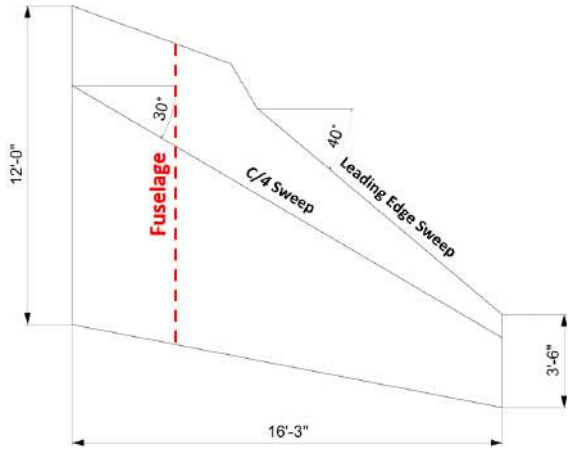

Fig. 24 Lobo Wing Dimensions

D. Leading-Edge Root Extension

A desire for decreased aircraft weight drove the design of a small, high-aspect ratio wing with reduced drag that allows for a high L/D for cruise to reduce fuel consumption. However, when considering the use of the Lobo as an interceptor aircraft, this high aspect ratio is not ideal for maneuvering and climbing at high angles of attack.

To alleviate this issue and allow the Lobo to operate at high angles of attack, it was determined that some measure must be taken to prevent abrupt stall of the aircraft. For this reason, leading edge root extensions (LEX) were added to

the Lobo's wing. The LEX creates a larger inboard section of the wing that preserves the outboard high aspect ratio properties ideal for cruise and patrol. By including a larger inboard section near the wing root, vortices are generated near the fuselage, which keep the flow attached at high angles of attack [5]. Additionally, due to the wing placement on top of the inlet, the upper surface of the inlet body can be used to assist in this vortex generation. To determine the extension length of the root chord, a trade study was performed to evaluate the additional fuel burn associated with increased parasite drag from the wing. It was also determined that minimal extension would not increase the fuel burn substantially. Therefore, by minimally extending the wing root and blending the wing into the upper surface of the inlet, a low wing weight with reduced drag is possible while allowing the Lobo to still operate at high angles of attack.

E. High-Lift Devices

After sizing the wing, it was found through a CFD analysis in SU2 that the clean wing could only produce a clean $C_{L_{Max}}$ of 1.03 at an angle of attack of 14 deg before reaching the tip back angle of 15 deg. To ensure the aircraft would not stall before this point, the pressure gradient was visualized to determine that the flow was still attached and there was no low pressure on the lower surface of the wing.

Because the required C_L for takeoff was 1.1, high-lift devices were necessary. To determine the type of devices used, a similarity analysis was conducted. The type of devices used on several supersonic fighter aircraft was provided by Nicolai [8]. From a similarity analysis, it was determined that single-slotted flaps are common on fighter aircraft and were selected for the Lobo. Because it was known that a high $C_{L_{Max}}$ was needed to meet the instantaneous turn rate of 18 deg/s, it was determined that as much of the wing should be flapped as possible. For this reason, flaperons were also implemented, using all possible area to generate more lift. Additionally, leading edge flaps were implemented to further assist in increasing $C_{L_{Max}}$. These flaps extend across the entire span of the wing's outermost section. The characteristics of the high-lift devices is shown below in 13. The high lift device configuration on the wing planform is shown below in Fig. 25. Fig. 27 shows the high lift devices on the wing airfoil.

Table 13 Lobo High-Lift Device Sizing

Device	**Flapped %**	c_f/c	$\Delta C_{L_{max}}$
Single-Slotted Flap	26.8%	0.190	0.307
Flaperon	18.5%	0.262	0.147
Plain Leading Edge Flap	43.3%	0.214	0.116

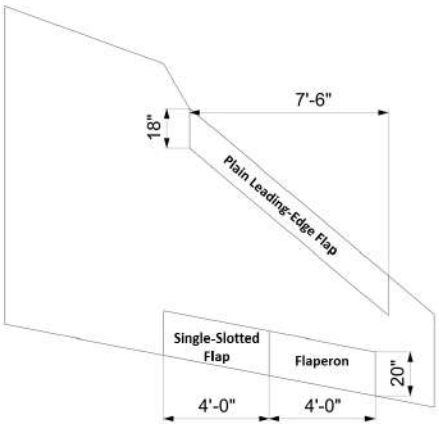

Fig. 25 High-lift device configuration.

To determine the necessary flap deflection at takeoff, Equation 9.3 in Nicolai was used [8]. It was found that for a flap deflection of 20 deg, the Δ_{0L} is -8.6 deg, which allows for the Lobo to achieve a C_L of 1.1 at an angle of attack of seven degrees, considerably lower than the tip back angle, which ensures the Lobo is able to takeoff within the required distance. At sea level with high lift devices, the Lobo achieves a $C_{L_{max}}$ of 1.62. The lift curve of the Lobo with and without high lift devices at takeoff is shown below in Fig. 26.

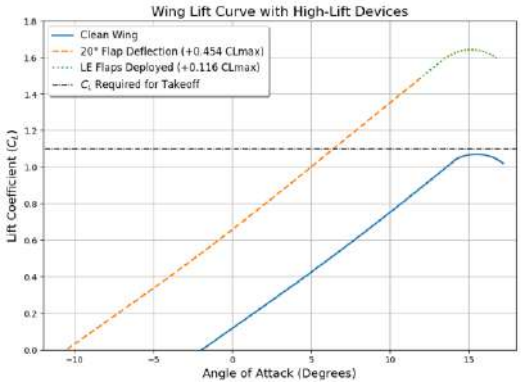

Fig. 26 Takeoff Lift Curve.

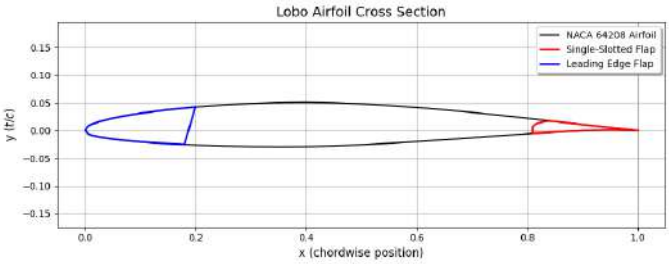

Fig. 27 Lobo Airfoil and High-Lift Devices.

F. Supersonic Considerations

Because the Lobo will operate in the supersonic flight regime, it was necessary to consider the effects of supersonic wave drag on the Lobo. When considering the Lobo's role as a homeland defense interceptor, maximizing the response time to a potential threat is crucial to the Lobo's operation. When evaluating the dash distance, minimizing supersonic wave drag is critical to minimizing fuel burn and increasing the interception distance.

This supersonic parasite drag is due to pressure drag caused by shock formation on the body of the aircraft, a result of the way the aircraft's volume is distributed along the length of the fuselage [5]. To minimize this drag, the Lobo was designed to model a Sears-Hack body, which minimizes pressure gradient changes along the fuselage, reducing the drag effects of shock waves. The Lobo's frontal cross-sectional area distribution and distribution at Mach 1.6 are shown below in Figure 29. By minimizing wave drag effects of the fuselage, the utilization of a thicker airfoil that creates more wave drag over the wing can be justified.

To ensure the calculated wing sweep in preliminary design is enough to prevent the shock wave formed at the nose of the aircraft from reaching the main wing, the Lobo was tested using SU2's Euler solver. The pressure distribution at Mach 1.6, shown below in Fig. 28, shows that the mach cone formed at the nose does not reach the leading edge of the wing, verifying that the wing is within the Mach cone formed.

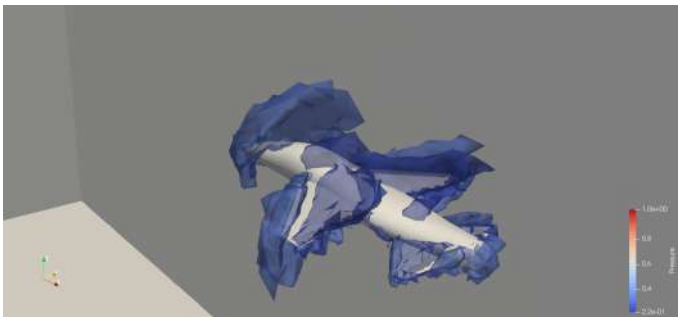

Fig. 28 Pressure distribution at Mach 1.6.

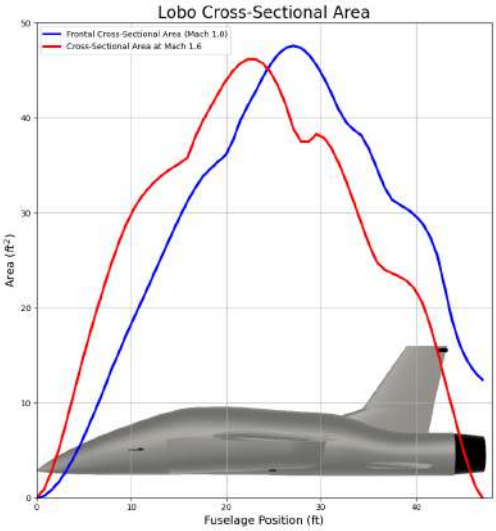

Fig. 29 Cross-sectional area distribution.

G. Drag Buildup

The Lobo has an S_{wet}/S_{ref} of 4.9, which is designed to reduce parasite drag. To further analyze the Lobo's aerodynamic performance, a tabulated drag buildup was performed using Equations 12.24 – 12.23 in Raymer [5] to determine the profile drag of the aircraft. Additionally, Hoerner's drag coefficients were used for the two AIM-120 AMRAAM missiles [17]. At dash conditions, the Delta Method was used to calculate supersonic wave drag caused by the formation of shock waves [18]. To determine $C_{D_{trim}}$ of the aircraft, Nicolai's Equations 22.5 – 22.8 were used [8]. The drag at each mission segment is tabulated in Table 14 below. For visual purposes, these components of drag at cruise are shown in Fig. 30. It can be seen that at the optimal cruise speed, the Lobo is flying just above the velocity for minimum drag, as parasite drag is only slightly greater than induced drag, illustrating the Lobo's aerodynamic efficiency.

Table 14 Lobo Tabulated Drag Buildup

Drag Category	**Mission Segment Drag Contribution**				
	Takeoff	Cruise	Patrol	Dash	Landing
C_{D_0}	0.0196	0.0187	0.0184	0.0014	0.0196
$C_{D_{0(flap)}}$	0.0107	0	0	0	0.0215
$C_{D_{0(wave)}}$	0	0	0	0.0385	0
C_{D_0} **(total)**	0.0304	0.0187	0.0184	0.052	0.0411
C_{D_i}	0.1131	0.0174	0.0246	0.0017	0.1569
$C_{D_{i(flap)}}$	0.0154	0	0	0	0.0215
$C_{D_{trim}}$	0.0135	0.0015	0.0001	0.004	0.0006
C_D **(total)**	**0.1723**	**0.0376**	**0.0421**	**0.0581**	**0.2202**

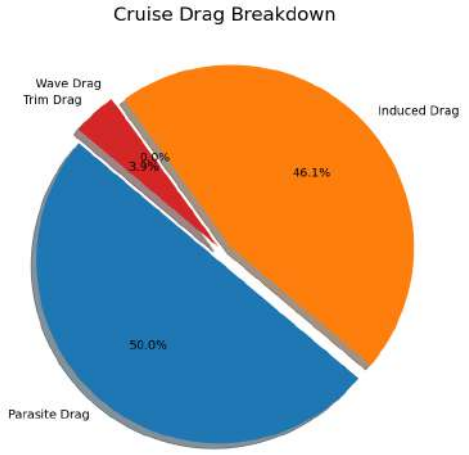

Fig. 30 Total drag breakdown for cruise

H. Aerodynamic Performance Analysis

To test the validity of the Lobo's aerodynamic design, and determine its aerodynamic capability, 3-D CFD was used to perform an analysis of the entire aircraft. SU2's Euler simulation provided a quick and accurate evaluation of the lift generated by the Lobo. Although viscous effects are not captured in this simulation, the lift values found from the pressure distribution provide a reasonable estimate in the transonic and supersonic regimes, which a Vortex Lattice Method cannot perform. Future testing of the Lobo's aerodynamic capabilities would include full aircraft CFD using a higher-fidelity method such as RANS. Using a higher-fidelity method would allow viscous effects to be considered and improve estimations in regard to leading edge root extension performance. However, this was not feasible in the scope of this project due to computational limitations on available technology.

For the transonic and supersonic mission segments of cruise, patrol, and dash, entire aircraft drag polars were created using lift data from SU2 and drag calculations from the tabulated drag buildup. This is shown below in Fig. 31, with the aircraft operating point indicated. These are the aircraft operating points for Mission One, which requires the Lobo to have full fuel weight. The operating points are tabulated in Table 15. Although the angle of attack at patrol is high, it is important to note that this is at the point when the Lobo has the largest amount of fuel, and decreases as the loiter continues and the Lobo burns fuel. These operating conditions show that the aerodynamic design of the wing was successful, allowing the Lobo to operate with a high L/D ideal for minimizing fuel burn, the main objective and driver of the Lobo's aerodynamic design.

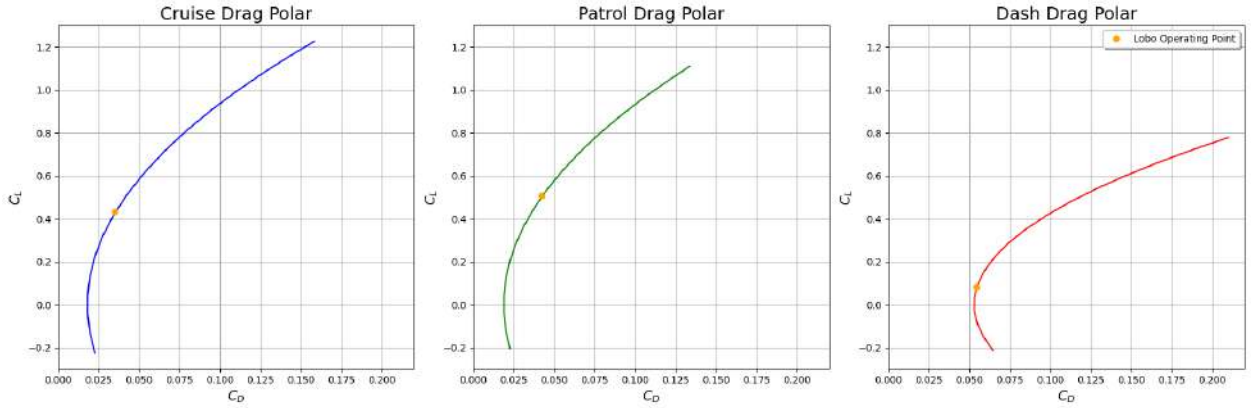

Fig. 31 Lobo drag polars for important flight regimes in Mission One.

Table 15 Operating Characteristics for Mission One Segments

Operating Characteristic	Cruise	Patrol	Dash
Required (C_L)	0.4315	0.512	0.08119
Angle of Attack [Degrees]	3.15	4.7	0.75
L/D	11.536	11.954	1.424

7. Performance, NB

This section will be an analysis of the requirements prescribed in the AIAA RFP [1] and the performance of the group's aircraft design. The requirements include three missions the aircraft must complete, field length requirements, specific excess power requirements, and a few more specific performance requirements.

A. Flight Envelope

It is important to know where the aircraft is able to operate. This is done by constructing a flight envelope. This consists of a composite of a stall line, a line of zero specific excess power, a line of the maximum dynamic pressure, and any other aircraft limitations. This is shown for the 1g case in Fig. 32(a). Additionally, it is desired to know how this changes when the aircraft is maneuvering or pulling g's. This can be visualized with the 5g flight envelope in Fig. 32(b). Both envelopes were created for the aircraft at MTOW. This means that this is the most constraining flight envelope case and that the aircraft will be able to operate at a wider flight regime as fuel burns off. The maximum Mach number of the aircraft is set at 1.6. This is largely due to engine inlet limitations and shock formation limitations. If the aircraft flies over Mach 1.6, the shocks from the nose will begin to reach the wing, and the engine inlets will limit the thrust that will be able to be produced.

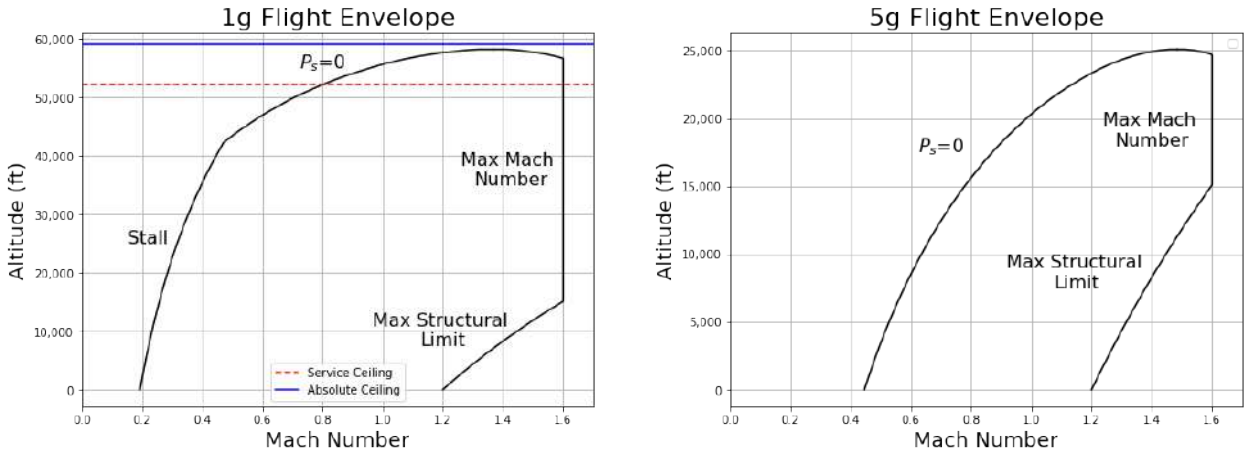

((a)) 1g flight envelope. **((b)) 5g flight envelope.**

Fig. 32 Comparison of 1g and 5g flight envelopes.

Another way that aircraft performance can be visualized is through the use of what are called doghouse plots. This is a graph with Mach number and turn rate on each axis. Specific excess power is plotted in ft/s. Also plotted are load factors and turn radii. The RFP requests these plots for 10,000, 30,000, and 50,000 ft. This can be seen in Fig. 33.

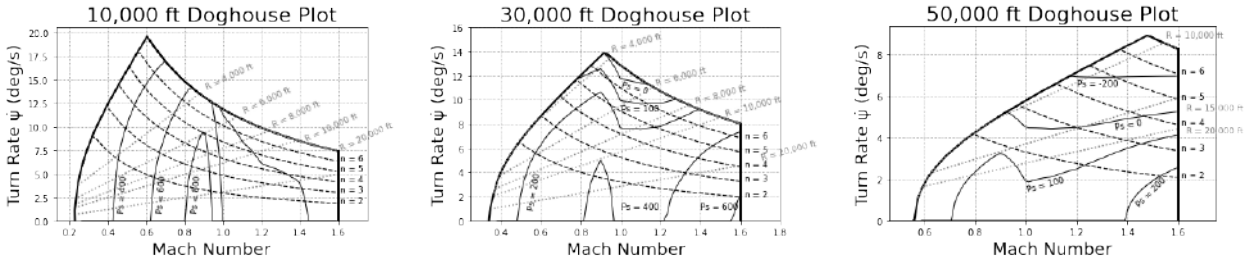

((a)) 10,000 ft. **((b)) 30,000 ft.** **((c)) 50,000 ft.**

Fig. 33 Doghouse plots for the lobo aircraft.

B. Field Lengths

This section will begin the field length analysis. The field length calculations were made modeling the use of spoilers and wheel braking. The calculated field lengths are shown in Table 17. The RFP requirement is that the aircraft can operate off of 8,000 ft NATO runways. The RFP specifies that calculations should be made for a runway at 4,000 MSL. The runway conditions are shown in Table 16.

Table 16 Braking Parameters under Different Runway Conditions

Runway Condition	DISA (°C)	μ_b	μ_{nb}
Dry	0	0.4	0.04
Icy	-15	0.05	0.015

The TOFL calculation was completed by conducting a time step integration for the aircraft accelerating to lift off speed, then clearing a 50 ft obstacle. Similarly, LFL was calculated by finding the approach distance simply from geometry by using a three deg glide slope and a 1.5 deg flare or touchdown angle. After that, the deceleration analysis is conducted in the same manner as the acceleration for takeoff. BFL reduces to the distance needed to accelerate to liftoff speed, then decelerate to a stop. For all three missions, the field lengths have been calculated for icy and dry conditions and are shown in Table 17. The aircraft meets the field length requirements.

Table 17 Field Lengths for Takeoff, Landing, and Balanced Operations

Runway	TOFL (ft)			LFL (ft)			BFL (ft)		
Condition	M1	M2	M3	M1	M2	M3	M1	M2	M3
Clear	4,100	3,100	4,100	2,750	2,750	2,800	3,350	2,450	3,350
Icy	3,750	3,000	3,750	5,550	5,500	5,700	7,400	6,200	7,400

C. Climb

The next aspect to be analyzed is the maximum rate of climb. The RFP requires the aircraft to climb from sea level to 35,000 ft constrained by a lateral distance of 4.8 nmi and a time to climb of one minute. This requirement is at half

internal fuel weight. The current estimate of the Lobo is that it can climb to 35,000 ft in a lateral distance of 3.75 nmi in 50 s. This meets the requirement in the RFP. This is done by using a constant Mach number climb at 0.9 until the aircraft hits a lateral distance of 1.5 nmi, then the aircraft transitions to a constant 45 deg climb. The Mach number bleeds down to about 0.6, which is well above stall speed at this weight and altitude. This climb trajectory can be visualized in Fig. 34. The aircraft has a thrust to weight ratio of more than one at the beginning of the climb which corresponds to the initial vertical segment of the plot.

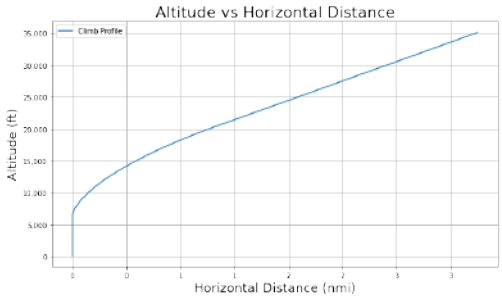

Fig. 34 Altitude vs. horizontal distance.

D. Cruise and Loiter

When choosing the flight conditions of the mission, there are methods to optimize the desired parameters. For cruise, loiter, and climb, $\frac{C_L}{C_D}$, $\frac{C_L^{\frac{3}{2}}}{C_D}$, and $\frac{C_L^{\frac{1}{2}}}{C_D}$ respectively can be plotted vs C_L to find the optimal flight condition for each case. To reiterate, finding the maximum $\frac{C_L}{C_D}$ will optimize range and this occurs at $C_L = 0.25$. Finding the maximum $\frac{C_L^{\frac{3}{2}}}{C_D}$ will optimize endurance and this occurs at $C_L = 0.42$. Finding the maximum $\frac{C_L^{\frac{1}{2}}}{C_D}$ will optimize fuel burn in climb and this occurs at $C_L = 0.75$. This can be seen graphically in Fig. 35. This can also be done numerically in the performance tool used to analyze the aircraft missions. For example, the cruise segment of a mission can be analyzed with a range of Mach numbers to find the Mach number that produces the lowest fuel burn. This is in fact a function of weight, but in most cases, this occurs at Mach 0.9 for the Lobo, or just before wave drag begins to become a factor.

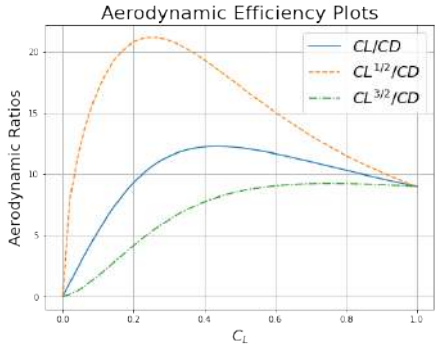

Fig. 35 Aerodynamic efficiency plots.

E. Altitude and Mach Number Trade Study

With a time stepping performance tool, it becomes feasible to do quick trade studies to optimize time or fuel burn. In this section, a trade study will be done on the first cruise segment of the first mission. This is shown in Table 18. The first column shows the Mach number selected and the second column shows how much fuel has been used in the mission at the end of the cruise segment being analyzed. It is important to note that this trade study is only valid at a specific weight and altitude. In this case, it is only valid at 35,000 ft and at the weight that the aircraft is from taking off at MTOW and climbing to 35,000 ft. For all missions, it is important to do this trade study, starting at the beginning and working through the mission. A Mach number of 0.90 was chosen to minimize fuel burn. Similarly, a cruise altitude can be studied. The results from this study were less pronounced. It can be seen from Table 19 that the altitude for lowest fuel burn occurs between 35,000 and 40,000 ft. The group found that for the 300 nmi segment in the DCA mission, 39,000 ft produced the lowest fuel burn.

Table 18 Mach Number Trade Study at 35,000 ft

Mach Number	Fuel Burn (lb)
0.8	1,240
0.85	1,180
0.9	1,140
1.0	3,180

Table 19 Altitude Trade Study at $M = 0.875$

Altitude (ft)	Fuel Burn (lb)
35,000	1,130
37,500	1,125
40,000	1,135
42,500	1,165
45,000	1,210

F. Mission Analysis

Three missions are included in the RFP. There is mission one, the defensive counter-air patrol mission, mission two, the point defense intercept mission, and mission three, the intercept/escort mission. Mission one is the constraining mission for the aircraft. The missions are shown in Tables 20, 21, and 22. With a 200 lb allowance of fuel for warmup and taxi, this puts total fuel burn for each mission to be 12,950 lb, 4,800 lb, and 12,500 lb respectively. Mission three is a variable mission. This means the amount of fuel will be fixed and the total range or capabilities of the aircraft will be reported. The Lobo currently has space for 13,000 lb of fuel. This tank size is set by the requirements for mission one.

Table 20 Mission One Specifications

Segment	Mach	Altitude (ft)	Fuel Burned (lb)	Drag (lb)	Time (hr)	Range (nmi)
Warm-up and Taxi	0	0	500	0	-	-
T.O. and Acceleration	0-0.78	0	550	5,000	-	-
Climb and 300 nmi Cruise	0.9	39,000	1,550	2,373	0.61	300
Four hr Loiter and Acceleration	0.65	35,000	7,100	2,050	4.0	1,600
100 nmi Dash	1.6	35,000	2,300	6,500	0.11	100
Combat Maneuvers	1.2 and 0.9	35,000	1,050	15,400	0.02	10
400 nmi Cruise	0.9	35,000	900	1,200	0.76	400
Reserve	0.3	0	900	1,150	0.5	65

Table 21 Mission Two Specifications

Segment	Mach	Altitude (ft)	Fuel Burned (lb)	Drag (lb)	Time (hr)	Range (nmi)
Warm-up and Taxi	0	0	500	0	-	-
T.O. and Acceleration	0-0.78	0	100	3,850	-	-
Climb and 200 nmi Dash	1.6	35,000	4,600	8,900	0.22	200
Combat Maneuvers	1.2 and 0.9	35,000	1,000	13,550	0.02	10
200 nmi Cruise	0.9	49,000	450	1,300	0.37	200
Reserve	0.3	0	900	1,250	0.5	65

Table 22 Mission Three Specifications

Segment	Mach	Altitude (ft)	Fuel Burned (lb)	Drag (lb)	Time (hr)	Range (nmi)
Warm-up and Taxi	0	0	382	0	-	-
T.O. and Acceleration	0-0.78	0	550	5,000	-	-
425 nmi Dash	1.6	35,000	9,850	10,100	0.52	425
300 nmi Escort	0.5	35,000	1,400	2,200	1.04	300
725 nmi Return	0.9	49,000	1,750	1,400	1.40	725
Reserve	0.3	0	900	1,300	0.5	65

G. Requirement Analysis

The aircraft design must meet all specified requirements. In the section before, it was discussed that the aircraft is able to complete all three missions. This satisfies the intercept mission radius requirement of 200 nmi and the DCA mission CAP endurance at 300 nmi radius of four hours. The maximum Mach number at 35,000 ft of 1.6 is also met within the missions. The next requirements are for specific excess power which are tabulated in Table 23. All specific excess power requirements are met. The sustained load factor of 5.0 g at maximum thrust at Mach 0.9 at 15,000 ft was exceeded doing the combat maneuvers which occurred at the structural limit of 7.0 g, so this requirement is met.

Table 23 Specific Excess Power at Mach 0.9

Configuration	P_s Requirement (ft/s)	P_s Results (ft/s)
1-g, Sea Level, Military Thrust	200	420
1-g, 15,000 ft, Military Thrust	50	330
1-g, Sea Level, Maximum Thrust	700	1,110
1-g, 15,000 ft, Maximum Thrust	400	780
5-g, Sea Level, Maximum Thrust	300	980
5-g, 15,000 ft, Maximum Thrust	50	530

The instantaneous turn rate requirement has been met, achieving an instantaneous turn rate of 18.1 deg/s using a lifting load of $n = 9.5g$. It is important to note that this value is over the yield limit of the aircraft, but under the ultimate limit of the aircraft. While staying under the yield limit the Lobo can achieve a maximum instantaneous turn rate of 16.2 deg/s. A future design iteration would be conducted to include more titanium in the structure of the aircraft in order to increase the yield limit such that the turn can be conducted under the yield limit. Another solution to be explored would be to include maneuvering slats and flaps to greatly increase C_{Lmax}.

8. Stability & Control, AM

A. Dimensions

A top and side view of the horizontal and vertical stabilizer are given on Fig. 6. An all moving tail configuration was selected for this aircraft in order to increase overall maneuverability and reduce trim drag by removing the drag associated with the flap mechanism.

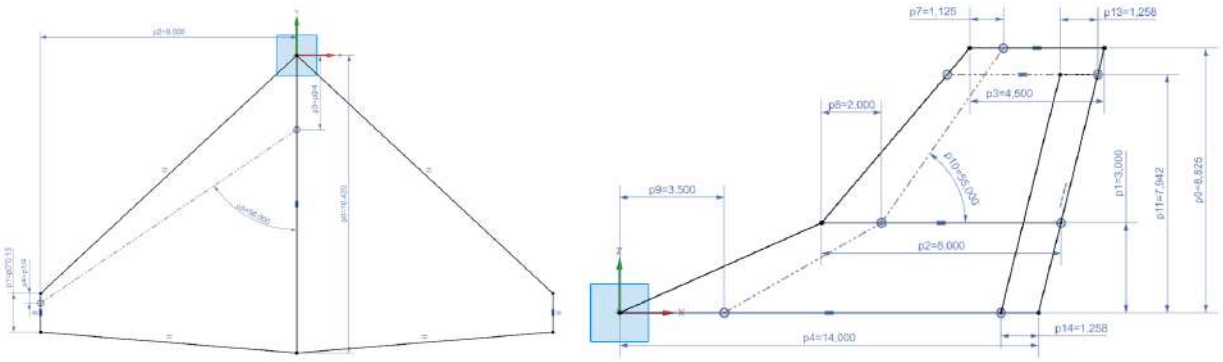

Fig. 36 Horizontal and vertical stabilizer top + side view (in.).

B. Control Surface Sizing

A crosswind takeoff and landing analysis with an uneven ordnance and fuel load was conducted in Fig. 37 using equations from Roskam part seven. The analysis was conducted with the assumption of half of the fuel loaded to one half of the aircraft only. It was found that the Flaperons would need to span four ft along the wing in order to be able to trim the aircraft in the most severe crosswind landing case. In this circumstance, this guarantees that even if half of the fuel tanks cannot be loaded on to the aircraft, the aircraft can still takeoff and land in even severe crosswinds. This requirement sized the flaperon span, while the chord was limited due to structural concerns at the tip of the wing.

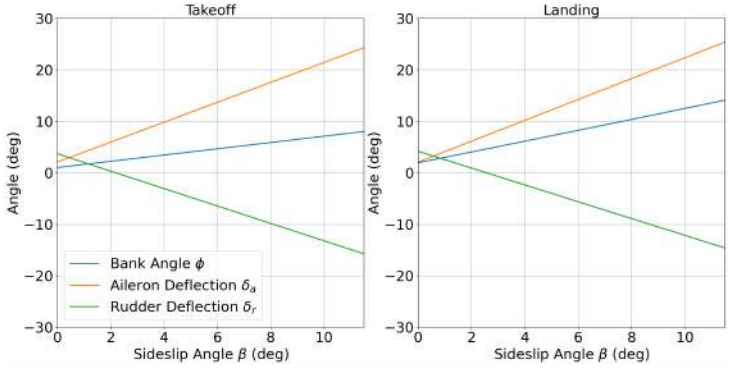

Fig. 37 Crosswind trim triangle with uneven ordnance and fuel load.

In addition, the rudder was sized through similarity analysis with the F-5E, and the design was validated by both the crosswind analysis and dynamic stability analysis. Dimensions for both the rudder and flaperon are given on Table 24.

Table 24 Control Surface Dimensions

	Rudder	Flaperon
Span Ratio	0.9	0.27
Span (ft)	6.84	4
Chord Ratio	0.3	0.3
Deflection Range	+25/-25	+30/-30

C. Aircraft Trim

A primary function of the horizontal stabilizer is to trim the aircraft throughout the mission. With an all moving tail configuration this is achieved through deflection of the horizontal stabilizer, aka modification of the incidence angle, which provides a balancing moment force from the tail that counteracts the overall pitching moment of the aircraft. In order for the aircraft to be in trim, the pitching moment must equal zero. To solve for trim conditions, equations from Roskam Part seven [6] were used to determine the necessary angle of attack and tail incidence required to balance the moments of the aircraft and meet the C_L requirements. Fig. 38 shows the trim diagrams for each segment in mission one. Since the trim values are all fairly low, this is an indication of low trim drag.

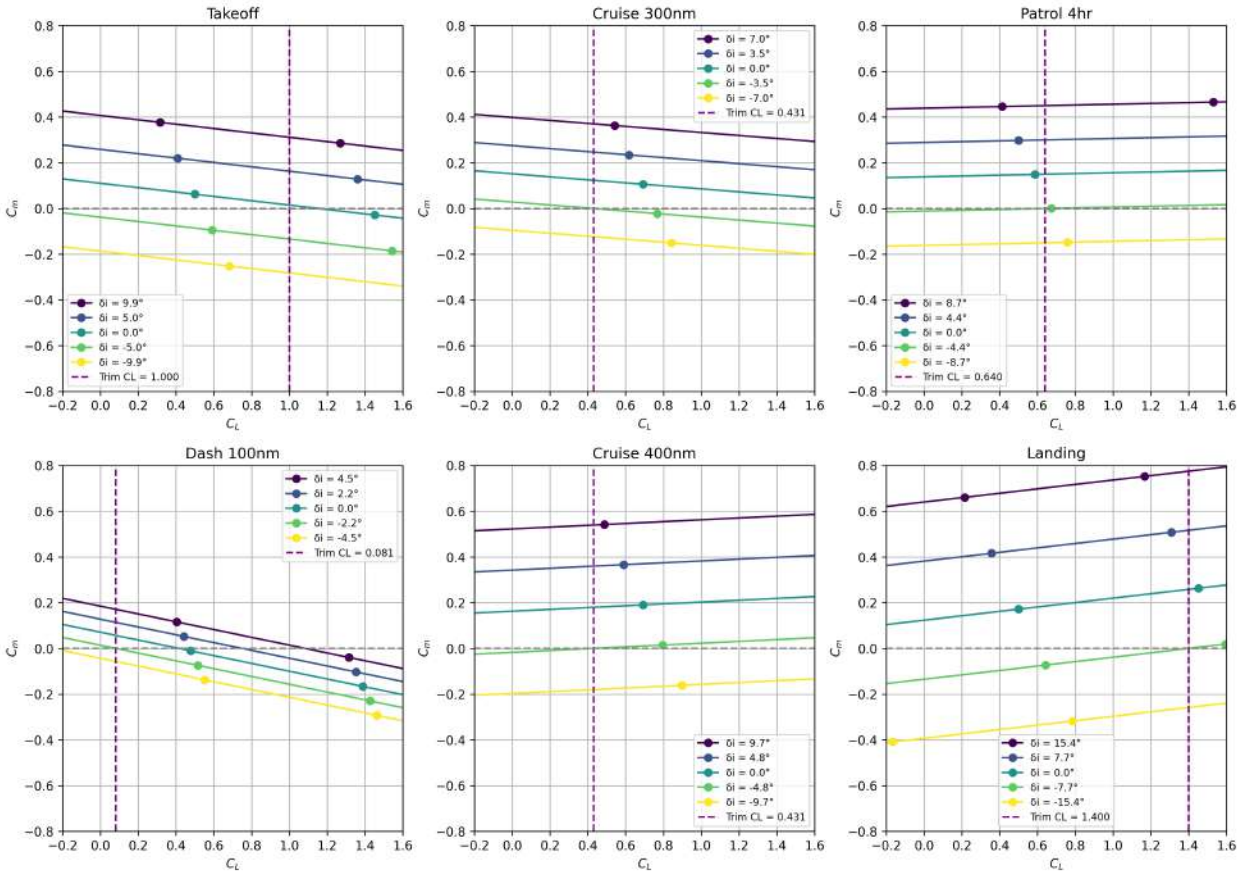

Fig. 38 Trim diagrams for mission one segments.

D. Design Evaluation

The stability and control characteristics of the team's aircraft were evaluated using AVL for subsonic flight conditions. In addition, the lift and drag profiles for the wing were evaluated in SU2 by aerodynamics. The stability and control derivatives were then checked against derivatives calculated using methods from Roskam part six and part seven [7], [6] and Roskam parts six and seven were used to estimate the stability and control derivatives during transonic and supersonic flight with Prandtl-Glauert compressibility corrections. The neutral point location, and static margin were calculated using data from Mass Properties. The neutral point, center of gravity location, and static margin throughout various stages of mission one are given in Table 25, and The stability and control coefficients for various segments of Mission one, are given in Tables 26(a) and 26(b). It can be seen that the team's aircraft satisfies the static margin constrain outlined in the RFP [1] as well as all constraints necessary for lateral static stability, that being $C_{y_\beta} < 0$, $C_{n_\beta} > 0$, and $C_{l_\beta} < 0$.

Table 25 Neutral Point (NP), Center of Gravity (CG), and Static Margin (S.M.) across Mission One Segments

	NP (%MAC)	CG (%MAC)	S.M. (%MAC)
Takeoff	51.4	41.8	9.6
Cruise 300 nmi @ M=0.85	50.5	43.9	6.6
Patrol Four hrs @ M=0.67	49.6	51.3	-1.7
Dash @ M=1.6	69.5	52.4	17.1
Cruise Back 400 nmi @ M=0.85	50.5	54.5	-4.0
Landing	51.4	61.0	-9.6

Table 26 Control and Stability Derivatives Across All Mission Segments

((a)) Control Derivatives

Derivative	TO	Cruise300	Patrol4hr	Dash100	Cruise400	Land
$C_{L_{\delta_i}}$	4.581	6.132	5.303	4.477	6.132	4.581
$C_{m_{\delta_i}}$	-0.438	-0.404	0.093	-0.764	0.245	0.442
$C_{Y_{\delta_a}}$	0.000	0.000	0.000	0.000	0.000	0.000
$C_{l_{\delta_a}}$	-0.113	-0.164	-0.135	-0.107	-0.164	-0.113
$C_{n_{\delta_a}}$	0.024	0.019	0.019	0.004	0.018	0.030
$C_{Y_{\delta_r}}$	0.326	0.170	0.271	0.742	0.170	0.326
$C_{l_{\delta_r}}$	0.020	0.026	0.034	0.133	0.026	0.008
$C_{n_{\delta_r}}$	-0.033	-0.085	-0.117	-0.372	-0.086	0.034

((b)) Stability Derivatives

Derivative	TO	Cruise300	Patrol4hr	Dash100	Cruise400	Land
ϵ_α	0.346	0.414	0.380	0.279	0.414	0.346
C_{L_α}	4.581	6.132	5.303	4.477	6.132	4.581
C_{m_α}	-0.438	-0.404	0.093	-0.764	0.245	0.442
C_{L_q}	9.308	14.846	12.521	15.623	16.578	10.818
C_{m_q}	-7.434	-8.383	-8.055	-10.411	-8.839	-7.345
C_{Y_β}	-0.853	-0.806	-0.910	-0.910	-0.806	-0.853
C_{l_β}	-0.304	-0.1	-0.318	-0.310	-0.308	-0.295
C_{n_β}	0.511	0.456	0.531	0.472	0.456	0.513
C_{Y_p}	0.202	0.051	0.103	0.006	0.047	0.259
C_{l_p}	-0.342	-0.474	-0.400	-0.081	-0.473	-0.351
C_{n_p}	-0.462	-0.170	-0.262	-0.030	-0.160	-0.576
C_{Y_r}	0.961	0.851	1.000	0.881	0.850	0.965
C_{l_r}	0.040	0.036	0.042	0.034	0.036	0.040
C_{n_r}	-0.662	-0.504	-0.619	-0.469	-0.500	-0.714

E. Dynamic Stability Analysis

Using the Stability and Control derivatives from earlier as well as equations from Roskam Part seven and Nelson [6], [19], A dynamic stability analysis was conducted on the aircraft during the 300 nmi cruise portion of mission one in order to determine whether it displays stable dynamic stability. By constructing the plant matrix outlined in Nelson for both the longitudinal and lateral modes, it was found that all eigenvalues of these plant matrices were complex, with their real parts all being strictly negative. This indicates that for any longitudinal or lateral mode, given an initial

perturbation the aircraft will return to equilibrium as time goes to infinity. The specific time dependent responses to various perturbations was graphed in Fig. 39(b), which demonstrates the aircraft performing a Short Period, Dutch Roll, and Phugoid maneuver. In addition, various properties of these dynamic stability modes are given in Table 27. The aircraft currently meets level one MIL Spec requirements for a Class IV Category A aircraft in both Rolling and Spiral modes, and meets the level two requirements for the Short Period, Phugoid, and Dutch Roll modes.

The roll response for the aircraft was graphed in Fig. 39(a). The team's aircraft currently far exceeds the MIL-HDBK-1797 requirement for an interceptor to complete a 90 deg turn in 1.3 s.

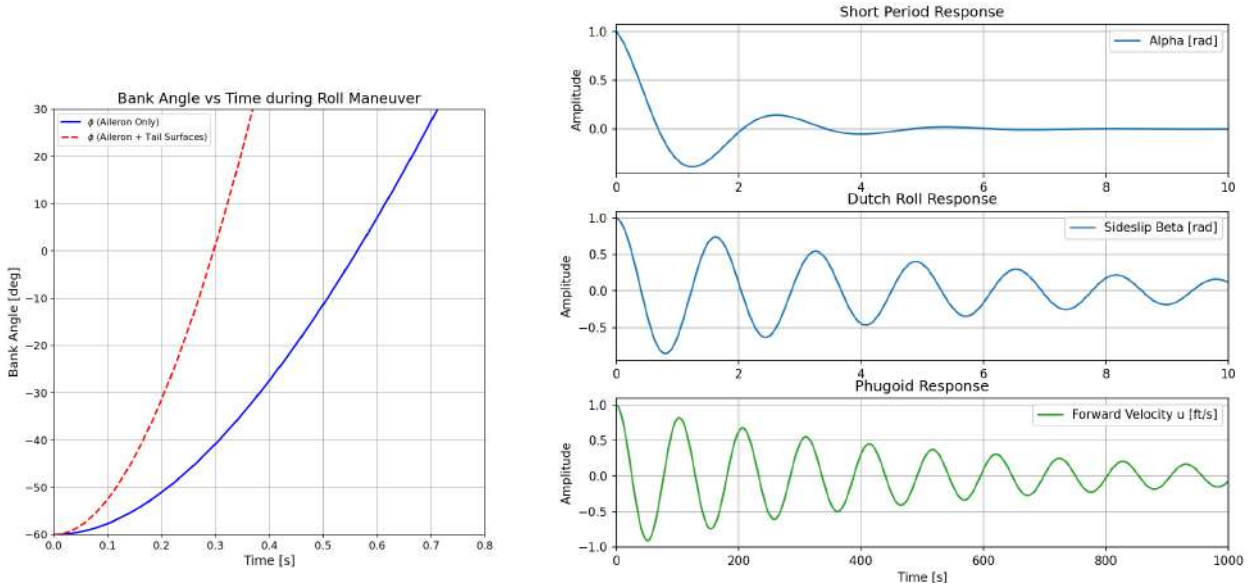

((a)) Roll rate with/without tail. **((b)) Short period, dutch roll, and phugoid modes.**

Fig. 39 Lateral-directional stability and control analysis.

Table 27 Dynamic Stability Characteristics

Mode	**Damping Ratio, ζ**	**Natural Frequency, ω_n (rad/s)**	$t_{1/2}$ **(s)**	$N_{1/2}$	**Period, T (s)**
Short-period	0.333	2.41	0.860	0.331	2.68
Phugoid	0.031	0.061	362.2	3.525	103.0
Dutch roll	0.049	3.973	3.560	2.255	1.581
Rolling	N/A	N/A	0.489	N/A	N/A
Spiral	N/A	N/A	28.69	N/A	N/A

9. Structures, MW

Following mission requirements of the Lobo, structural design and materials were chosen based on existing fighter and interceptor designs. Finite element models were used to validate design choices and provide insight into the viability of the structure. Figure 40 shows the final design of the main structure.

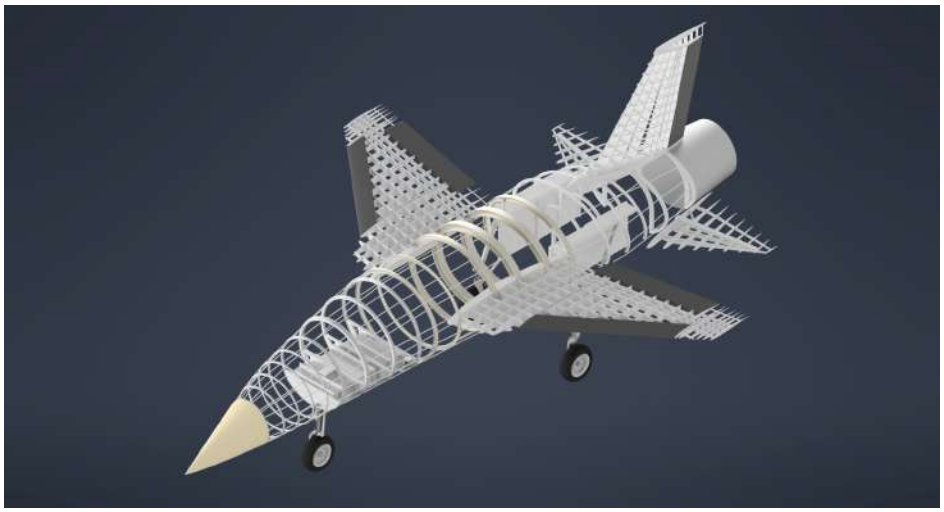

Fig. 40 Image of the full structure of the aircraft.

A. Materials

As the aircraft must be low cost and sustain high loads, common aircraft-grade materials were chosen to be candidates for the structure, as they can be sourced at low cost and tend to have a higher modulus than similar non-aerospace alloys. Table 28 contains common aircraft materials that were candidates for the structure of this aircraft [20–30].

Table 28 Table of Materials to Consider for the Aircraft

Material	Young's Modulus (GPa)	Cost ($ per kg)
6061 Aluminum	68.9	3.00 - 5.00
7075 Aluminum	70	10.00 - 20.00
7050 Aluminum	70-80	5.00 - 10.00
4130 Alloy Steel	205	1.25 - 5.56
1045 Cold Rolled Steel	200	13.00
Carbon Fiber Composite	185 - 588	3.50 - 34.00
Fiberglass Composite	51.7 - 86.9	10.00 - 20.00

For the wing skin, horizontal stabilizer skin, vertical stabilizer skin, lower-load spars, and longerons, 7050-T6 Aluminum was chosen for its relatively lower cost and density when compared to 7075 Aluminum Alloys. For the nosecone, a fiberglass composite was chosen as it requires a non-conductive material to not interfere with the radar. For the tail skin, 6061 Aluminum was chosen for its low cost and weight as well as a high enough melting point to withstand burner and exhaust temperatures. To save weight, a low-modulus carbon fiber composite with a $[0, 90, \pm 45]_s$ layup was chosen for the fuselage skin and control surfaces. As this is an all-weather interceptor, a lightweight aluminum weave will be included on the outer layers of the composite to maintain a proper Faraday Cage and protect internal components from lightning strikes.

B. Design

1. Fuselage

As the skin of the fuselage was chosen to be a carbon fiber composite, a semi-monocoque design was used. In the design of the aircraft, a majority of tensile and compressive forces are carried by this composite skin, shown in Fig. 41(a), with sparse longerons in place for additional strengthening. The longerons are spaced to minimize weight while providing proper support for the skin to resist buckling when subjected to aerodynamic pressure forces. As the landing gear is placed within the fuselage, the landing gear housing is integrated into the fuselage structure. Engine frames were designed to allow the engine to be lowered without the need for structural disassembly. They are shown in Fig. 41(b). Frames located forward of the nose landing gear were sized and spaced using similarity analysis with the F-18. All other frames were sized and placed using similarity analysis with the F-22. To reduce weight, larger frames were designed using flanges and webs. The full fuselage structure is shown in Fig. 41(c).

(a) Carbon fiber skin used for the fuselage

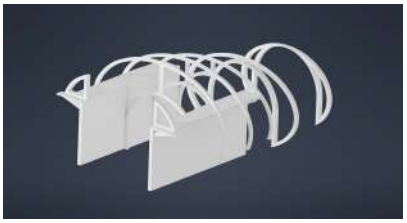

(b) Frames surrounding engine and main gear.

(c) Internal fuselage structure.

Fig. 41 Internal structural features of the Lobo fuselage.

2. Wings

To first determine a needed moment of inertia for the wings, an Euler Bending approximation was used. The bending moment, M_y, was chosen to be 1,669,500 ft-lb, resulting from a 10.5 g load placed at 40% span. The stress, σ, was chosen to be 76,000 ksi as this is the UTS of 7050-T6 aluminum. The distance from the neutral axis, z, was chosen to be 0.5 ft as this height can be contained within most of the wing. The minimum moment of inertia was found to be 220 in^4.

Initial sizing and placement of the ribs and spars was performed using similarity analysis with the F-16. After performing a finite element analysis (FEA) on the wings, additional ribs and spars were added to address stress and buckling concerns. The final design of the wing uses 17 spars and 20 ribs. A combination of Ti-6AI-4V and 7050-T6 Aluminum was used in the construction of the wing to minimize cost while properly supporting critical areas, such as the wingtip.

Typical of most wing designs, pressure forces are greatest near the wing root. As this results in lower pressure forces experienced in the skin near the tip of the wing compared to the root, a tapered wing skin was used. The skin quadratically reduces from a thickness of 0.5 inches at the wing root to 0.05 inches at the wing tip. Additional stiffening is used in the wing skin due to buckling concerns in high-load maneuvers.

The finalized design of the wing is shown in Fig. 42. Further design iterations will be performed to reduce weight and increase the performance of the structure.

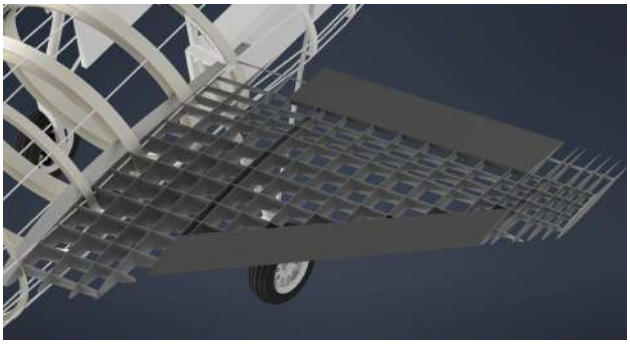

Fig. 42 Close-up of the wing structure.

3. Tail

The vertical stabilizer was designed using similarity analysis with the F-16. Additional lightweight spars were placed to resist buckling at high airspeeds. The horizontal stabilizers were designed using similarity analysis with the F-22 with additional structure used due to the aluminum skin used on the Lobo. As the horizontal stabilizer is an all-moving control surface, additional lateral support was needed near the root to transfer loads throughout the structure and prevent stress concentrations near the main spar. The finalized structure is shown in Fig. 43.

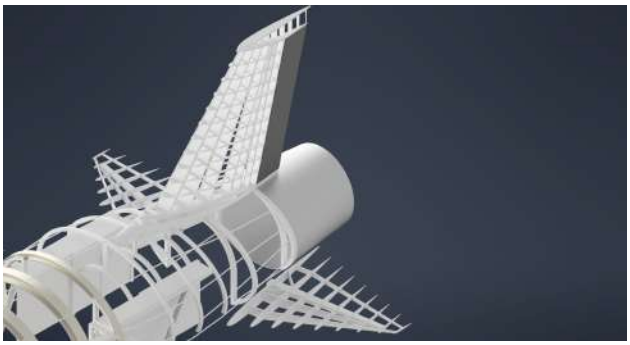

Fig. 43 Image of the tail structure of the Lobo.

C. FEA

Finite Element Analysis (FEA) was used on the wing structure to ensure that all structural members were performing as expected. Figure 44 depicts an analysis of the wing when subjected to the maximum design load. Figure 45 contains the titanium structures (top left) and aluminum structures (top right) within the wing. Resulting from these simulations, the largest calculated stress was 566.6 N/mm^2, which occurred within a titanium spar and results in a safety factor of 1.68 for UTS. The highest stress seen in the aluminum was 348.3 N/mm^2 and yields a safety factor of 1.50. These results demonstrate the effectiveness of the wing structure for high loads and indicate that possible cost and weight reductions can be made to this structure. Figure 45 show the internal (bottom right) and external (bottom left) stress distribution for the 16.2 deg/s turn rate. As these loads are smaller than the maximum load case, they were not used as design and materials drivers.

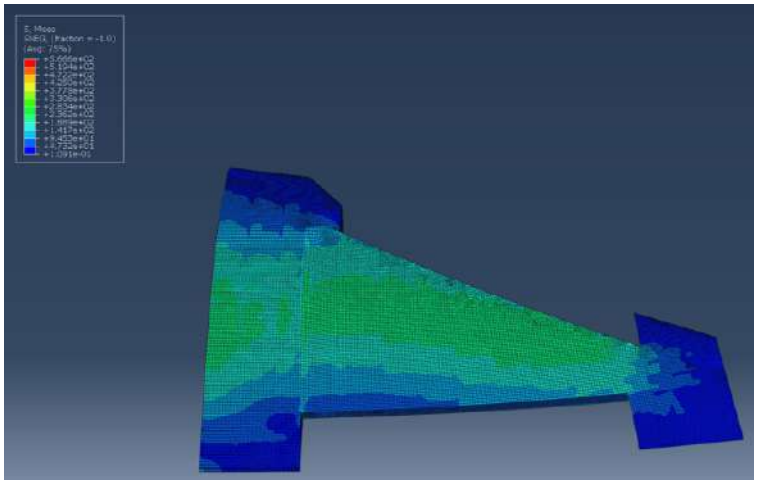

Fig. 44 FEA of full wing structure at 10.5 g (max load).

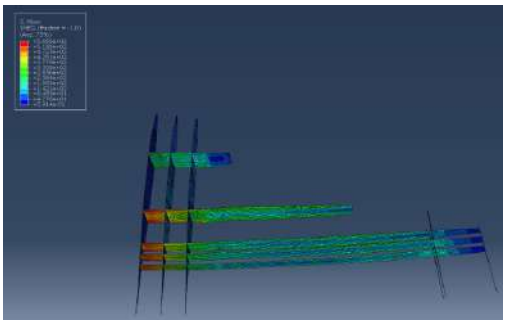

(a) Internal titanium wing structure at 10.5 g.

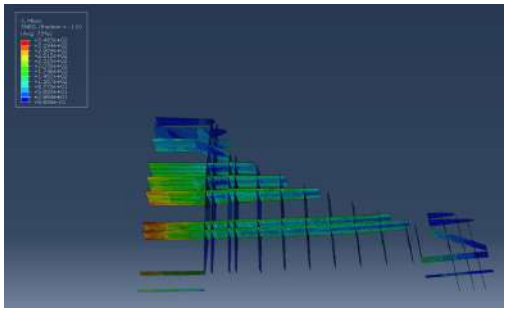

(b) Internal aluminum wing structure at 10.5 g.

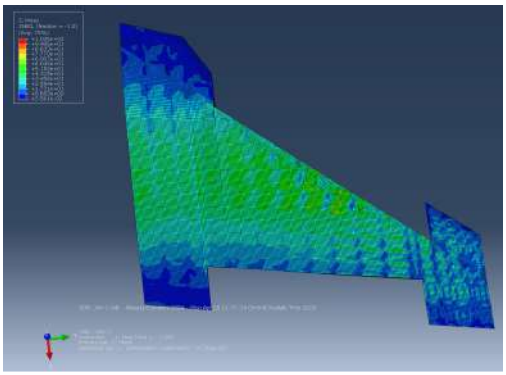

(c) Full wing structure at 16.2 deg/s turn rate.

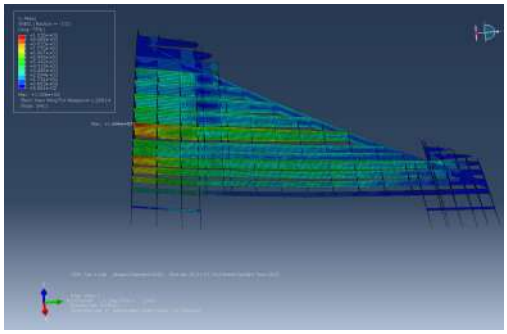

(d) Internal structure at 16.2 deg/s turn rate.

Fig. 45 FEA results of wing and internal structures under load cases.

D. Survivability

Due to the weight and cost restrictions on the aircraft as well as the lack of a human pilot, pressurization was not used and no special armor or structural arrangements were considered. As the structure will need to be rated to a high g-Load, it is possible that components can take damage without a total loss of structure, assuming that the aircraft is not subjected to high-load maneuvers after damage occurs. As the composite skin will be constructed with fibers running the length of the fuselage, it is possible that nearby fibers can remain intact if small damage occurs to the skin. While stresses will increase on these nearby fibers, they will not lose all load-carrying capacity and can allow the plane to remain intact, albeit with a large reduction in maximum load. Damage to frames can be withstood if webs remain intact and if the damage does not result in large crack formation in high-load areas, such as the engine and wing frames.

10. Loads and Dynamics, MW

A. Evaluation

To graphically demonstrate the structural flight envelope of the planned aircraft, a V-n diagram was used, shown in Fig. 46. This plot includes a safety factor of 1.5 for maximum g-loads. The structure is designed to withstand a maximum dynamic pressure of 2,133 psf in a dive with ultimate tensile strength (UTS) occurring at 1.5 times the dive loads to meet RFP requirements [1].

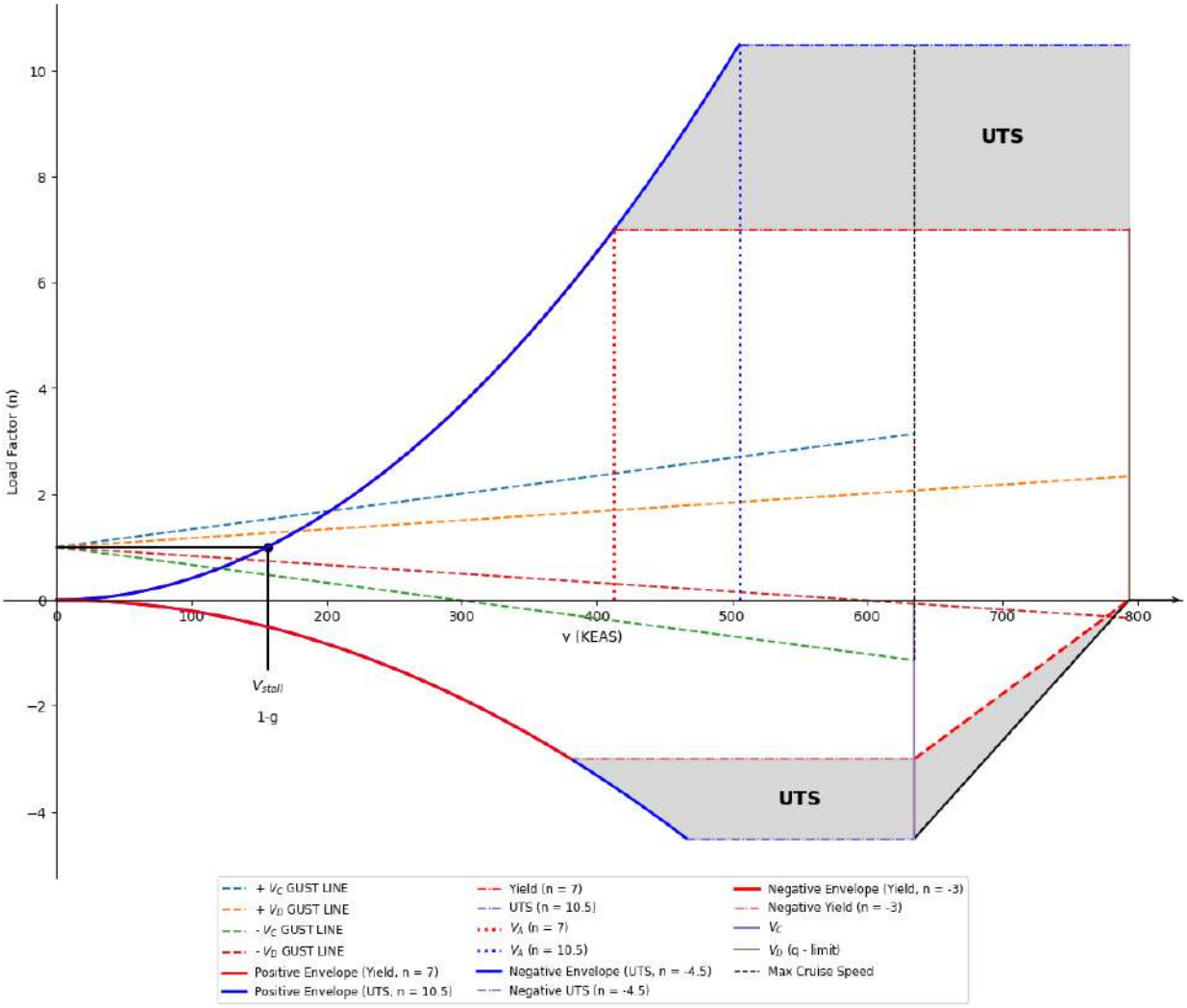

Fig. 46 Airspeed vs load factor plot for the chosen variant.

Due to the required maneuver loads and flight speed, gust loads are negligible. The normal operating conditions of the aircraft will limit it to +7 g and -3 g for all maneuvers, which will keep the structure below the yield stress and will not cause any permanent deformations to occur.

B. Load Path

Figure 47(a) depicts the typical load path experienced in flight, where the skin transfers aerodynamic loads to the structure, which then passes it to the center of gravity. Figure 47(b) depicts the load paths of control surfaces. Figure 47(c) depicts the load path of the landing gear, where the gear will transfer loads to the housing which will then transfer loads to the structure. Further analysis of the locations of torque boxes will need to be performed, especially around the wing and tail sections.

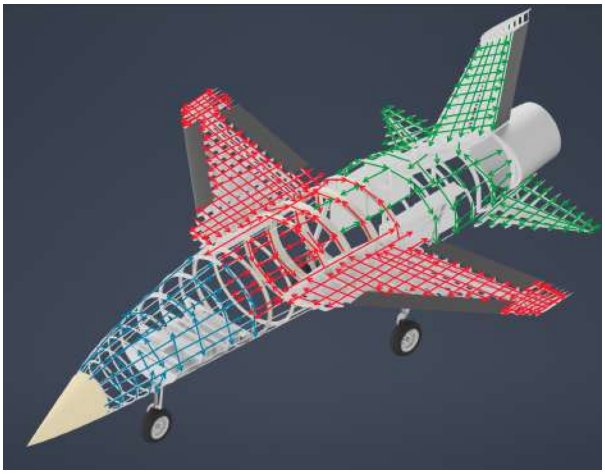

(a) Load path for nominal flight loads.

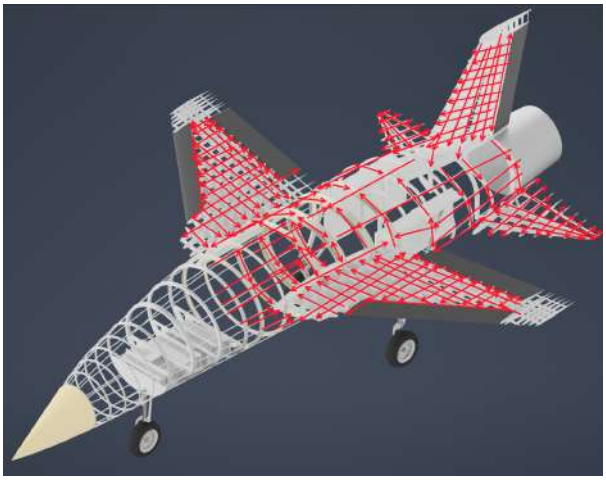

(b) Load path for control surfaces and flaps.

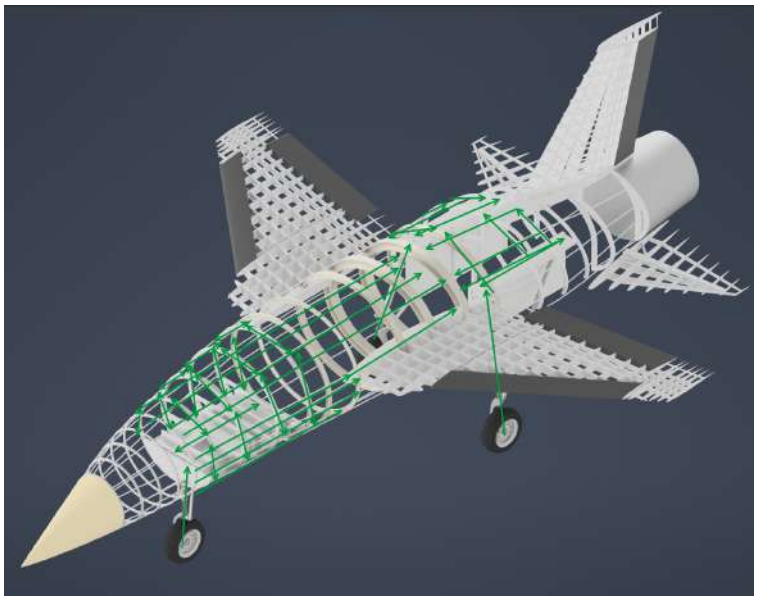

(c) Load path for landing gear.

Fig. 47 Load path visualizations for key flight and structural scenarios.

C. Load Cases of Interest

1. Maneuvering Loads

To meet RFP requirements, the aircraft was designed to withstand a positive load of 10.5 g and a negative load of -4.5 g at UTS [1]. Yield strength was chosen to occur at a positive load of 7 g and a negative load of -3 g to minimize weight of the structure. Initial loading distributions were calculated using Schrenk's approximation and were used to begin initial sizing of the wing structures. After performing finite element analysis on the wing, it was found that wingtip deformations occurred at high loads, which resulted in a varying angle of attack across the wing. To address this, a new lift approximation was developed to account for this deformation as well as incorporate the leading edge extension vortices generated at high angles of attack. To better match the performance of the wing in simulations, this new approximation was averaged with Schrenk's approximation, resulting in the lift distributions shown in Fig. 48. These distributions were then used to generate shear and bending moment diagrams for the wings. Fig. 49 show the derived distributions with the incorporation of loads from the armaments. Table 29 contains the calculated shear and bending moments at the fuselage location for each of the four load cases.

Table 29 Calculated Loads Using Lift Approximation

Load Cases	Shear at Fuselage (lb)	Bending Moment at Fuselage (ft-lb)
10.5 g	-53,050	237,000
7 g	-34,920	162,060
-3 g	12,280	-69,380
-4.5 g	18,420	-104,080

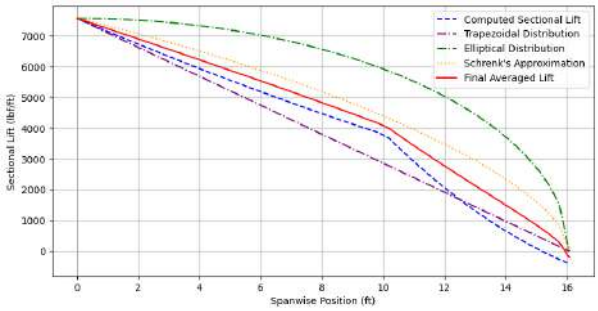

(a) Wing loading for 10.5 g UTS.

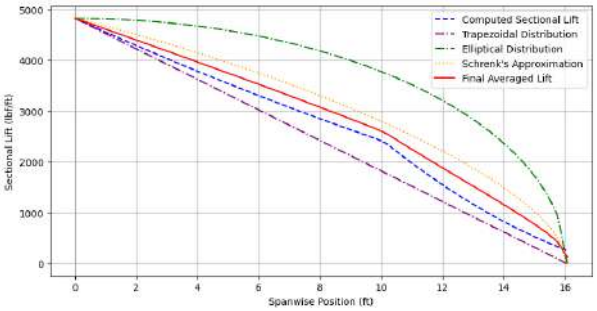

(b) Wing loading for 7 g yield strength.

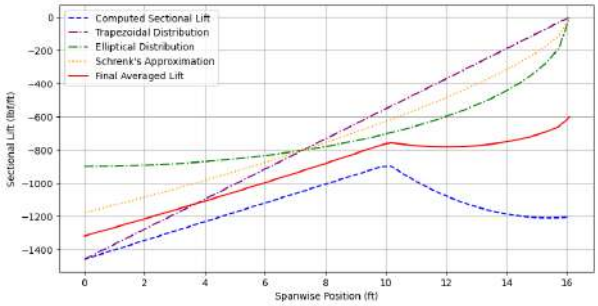

(c) Wing loading for -3 g yield strength.

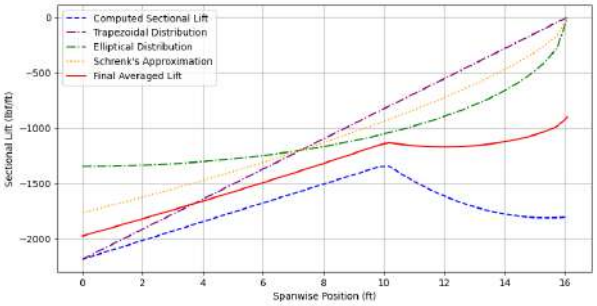

(d) Wing loading for -4.5 g UTS.

Fig. 48 Approximate wing loading distributions for positive and negative load cases.

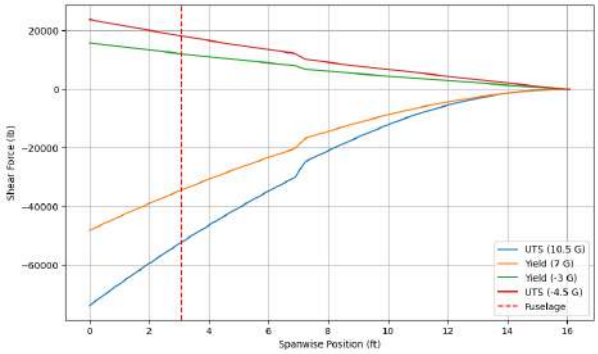

(a) Shear distribution using averaged lift approximation.

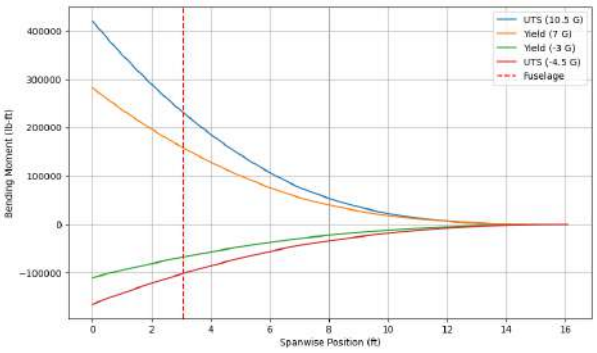

(b) Bending moment distribution using averaged lift approximation.

Fig. 49 Approximate structural load distributions along the wing span.

2. Landing

The maximum landing load was chosen to be 2.5 g at MTOW to simulate an emergency landing immediately after takeoff. Permanent deformation and buckling of the landing gear structure occurs at 3.75 g to account for a safety factor of 1.5. The expected maximum load for this case is 40,000 lb. Wing shear and bending moment for this scenario are depicted in Figs. 50(a) and 50(b). Fuselage shear and bending moment are shown in Figs. 50(c) and 50(d). The team used these values to size components within the wing and fuselage structures.

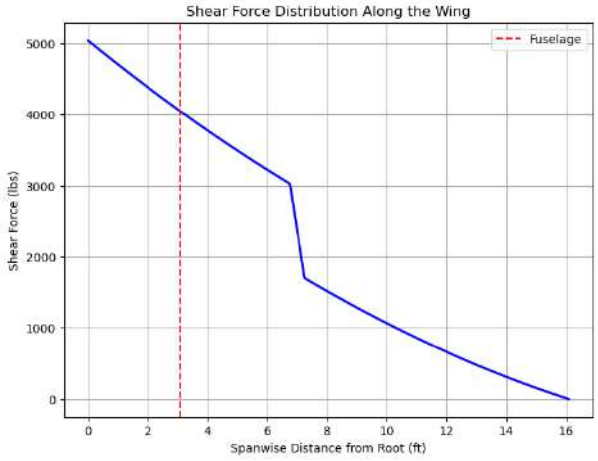

(a) Shear distribution in the wing at max landing load.

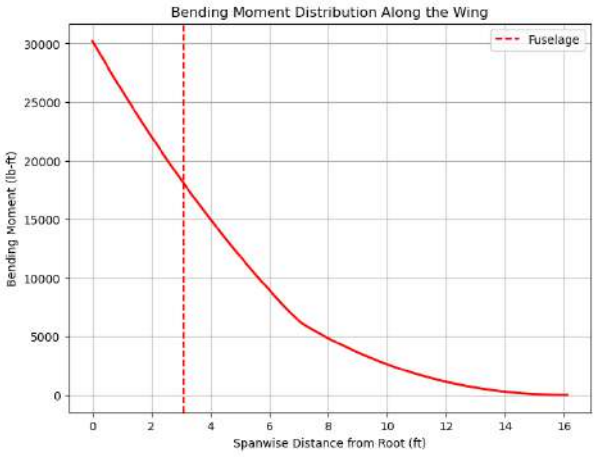

(b) Bending moment in the wing at max landing load.

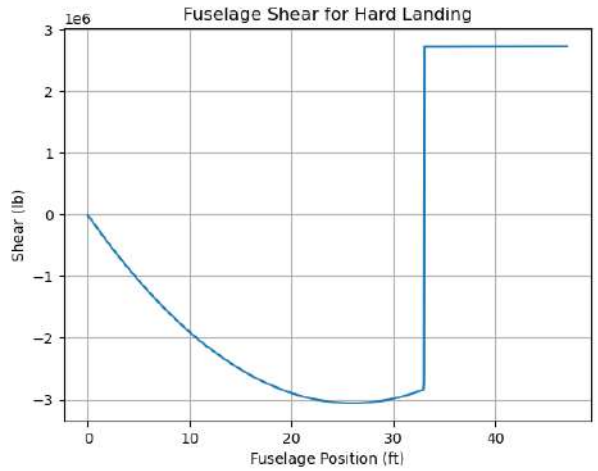

(c) Shear distribution in the fuselage at max landing load.

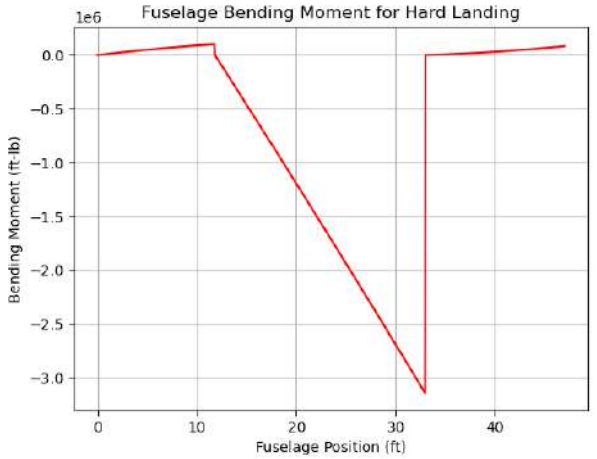

(d) Bending moment in the fuselage at max landing load.

Fig. 50 Structural load distributions at maximum landing conditions.

3. Braking

Due to tire restrictions, the maximum braking load that can be achieved is 23,430 lb. Using this value, a shear and bending moment distribution was generated, shown in Figs. 51 and 52. As these values did not exceed shear and bending moments for the hard landing, they were not chosen to be design drivers of the fuselage.

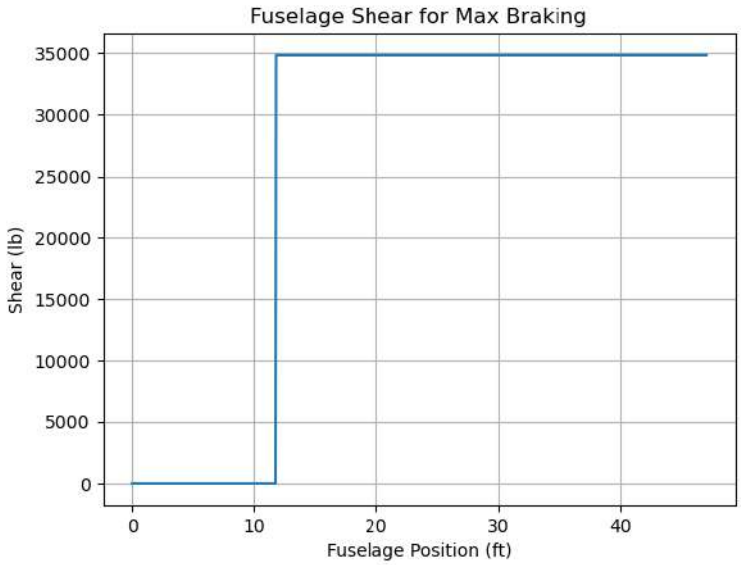

Fig. 51 Plot of shear distribution in the fuselage at maximum braking load.

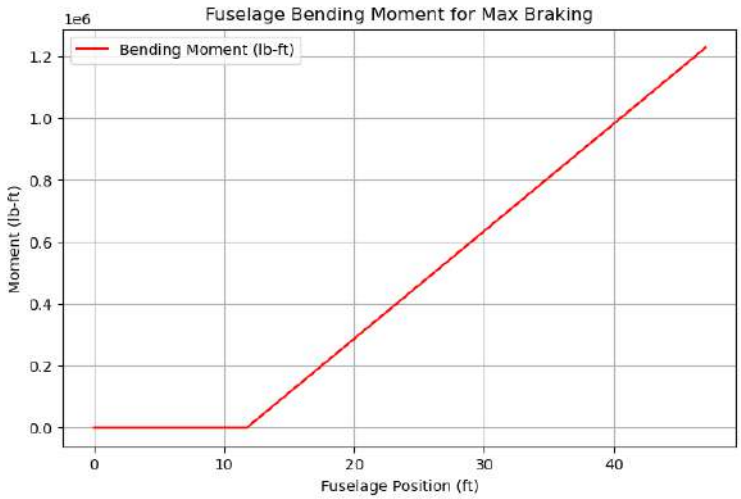

Fig. 52 Plot of bending moment distribution in the fuselage at maximum braking load.

11. Mass Properties, MR

A. Methodology

To determine the most appropriate methodology for estimating the weights of various aircraft components in the interceptor design, a trade study was conducted comparing estimation techniques from established aerospace design sources, including Raymer [5], Roskam [31], and Nicolai [8]. Each methodology was applied to the F-16, and the resulting component weights were compared against publicly available reference data. The analysis indicated that Roskam's GD method had yielded the closest match to known values, making it the most suitable for the design application.

As a result, Roskam's GD methodology was selected as the primary framework for mass properties analysis. Table 30 documented the specific equations used, along with references and indications where measured or CAD-derived values had been employed in place of empirical estimates.

Several subsystems—such as propulsion, controls, avionics, environmental systems, and electrical architecture—had individualized weights based on selected components. These values were determined using a combination of Roskam-derived approximations and reported weights from comparable real-world platforms.

Direct weight data were available and used for key elements including the engine, internal fuel, and ordnance (two AIM-120 missiles). Portions of the landing gear, including the tire assembly, also incorporated reported weights where available.

Advanced modeling capabilities in NX had facilitated direct extraction of component weights through the Mass Properties tool, enabled by the assignment of accurate material densities. This allowed for improved accuracy in key systems such as landing gear, propulsion subsystems, and structural elements, reducing reliance on purely analytical estimates.

Component center of gravity locations were measured in inches from the aircraft datum using the NX CAD model's geometry. The percent mean aerodynamic chord (%MAC) for each component was calculated by expressing its CG location relative to the aircraft's reference wing MAC. These values support later analyses including CG buildup, static margin evaluation, and loading condition studies.

Table 30 Component Weight and Center of Gravity Breakdown

No.	Component	Source	Weight (lb)	CG (in from datum)	%MAC
1	Wing	5.9 & CAD	1,832.68	327.49	48.39
2	Horizontal Tail (Htail)	5.17 & CAD	394.27	492.01	74.08
3	Vertical Tail (Vtail)	5.18 & CAD	209.31	465.82	70.31
4	Fuselage	5.26	3,379.99	303.31	27.09
5	Landing Gear	CAD & Reported	1,800.00	350.64	68.80
6	Engine	Reported	3,940.00	517.95	108.13
7	Air Induction	6.9	824.67	286.78	12.52
8	Fuel System	6.20	649.02	295.89	20.54
9	Propulsion System	6.22	63.70	100.00	-152.10
10	Flight Control System	7.10	928.76	90.00	-160.91
11	Hydraulic/Pneumatic System	7.2	322.00	100.00	-152.10
12	Electrical System	7.20	387.70	180.00	-81.59
13	Instrumentation/Avionics/Electronics	7.25 & Reported	594.42	90.00	-160.91
14	AC/Pressurization/Anti-De-Icing	7.33	137.82	170.00	-90.41
15	Ordnance	Reported	680.00	310.40	-54.80
16	Paint	7.51	100.00	339.67	59.13
17	Fuel	Reported	14,875.00	302.26	26.16
Operating Empty Weight (OEW)			**15,570**	**341.8**	**61.02**
Maximum Zero Fuel Weight (MZFW)			**16,240**	**336.3**	**56.17**
Maximum Takeoff Weight (MTOW)			**31,120**	**320.1**	**41.83**

B. Center of Gravity

The Operational CG Envelope diagram illustrated by Fig. 53 shows how the aircraft's center of gravity shifts during ground-based loading of fuel and ordnance, starting from the operating empty weight (OEW). The extreme forward and aft CG limits, marked at 40.06% MAC and 62.14% MAC respectively, define the allowable operational boundaries to maintain longitudinal stability throughout all loading conditions. The plotted forward and aft loading paths represent two bounding sequences for mass addition. The forward loading path follows the order: OEW, tank one, ordnance, tank two, tank three, tank four, tank six, and finally tank five. The aft loading path begins at OEW and loads components in reverse order: tank five, tank six, tank four, tank three, tank two, ordnance, and tank one. These cases capture the range of possible CG movement during typical ground loadout operations.

Throughout the loading process, the center of gravity remains within the defined operational envelope. Additionally, the main landing gear CG is located aft of the aft CG limit, providing a stable ground stance and ensuring there is no

risk of tipping or nose-over during the loading sequence. This representation is essential for verifying safe and balanced load integration procedures prior to flight.

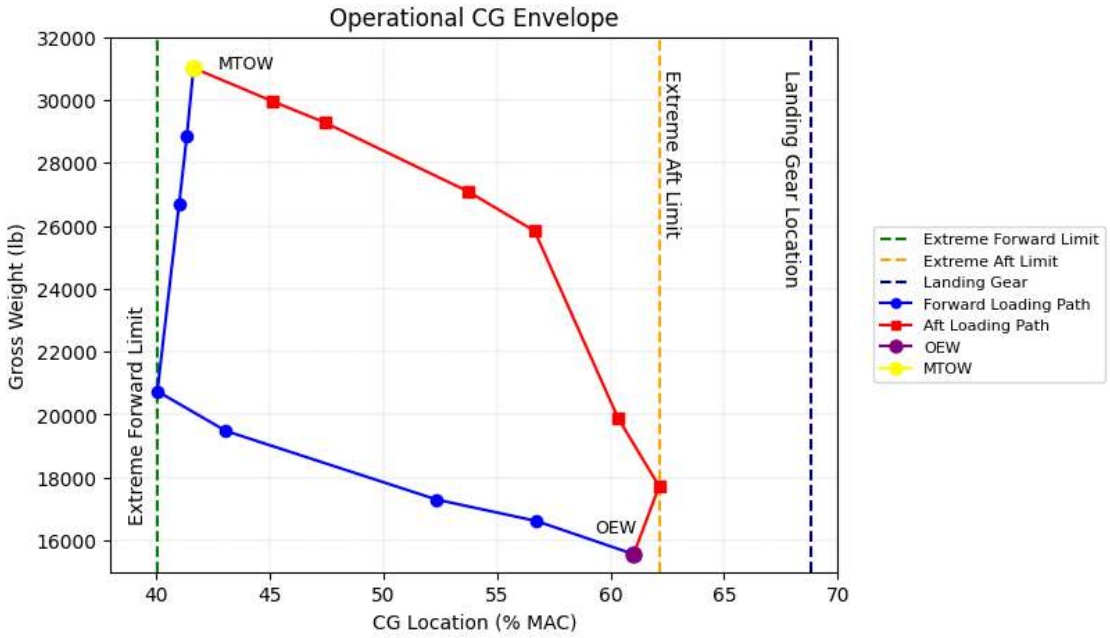

Fig. 53 Operational CG envelope.

C. Center of Gravity: Mission Segments

Once the aircraft is fueled, loaded, and begins executing any of the three defined mission profiles, the center of gravity (CG) undergoes significant shifts across the mission timeline. These changes are critical to understanding aircraft handling and stability, as they directly impact control characteristics and trim requirements.

1. Mission One: Defense Counter-Air Patrol

Mission one involves prolonged loitering, combat air patrol, and multiple high-speed maneuvers. The aircraft begins with a CG at 42.27% MAC and experiences a progressive aft shift as fuel is consumed and ordnance is expended. By the reserve phase, the CG reaches 61.02% MAC, as shown in Table 31. The most dramatic changes occur after the 4-hour loiter segment and throughout combat and dash phases, driven by fuel depletion and missile firing. Figure 54 illustrates the CG trajectory across the mission, highlighting the aircraft's capacity to remain within stability limits even as the CG shifts nearly 19% MAC aft.

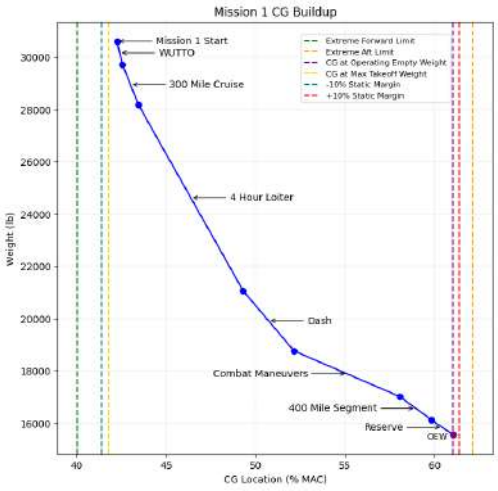

Fig. 54 Center of gravity buildup for mission one.

Table 31 Mission One Weight and CG Buildup

Segment	Weight (lb)	CG (in)	CG (%MAC)
Start	30,600	320.46	42.27
WUTTO	29,700	320.80	42.56
300 Mile Cruise	28,150	321.83	43.47
Four Hour Loiter	21,050	328.53	49.31
Dash	18,750	331.81	52.15
Combat Maneuvers	17,000	338.56	58.07
400 Mile Segment	16,100	340.59	59.84
Reserve	15,550	341.95	61.02

2. Mission Two: Point Defense Intercept

This mission emphasizes rapid climb and high-speed dash segments with a more compact flight profile. The CG starts at 47.43% MAC and transitions to 61.02% MAC by the reserve phase, as detailed in Table 32. Unlike mission one, the CG movement here is more concentrated into the mid-to-late phases of the flight. Notably, the CG change of approximately 13.6% MAC primarily results from post-engagement fuel consumption and the effects of weapon release. Figure 55 captures the relatively direct CG shift pattern and the efficient control of stability margins throughout high-speed operations.

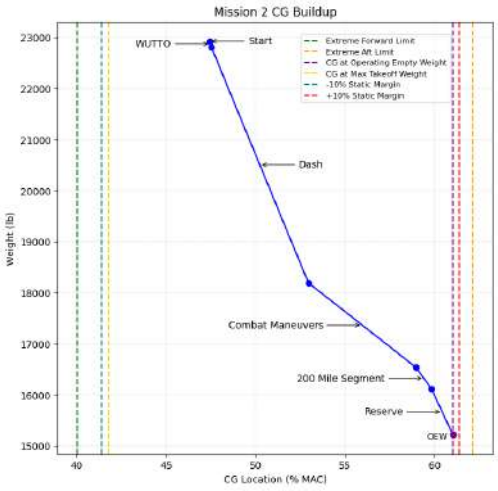

Fig. 55 Center of gravity buildup for mission two.

Table 32 Mission Two Weight and CG Buildup

Segment	Weight (lb)	CG (in)	CG (%MAC)
Start	22,900	326.40	47.43
WUTTO	22,800	326.52	47.53
Dash	18,200	333.94	52.96
Combat Maneuvers	16,550	340.44	58.97
200 Mile Segment	16,100	340.59	59.84
Reserve	15,250	341.95	61.02

3. Mission Three: Intercept and Escort

Mission three begins with the CG at 42.20% MAC and ends at 56.17% MAC by the reserve phase, as seen in Table 33. While this mission exhibits a moderate total CG shift of 14% MAC, the distribution is smoother across segments such as dash, escort, and return. The escort phase, flown at minimum practical airspeed for an extended duration, significantly contributes to aft movement due to sustained fuel draw from forward tanks. Figure 56 shows a gradual CG progression, with stability preserved by balanced tank usage and planned ordnance deployment.

In all three missions, the calculated CG paths serve as key indicators of design robustness under variable loading and fuel burn. Graphical depictions in Figs. 54–56 visualize the CG evolution, confirming that mission performance remains within the aircraft's center of gravity envelope and allowable static margin bounds.

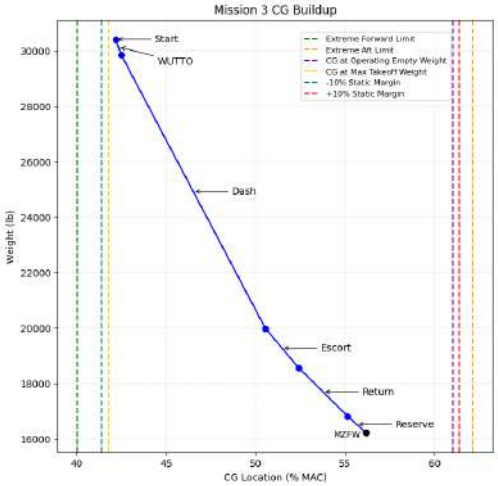

Fig. 56 Center of gravity buildup for mission three.

Table 33 Mission Three Weight and CG Buildup

Segment	Weight (lb)	CG (in)	CG (%MAC)
Start	30,400	320.13	42.20
WUTTO	29,850	320.47	42.50
Dash	20,000	329.30	50.55
Escort	18,550	331.25	52.42
Return	16,850	334.13	55.13
Reserve	16,250	335.28	56.17

D. Component CG Influence and Drivers

To better understand which subsystems most significantly affect the aircraft's center of gravity, a visual mapping of component CG locations and relative weight contribution was developed, as shown in Fig. 57. Each circle represents the CG location of a specific aircraft subsystem, plotted relative to the airframe. The size of each circle corresponds to the component's weight as a percentage of the total aircraft mass, providing a dual representation of both CG location and its influence on overall balance.

As seen in the figure, the most prominent contributor to CG placement is the internal fuel system, shown as the largest circle. Its central location and substantial weight make it the dominant driver of both the aircraft's overall CG and its variability during different mission segments. Other significant components include the engine, avionics, and landing gear, but none match the fuel system in impact.

This CG mapping highlights the importance of optimizing the fuel tank location to ensure stability throughout

mission execution. The visual emphasis on the fuel system supports the rationale for conducting a focused trade study on fuel placement, discussed in the following section.

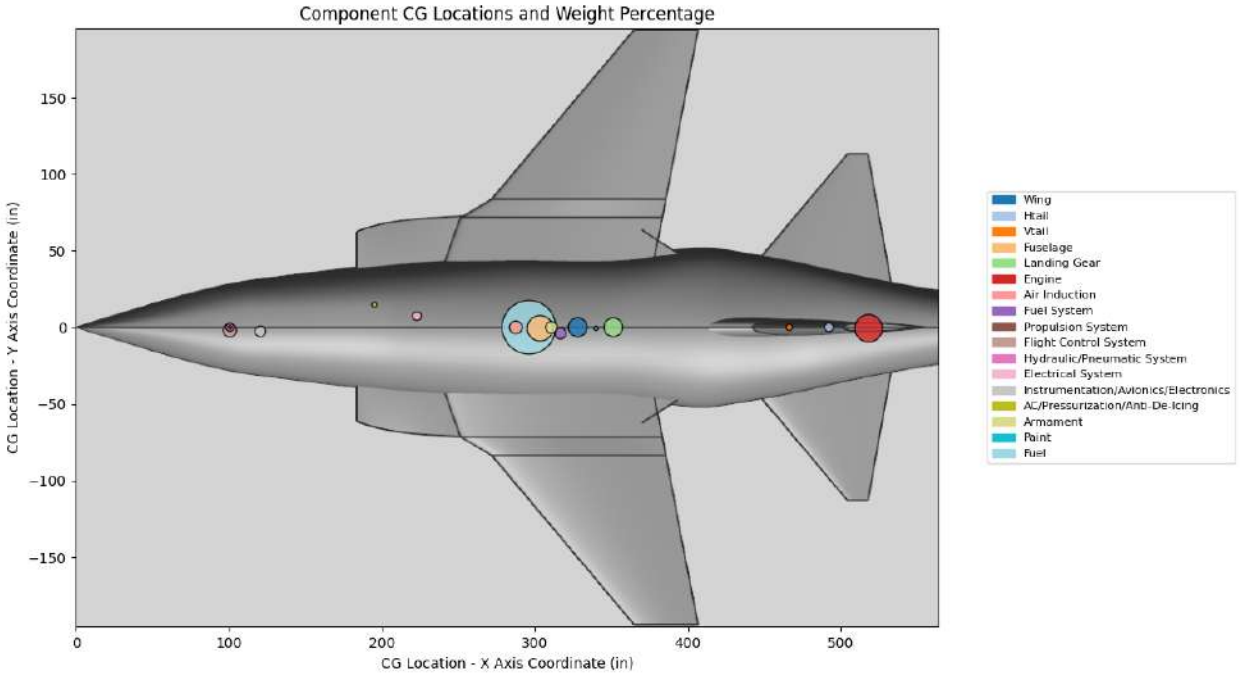

Fig. 57 Component CG locations and relative weight contribution.

E. Trade Study: Fuel Placement

A trade study was conducted to evaluate the impact of fuselage fuel tank placement on overall aircraft stability and static margin compliance. In an earlier configuration, the fuel tank CG was located at 285.6 in from the nose, placing it ahead of the Leading Edge of the Mean Aerodynamic Chord (LEMAC), which is at 272.6 in. This configuration resulted in a negative CG expressed as a percentage of MAC, leading to poor static margin and noncompliance with aircraft stability requirements.

The current configuration relocated the fuel CG aft to 302.26 in, which corresponds to 26.16% MAC, as reported in Table 30. This new location significantly improved the aircraft's static margin and placed the CG within a more favorable range for both cruise and landing operations.

During an intermediate configuration stage, the CG path across mission segments resulted in a static margin range between -3% and +17%. Although better than the initial design, this range still posed concerns for longitudinal stability, particularly during aft CG conditions. To resolve this, the fuel tank configuration was revised again—retaining the same fuel volume but shifting the tank CG an additional six inches aft. This refinement aligned the full mission CG path with the ±10% static margin envelope required by the Request for Proposal (RFP), ensuring stability throughout all mission segments without compromising capacity or structural layout.

12. Landing Gear, MW

The chosen requirement for the landing gear was to sustain a 3.75 g landing at a 15 deg angle relative to the runway on only one main gear. This case was chosen to as a worst-case scenario for an aircraft landing. The gear is configured for a load distribution of 78-22. The final design of the landing gear accounts for a tipback angle of 15 deg and an overturn angle of 62 deg, shown in Fig. 58, which meet design requirements of a specified in Raymer [5]. At the required takeoff angle of attack of seven deg, the Lobo has a ground clearance of two ft.

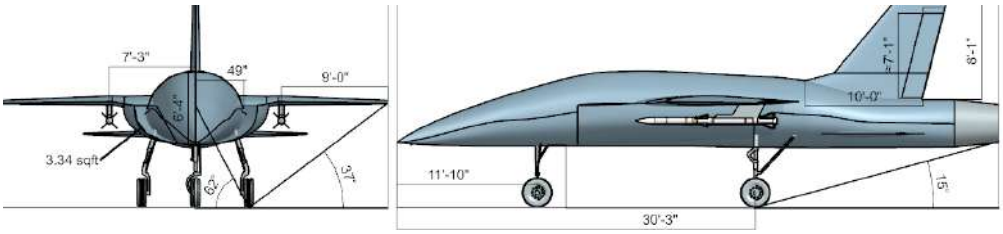

Fig. 58 Front and left view of the Lobo with tipback and overturn angles labeled.

A. Structural Design

To reduce weight while effectively transferring loads from the landing gear to the structure, a titanium housing was used. The gear connects to housings through a rotational pivot to allow the gear to retract. Linkages are connected to the aft side of the gear to provide lateral support and prevent collapse during braking. At full extension, the linkages are secured in place using down locks placed at the central rotation joint, similar to the F-16. Figure 59 depicts the nose gear in its extended position. Figure 60 shows the left main gear in the extended position.

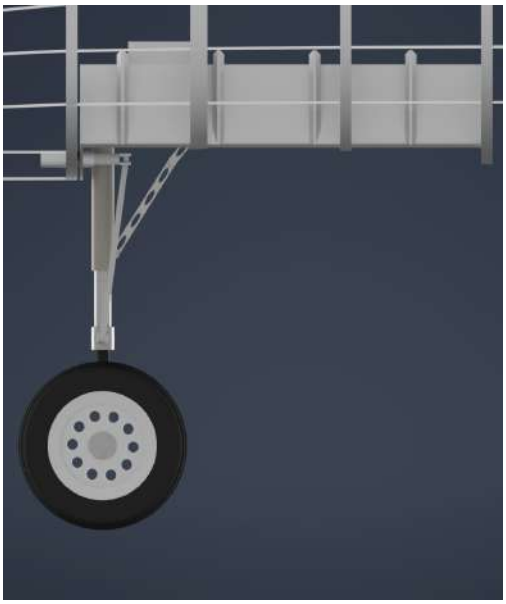

Fig. 59 Image of the nose landing gear.

Fig. 60 Image of the main landing gear.

B. Oleo System

To reduce size and weight while providing adequate shock absorption for landing, an oleo system was chosen for the nose and main gear. Using empirical equations found in Raymer alongside Euler beam bending and buckling calculations, a four inch diameter oleo was used for the nose and main gear. The inner piston of this system was sized at three inches and has a stroke length of ten inches. To meet the 40,000 lb load requirement in hard landings, the oleo was designed to bottom out at 8,000 psi, which results in a bottoming load of 56,547. This provides a safety factor of 1.41 for the expected maximum load and a safety factor of 1.21 for the maximum bottoming load of the tire. As the hard landing is assumed to occur at 13 ft/s, the oleo will absorb 47 kJ of kinetic energy, which will result in a temperature rise of approximately $2.8^{o}F$, well below the ignition temperature of the hydraulic oil contained within the cylinder.

C. Wheel Selection

Due to speed requirements and runway classification restrictions, the Goodyear 753M series was chosen for all three landing gear. As the 753M25G3 has a larger rated and maximum load than the aircraft's expected loads, it was chosen to be used as the tire for the main gear. To reduce the complexity of maintenance as well as provide adequate flexibility in braking performance and alternative use cases, the 753M25G3 was also chosen to be used as the tire for the nose gear. Specifications for this tire are provided by Goodyear Aviation and can be found in Table 34 [32]. For runways with lower pavement classifications, the tires can be deflated to 200 psi.

Table 34 Table of Tire Specifications

Property	Manufacturer-Specified Value
Diameter	29.96 in
Width	9.33 in
Maximum Rated Load	15,620 lb
Maximum Bottoming Load	46,900
Maximum Braking Load	23,430
Rated Inflation	232 psi
Rated Speed	257 MPH

D. Retraction

The retraction mechanism of the Lobo is designed to be similar to the F-16. A hydraulic piston is placed within the landing gear housing and connects to a pivot located near the top of the oleo strut. This system consists of a three inch diameter hydraulic cylinder with a two inch diameter piston. It operates at 5,000 psi to integrate with the rest of the hydraulic systems. Pneumatic single-acting pistons are used to engage an up-lock system to ensure that the gear remains stowed in high-g maneuvers. Due to space considerations below the forward fuel tank, the nose gear is required to rotate

90 deg. To accomplish this, the steering hydraulic piston is designed to bottom-out at an extension of seven inches. As the steering linkage is connected off-axis to the lower strut assembly and the steering linkage has a fixed length, the extension limit of the steering piston forces the wheel to rotate 90 deg to its retracted position. This sequence can be seen in Figs. 61, 62, 63, and 64, which show the nose gear in the process of retracting. Figure 62 was taken at the point where the nose gear rotated to 90 deg. As no rotation is required for the retraction of the main gear, a torque link is placed between the upper and lower segments of the oleo strut to prevent rotation during landings. All gear are designed to free-fall into the extended position in the event of a failure of the hydraulics system.

Fig. 61 Image of the landing gear extended.

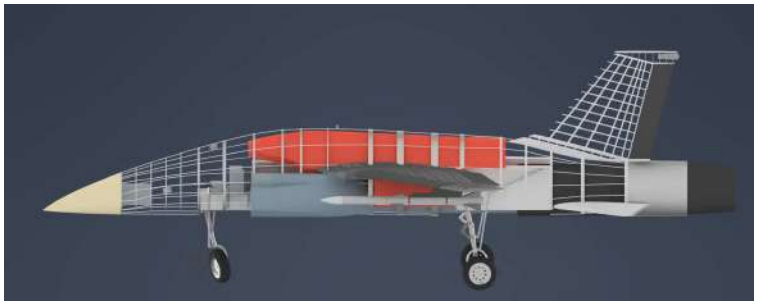

Fig. 62 Image of the landing gear during retraction at point of nose gear rotation.

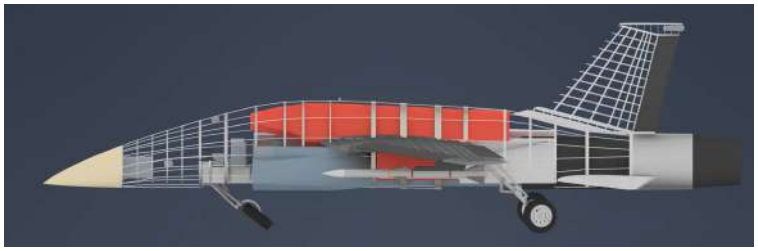

Fig. 63 Image of the landing gear while retracting.

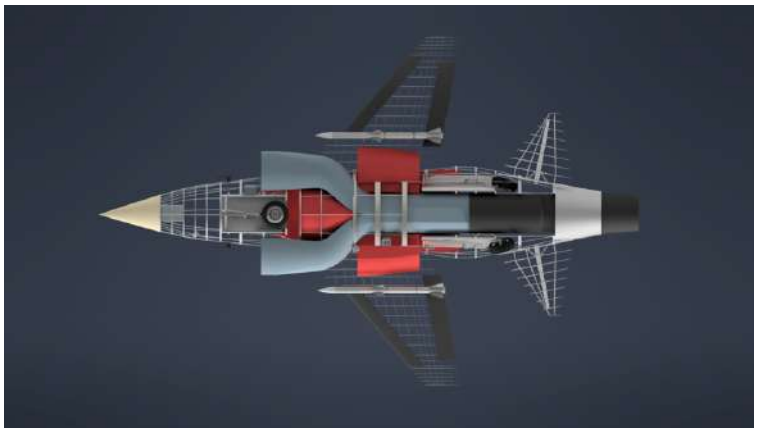

Fig. 64 Image of the landing gear retracted within the fuselage.

E. Steering

Steering of the nose gear is handled by a hydraulic piston connected by a fixed-length linkage to the oleo strut. Linear extension of the hydraulic piston translates to rotational movement of the nose gear due to the off-axis connection of the linkage. This system can be seen in Fig. 65, which depicts the nose gear in a full left turn deflection. This system can achieve a maximum turning deflection of 62.59 deg, allowing the Lobo to have a minimum turning radius of ten ft. In later iterations of the design, shock absorption considerations will need to be implemented through a linkage system.

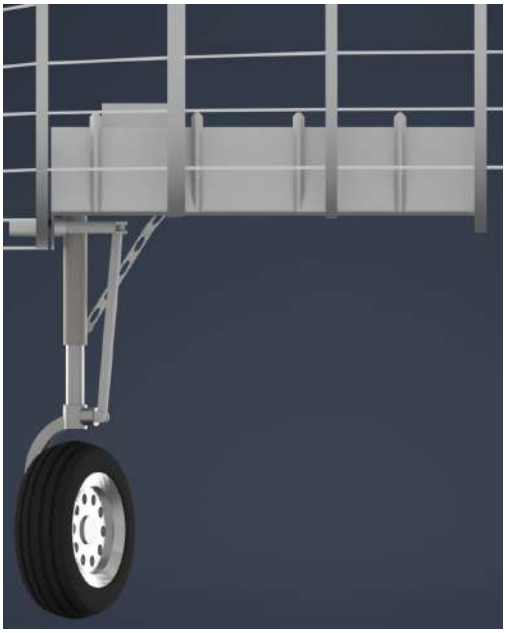

Fig. 65 Image of the nose gear with maximum steering deflection.

13. Systems, DM

A. Flight Controls

Lobo will utilize a remote fly-by-wire system, which provides benefits such as weight reduction and improved handling characteristics. Inputs given by the pilot and sensor operator will be communicated to the aircraft and translated into control surface movements for roll, pitch, and yaw. The aircraft will also utilize leading- and trailing-edge flaps for additional lift at lower speeds. During landing, Lobo will use hydraulic braking and spoilers to decrease speed.

Lobo's flight control system will also utilize a Vehicle Management System (VMS) to perform continuous adjustments to collective and differential control surfaces throughout its flight. This will not only enhance the stability of the aircraft across flight regimes, but will also improve its fuel efficiency. As part of the VMS, an Integrated Flight and Propulsion Control (IFPC) will be used to precisely regulate fuel flow to the engine, which is fitted with quadruplex sensors and actuators for added redundancy. Additionally, a VMS will enable Lobo to more precisely manage internal cooling temperatures, as shifts in flight regimes and changing inlet conditions can make bleed air temperatures more difficult to regulate.

B. Engine Controls

Lobo will utilize a direct throttle power input remotely communicated by the pilot at the ground station to control fuel flow into the engine. However, the relationship between the thrust generated and the fuel supplied to the engine is complicated by the changes in atmospheric variables at different flight regimes. Changes in engine operating conditions caused by fluctuating air density mean that the pilot would have to continually adjust throttle controls to maintain optimal flight conditions.

Lobo will use a Full Authority Digital Engine Control (FADEC) system, which leverages various atmospheric inputs to provide precise fuel flow corrections to maintain an optimal flight envelope. Examples of these atmospheric inputs include airspeed and altitude, total temperature, engine speed, engine temperature, nozzle position, and current fuel flow. Inputs such as altitude and total temperature are calculated through measurement probes already located throughout the aircraft, while parameters such as engine speed and engine temperature are measured through speed probes and thermocouples located within the engine itself.

The schematic in Fig. 66 displays a simplified fuel flow mapping from the fuel tanks to the engine. Fuel is fed from the tanks through a low-pressure fuel pump, which can be disengaged through an engine shut-off switch. The fuel is then used as a cooling medium for oil in a heat exchanger before being filtered. This oil is used in many of the aircraft's systems, such as in the engine and environmental control systems.

The fuel undergoes a dual-stage filtration method, split between a fuel strainer and a fuel filter. The fuel strainer is much coarser and is first used to filter large particles from the liquid that could have been mixed with the fuel in the tanks. The fuel is then fed to a fuel filter, which uses finer grates to remove foreign particles that are small enough to

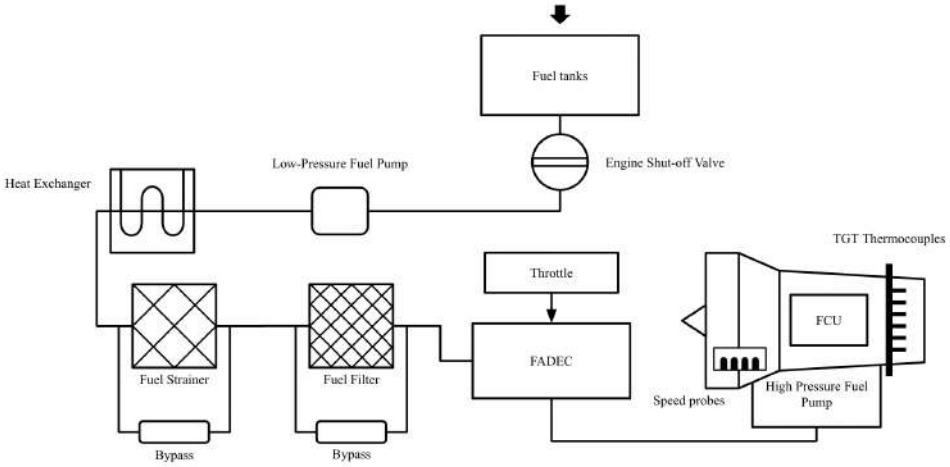

Fig. 66 Engine control schematic for Lobo propulsion system.

pass through the fuel strainer. These devices collect foreign objects rather than expel them, and must thus be changed every 100 flight hours in accordance with 14 CFR §43, App. A.

For redundancy, two fuel bypass switches are added across the fuel strainer and fuel filter. This ensures that fuel can flow, even in the case that the filtration system is clogged. The bypass filters are closed by default and only open when additional fuel flow is needed.

C. Fuel System

Lobo's fuel volume is split between five fuel tanks positioned above the wing. This design was chosen because it provides sufficient control over the location of the CG. Additionally, this design minimizes the risk of cavitation during flight, which occurs when the change in flight conditions makes fuel more susceptible to vaporization. This can cause many complications during flight — such as engine flameout — and can be avoided through the use of fuel booster pumps. The aspects of the fuel system are designed to satisfy MIL 516C part 8.3.4.

Manufacturer standards require a fuel feed pressure of at least five psi above true vapor pressure at all times [33]. In order to achieve this, Lobo's fuel tanks will contain fuel accumulators, which will allow the aircraft to more accurately regulate the pressure of fluid pumped to the engine.

Fuel from Lobo's tanks can be cross-fed between fuel accumulators, providing an additional layer of redundancy in the case of pump failure. Additionally, tanks are interconnected between each other through bidirectional transfer valves, allowing fuel to be routed between them. In the case of a fuel pump failure, fuel tanks are arranged to allow for fuel to fall to lower tanks in a gravity-driven system. All fuel tanks are self-sealing, and 11 millimeters of space was included between fuel tanks and the fuselage in order to account for this feature [34].

Lobo's fuel system layout is displayed in Fig. 67. Due to Lobo's demanding combat characteristics, fuel will be

pumped from the front of the tanks. This ensures the weight will shift forward as the mission progresses, ultimately improving aircraft stability and control. With regard to refueling, Non-Return Valves (NRVs) will route incoming fuel to Tank one, from which it will drain to Tanks two, three, and four. Fuel pumps can expedite this process if necessary.

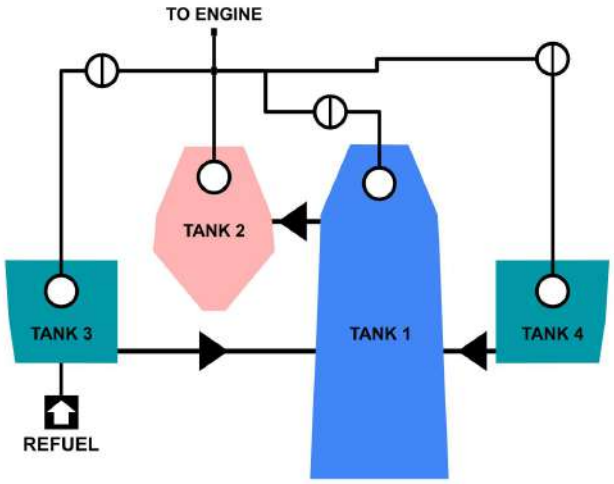

Fig. 67 Fuel tank schematic.

Each tank is also fitted with a fuel vent valve, which relieves pressure and vacuum in the tank during refueling. This is a crucial component to prevent explosions and leaks.

Lobo will not provide the capability for fuel jettison. Due to the fact that the aircraft's MTOW and MLDW are equivalent — as well as the cost constraint given by the RFP — there is little justification for this system to be implemented.

D. Hydraulic Systems

Hydraulics are used by Lobo to actuate many of its control surfaces, implement backup safety mechanisms, and activate additional military capabilities. The hydraulic system is split into two primary systems — A and B — each supported by a single hydraulic reservoir. A third standby system, also supported by its own reservoir, can be used in the case of hydraulic failure. Fluid in the B system can be fed to the A system via a Pressure Transfer Unit (PTU) valve, which allows pressure to be transferred from one system to the other without mixing fluid. This is used specifically in case of hydraulic failure, where pressure may be lost in the A system. This verifies safe operation in case of a failure in accordance with MIL 516C part 8.1.1.

Hydraulic fluid is pumped in and out of each reservoir using Engine Driven Pumps (EDP). These pumps will be mounted in the engine auxiliary gearbox to provide easy access for maintenance personnel; they use power generated from the engine to feed hydraulic fluid throughout the system. In the case of EDP failure, Alternating Current Motor Pumps (ACMP) can be used to perform the same function. ACMPs are continuously rated and capable of maintaining

the required system pressure of 5,000 psi.

A schematic of Lobo's hydraulic system is shown in Fig. 68. Fluid for the actuation is split between the three systems, with A routes being expressed in red, B routes expressed in green, and C routes expressed in blue. Filters are located in each system to remove foreign debris from the hydraulic fluid. It is important to note that while the schematic maps general hydraulic movement from point to point, when implemented, each route will have an outbound and an inbound line.

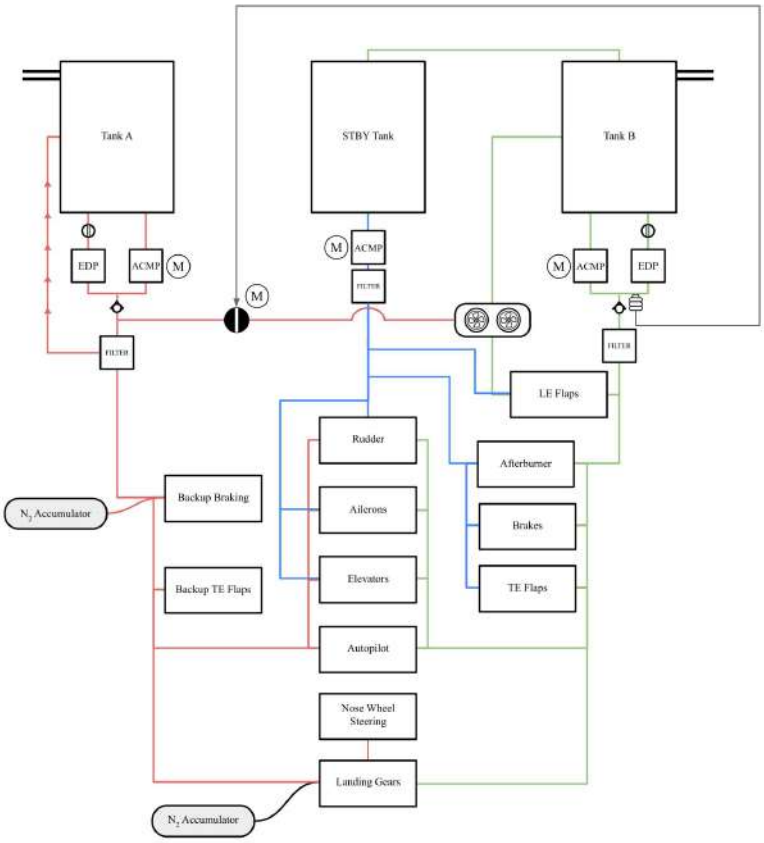

Fig. 68 Simplified schematic for Lobo hydraulic systems.

The hydraulic system is categorized into three groups: Primary Flight Controls, Secondary Flight Controls, and Utilities. Primary Flight Controls refer to systems that are required for basic aircraft maneuverability, such as elevators, rudders, and ailerons. Secondary Flight Controls refer to systems that enhance flight characteristics but are not necessary for survivability. These controls include leading-edge flaps, trailing-edge flaps, spoilers, and stabilizer trim. Lastly, Utilities refer to systems that are not directly necessary for flight. Examples of these systems include afterburner, landing gear, brakes, and nose-wheel steering.

When planning the hydraulic system, these systems are prioritized and split between the A and B reservoirs such that the overall hydraulic load is similar. The STBY reservoir is fed to the most essential systems to ensure redundancy

in the case of hydraulic failure. In the case that a system is not backed up by the STBY reservoir, a backup hydraulic actuator is implemented and linked to the alternate reservoir.

Check valves are implemented throughout the hydraulic system in areas where a loss in pressure could substantially affect the operation of the system. These check valves are placed on all unidirectional hydraulic feeder and return lines and function as an additional measure to prevent backflow in the system.

N_2 accumulators are placed strategically throughout the hydraulic system to provide an additional layer of redundancy in the case of hydraulic failure. These devices collect pressure during standard system operation and can be used to introduce additional pressure into the system to ease the burden on the EDP, ACMPs, or RAT. Lobo uses an accumulator on its A-reservoir system to maintain stability during the operation of the PTU. Its placement also enables it to be used to assist the EDP during the initial startup of the ACMPs.

With additional pressure sources being introduced into the system, it occasionally occurs that the hydraulic system is overwhelmed with pressure. This can be dangerous, as unregulated high pressure can cause damage to both internal and external systems. To mitigate this, pressure relief valves are placed at the top of the A and B reservoirs to vent fluid. This ensures a proper pressure rating is maintained throughout the system at all times.

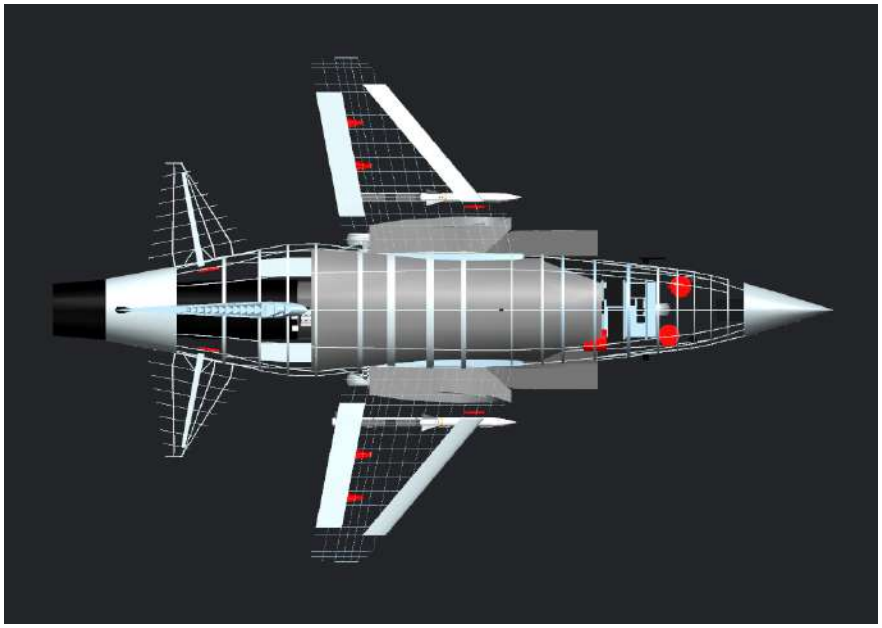

Fig. 69 Physical arrangement of hydraulic actuators.

Figure 69 shows Lobo's physical hydraulic system placement. The aircraft uses two hydrostatic actuators for trailing edge flaps, one for leading edge flaps, one for each landing gear component, and one for each of the differential horizontal stabilizers. The rudder also uses two hydraulic actuators, which are not pictured.

1. High-g Considerations

Lobo's hydraulic system is designed to withstand high-g maneuvers through various flight regimes. The hydraulic fluid used, MIL-PRF-87257, is a Polyalphaolefin-based fluid approved by the Air Force in 1990 [35]. The fluid's fire-resistant nature mitigates the risk of hydraulic fluid fires, also keeping ground personnel safe. Additionally, its high performance under extreme temperatures and pressures ensures it is reliable throughout all parts of Lobo's flight.

The size and positioning of hydrostatic actuators were also selected with high-g maneuvers in mind. Along with actuators being designed to minimize stroke length, the orientation of these devices — specifically, being placed at a 90-degree angle — minimizes strain during stages of flight where loads are high.

2. Hydraulic Pump and Tube Sizing

The three hydraulic reservoirs, located in the front section of the aircraft, are sized to produce three times the volume contained in the hydraulic tubes. The hose assembly is comprised of MIL-DTL-8790, which can withstand temperatures from -65 to +275 degrees Fahrenheit. The hoop stress and thickness formulas were used to size the tubes to have a total diameter of 1.66 inches.

3. Ram Air Turbine

In the case that additional power is needed to maintain hydraulic pressure, a Ram Air Turbine (RAT) is installed. Lobo's RAT will be located within the nose wheel well for all stages of flight and will extend when additional power is needed. Although the RAT and nose landing gears will not be able to enter transitional stages at the same time, they can both be extended or retracted simultaneously.

Based on the 50 kW electricity requirement for crucial avionics and systems, Equation 1 was used to determine the required total blade area:

$$P_e = \frac{1}{2}\rho V^3 A \kappa_p \eta_{tot} \tag{1}$$

where P_e is the required electrical power, ρ is the air density, A is the blade area, κ_p is the power coefficient, and η_{tot} is the total efficiency. From the RFP and electrical schematics, P_e is known to be 50 kW. The values for η_{tot} and κ_p were estimated to be 0.8 and 0.3, respectively, based on real-world empirical data. The atmospheric variables at an altitude of 35,000 ft and airspeed of 350 KTAS were the design drivers for the RAT.

Lobo uses two RAT blades, sized for efficient stowage within the nose wheel well. The final dimensions are shown in Fig. 70:

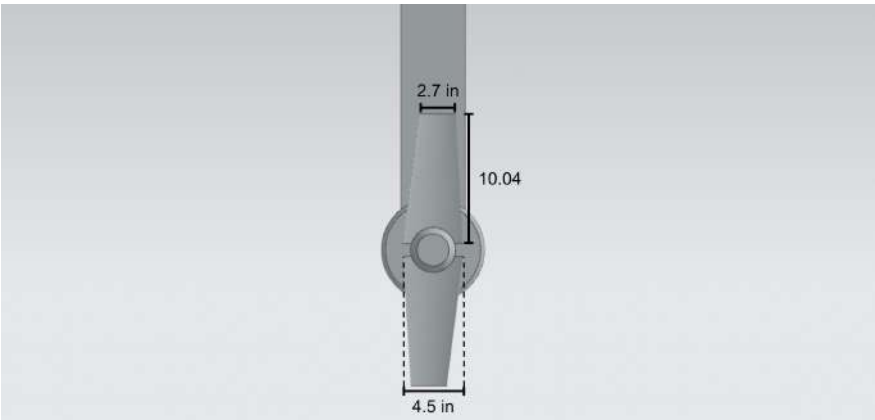

Fig. 70 Dimensions of the ram air turbine.

E. Electrical System

Lobo leverages both AC and DC power, each in different cases. The electrical system uses a series of 28VDC electrical buses that distribute DC power among primary systems and sensors. The general power system distribution diagram is shown in Fig. 71. This does not express individual power distribution among buses, but rather displays the overall battery-to-system routing.

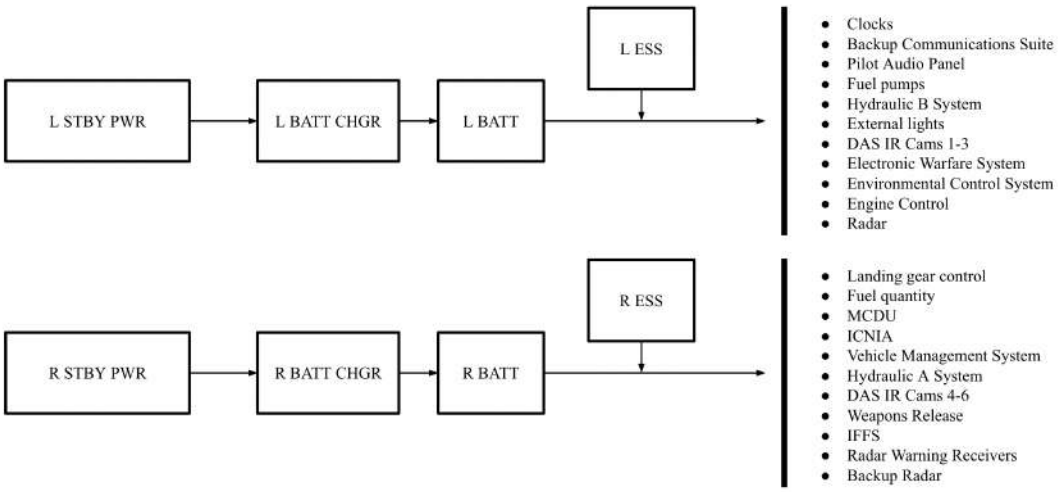

Fig. 71 Distribution of left and right electrical systems to DC power.

The generator is regulated to supply a consistent current such that voltage fluctuation tendencies are overcome. AC power is also generated through an Integrated Drive Generator (IDG), which generates AC power from engine movement. This current is regulated to output three sine waves at a constant frequency, each positioned at a 120 phase offset from the previous wave. This enables voltages to be easily fluctuated between high voltages for transmission and

low voltages for distribution, providing increased efficiency to the system overall. The aircraft's high-level electrical system schematic is shown in Fig. 72. Individual connections from the buses to the electrical systems are not displayed, however, distribution between the power systems and the buses is shown. The blue connections represent AC power, and the red connections represent DC power. The black connections represent systems without initial power.

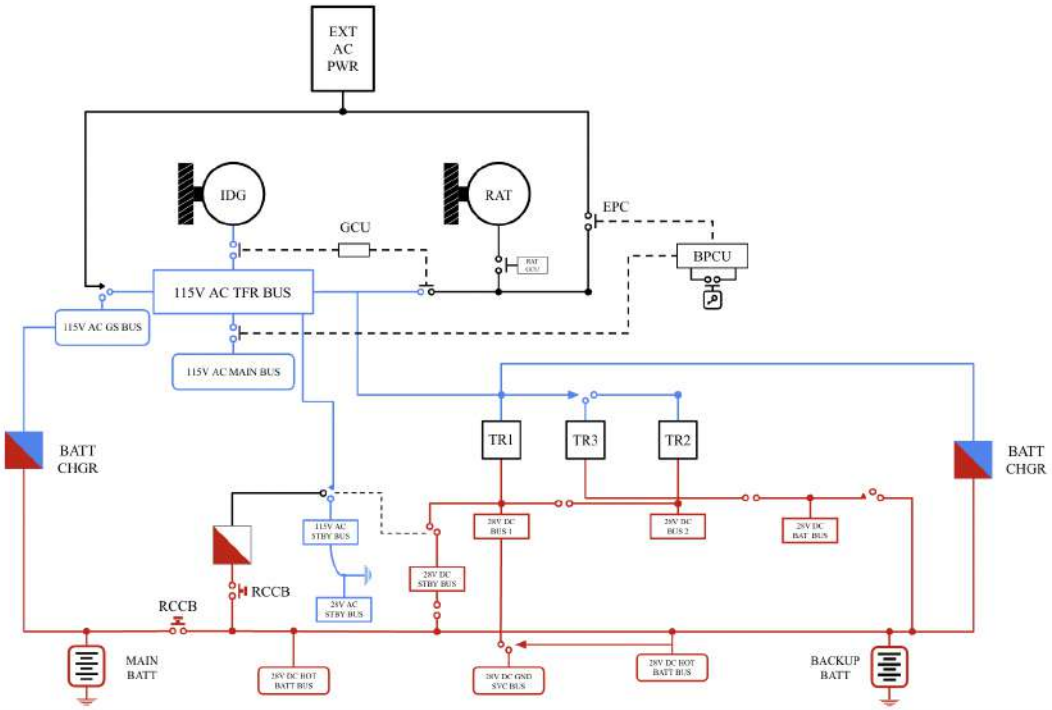

Fig. 72 High-level schematic of Lobo electrical system.

Power is interfaced from AC to DC through three Transformer Rectifiers (TR), which output constant DC voltage from sinusoidal AC inputs. This electricity is then fed to the DC power buses, which distribute electricity to individual systems and recharge the battery.

The Bus Power Control Unit (BPCU) is the electrical system's primary management device. This device controls the following systems:

- **External Power, typically by Ground Power Unit (GPU)** - Externally supplies auxiliary power to the aircraft's electrical systems. Only used when the aircraft is on the ground and connected to airfield infrastructure.
- **Ram Air Turbine (RAT)** - Deployed during emergency situations to provide additional power to electrical and hydraulic systems. [36]

Power from the generators can be activated using the External Power Contactor (EPC) which, when connected, connects power from the GPU to the AC electrical system. Similarly, the system's Generator Control Units (GCU) interface power between the generators and the AC system, regulating voltage to prevent electrical faults.

The electrical system also contains Main and Backup batteries that provide power to the system. The batteries were

selected Concorde RG-380E/44, which have a 24V 42Ah power specification. This selection was driven by their ability to power the aircraft for 30 minutes in the case of an electrical failure at its maximum operational altitude, assuming a 1 kW conservative load split among backup flight controls, emergency radios, and essential sensors. This calculation also includes a 50% safety margin, satisfying MIL 516C part 12.1.1. When stored, these Lithium-ion batteries will be covered in fireproof containers to prevent any damage if the battery were to explode.

In the case of electrical failure, a standby AC electrical bus is continuously running. This standby bus can provide both AC and DC power to other buses as needed. Power overloads are prevented by two Residual-Current Circuit Breaker (RCCB) devices, which open the circuit if the current detected is too high.

The system is also equipped with two 28 VDC hot battery buses, which run continuously. These buses supply electricity to critical components such as the aircraft's lights, fuel system, anti-ice, and fire suppression systems.

1. Anti-Theft

It is worth noting that a physical key is required to activate the BPCU, which is implemented as an anti-theft measure. However, if it does occur, this measure will provide an additional layer of security to ensure no damage will occur to airport equipment or personnel. The BPCU specifically was chosen as it dictates the interface between external and AC power, and a deactivation of this prevents crucial operations from running, such as engine start.

F. Environmental Control System

Due to the nature of the aircraft's operation — specifically, being remotely controlled — pilots will be more heavily reliant on onboard sensors and electronic equipment than on traditional manned aircraft. Considering the absence of a cockpit onboard, the avionics are able to be packed more tightly. Although this allows the aircraft to be smaller, more advanced electronic components being used will result in more heat and power dissipation during flight, which is difficult to maintain [37]. Thus, a need arises for an advanced climate regulation system that is able to maintain stable internal temperatures for computer equipment and embedded sensors. This will be in accordance with MIL 516C part 12.1.2.

One cooling system that has historically been used for avionics applications is ram-air convection. This method involves positioning an intake at the front of the aircraft, which increases the air pressure through the usage of a diverging nozzle [38]. Although this cooling method was considered, compressibility effects would make temperatures difficult to regulate, as inlet temperatures could reach upwards of 350 degrees Fahrenheit during dash, per Fig. 73.

Instead, liquid cooling was selected as Lobo's avionics Environmental Control System. In this method, a coolant is circulated throughout mission-critical electronic components and to the wings to further cool embedded sensors [38]. Although the liquid cooling system allows for more precise temperature regulation, its components can be heavy depending on their coverage throughout the aircraft. Polyalphaolefin (PAO) has been selected as Lobo's coolant due to

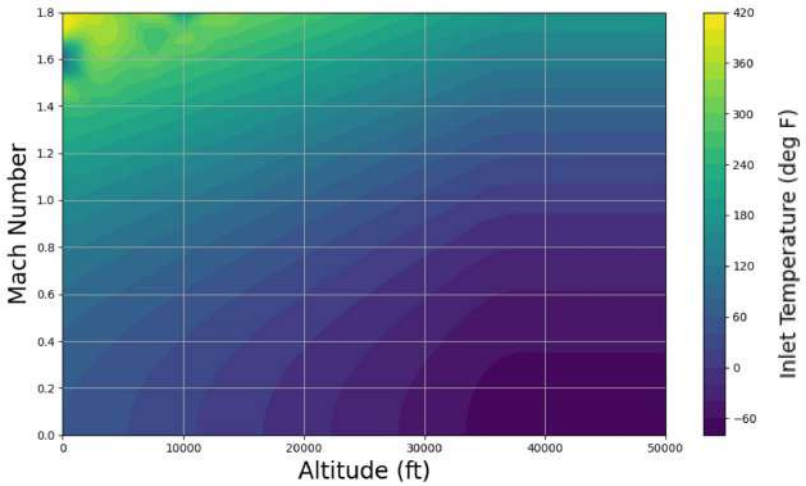

Fig. 73 Inlet temperatures at various flight regimes.

its excellent thermal conductivity and high dielectric strength, stability, and wide operating temperature range [39]. Additionally, ram air can still be used with this method to cool PAO.

Figure 74 shows the simplified schematic for the aircraft's self-contained liquid cooling system. PAO is pumped at a constant rate to a series of cold plates that directly contact avionics equipment. Lobo will be fitted with 30 cold plates, interfacing between integral avionics components. This allows multiple processors to share a single cold plate, providing the benefit of precise temperature regulation while reducing the overall system weight. After cooling, the PAO is sent through a diverter node, which redirects the warm fluid to the heat exchanger while recirculating the cold fluid to the pump.

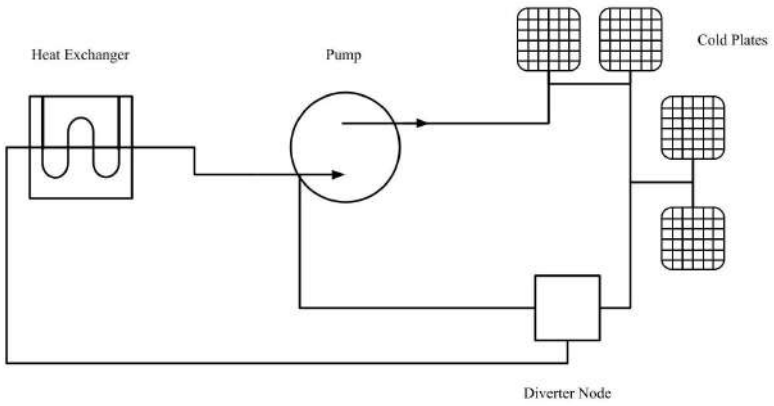

Fig. 74 Liquid cooling system for avionics environmental control.

Liquid cooling is used in more modern fighter aircraft, such as the Lockheed Martin F-22 Raptor, Lockheed Martin F-35 Lightning, and General Dynamics F-16 Fighting Falcon [40]. It is also used in commercial applications on aircraft

such as the Boeing 777 and Boeing 787.

G. Emergency Systems

1. Safety in Bad Weather

Lightning poses inherent risks to Lobo during flight, and adding preventative measures to the aircraft ensures safety both on the ground and in flight. Lobo will use an On-Board Inert Gas Generating System (OBIGGS) to provide nitrogen gas to the fuel system, ultimately reducing oxygen content in fuel vapor to below 9%. This value was chosen as it provides a safe fuel-to-air ratio throughout all stages of flight.

Additionally, static wicks are placed on Lobo's control surfaces to discharge electricity from lightning strikes. Fig 75 shows the location of these devices. Three wicks are located on the trailing edge of each wing at a seven-inch separation to minimize the distance between them and maximize coverage across the wingtips. Three wicks are also placed on the vertical stabilizer.

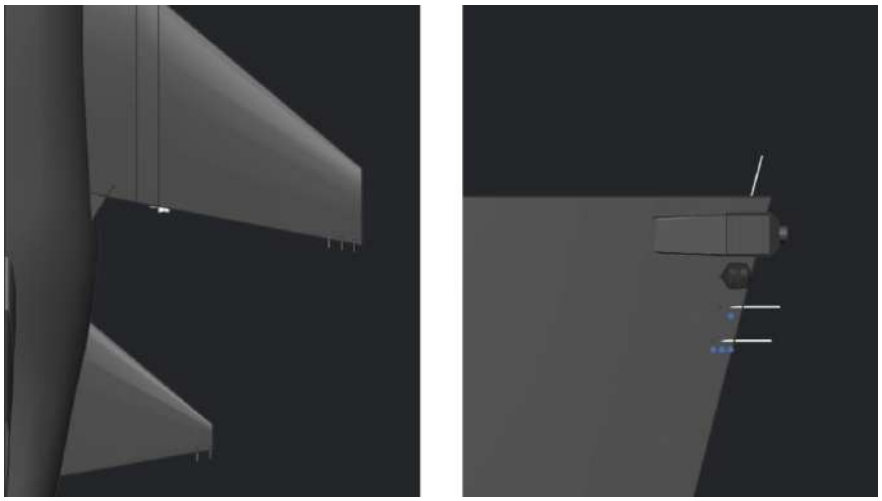

Fig. 75 Static wicks on the trailing edge of the wing and horizontal stabilizer (left) and at the top of the vertical stabilizer (right).

2. Aircraft Health and Crash Logging

Lobo will use Boeing's Aircraft Health and Trend Monitoring system to self-diagnose issues and notify the crew when maintenance is required. Although not necessary, this feature eases the burden on pilots and mechanics when completing regular aircraft checks.

Additionally, Lobo will be fitted with a crash recorder and a flight data recorder. These devices will be installed in a fireproof box, enabling them to withstand extreme crash conditions.

H. Lights

Lobo will be equipped with position, anti-collision, landing, and taxi lights to comply with FAA regulations. The layout of Lobo's light system is shown in Fig. 76. The purpose of each lighting system, as well as its location, is listed below:

- **Position Lights (Solid)** - Red light on left wingtip, green light on right wingtip, white light below engine. These lights provide information to other aircraft about orientation.
- **Anti-collision Lights (Flashing)** - Red lights on top and bottom of aircraft, white lights on wingtips. These lights illuminate aircraft wingtips for ground personnel and other aircraft to prevent collisions.
- **Landing Lights (Solid)** - White lights fore of fuselage, near radome. These lights illuminate the runway during takeoff and landing.
- **Taxi Lights (Solid)** - Front-facing lights mounted on the nose wheel joint. These lights provide additional visibility during taxiing.

Fig. 76 Location of Lobo's lights.

14. Avionics, DM

A. Navigation, Surveillance, and Targeting

1. Distributed Aperture System

Lobo will implement a Distributed Aperture System (DAS), similar to that of the AN/AAQ-37 used on the Lockheed Martin F-35 Lightning II. The DAS includes six infrared cameras to provide enhanced visual support for pilots [41]. This technology is an improvement over conventional 360-degree cameras, as it disregards the visual obstruction caused by clouds, dust, haze, and fog. Additionally, the arrangement of the DAS system enables Lobo pilots to have a spherical (4π steradian) visual range without additional input from the pilot or sensor operator.

The layout of the DAS cameras is shown in Fig. 77. Four of the six cameras are shown in the figure, while the remaining two cameras are located on the opposite side of the fuselage in the same orientation as the lower two cameras.

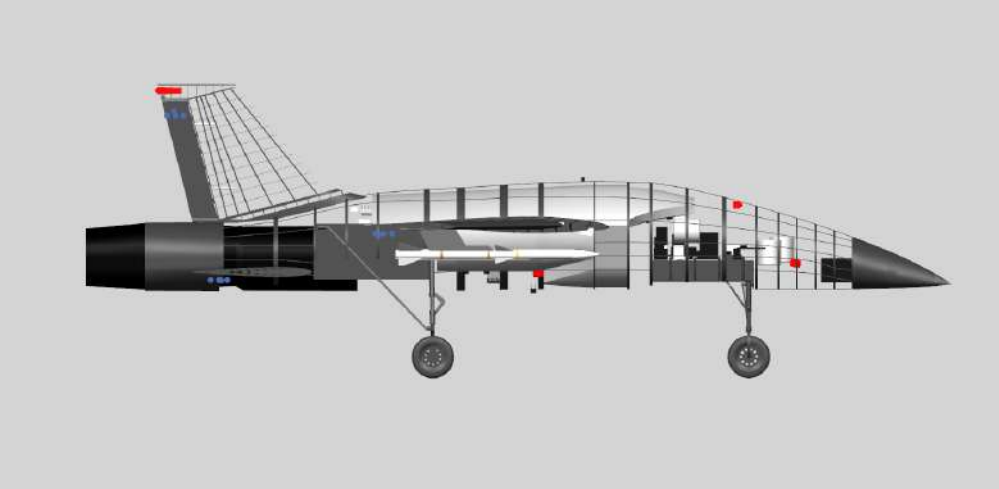

Fig. 77 Layout of Six DAS infrared cameras.

In the case of DAS failure, Lobo is equipped with an advanced navigation suite, allowing for the safe operation of the aircraft without the need for a direct video feed. This is in satisfaction of MIL 516C parts 11.1.1.5 and 11.1.2. The exact specifications of this navigation system are discussed in section 14.G.

2. Radar Warning Receivers

The aircraft is fitted with the AN/ANR-39 Radar Warning Receiver (RWR) system. This system is able to detect incoming RADAR signals and notify the pilot when the aircraft is under surveillance. This adds an additional layer of safety and situational awareness.

Lobo's RWR antennae are located on the leading and trailing edges of its wings and horizontal stabilizers. These locations were chosen as radar signals are most often deflected from them. The RWR system spans five communication bands — D through K — enabling the aircraft to simultaneously scan different frequency ranges for incoming signals.

B. Communication

1. UHF and VHF Communication

Being a remotely-controlled aircraft, Lobo must be able to communicate with its ground station controllers such that a continuous, steady stream of input is transmitted and received throughout all stages of flight. The aircraft is fitted with both Ultra-High Frequency (UHF) and Very High Frequency (VHF) radio communication bands. The UHF bands will be used mainly for short-range communication with Air-Traffic Control (ATC), while the VHF bands will be used to transmit data from the sensors to the ground station when the aircraft is within Line of Sight (LOS).

Because the aircraft is unmanned, ATC communications will be relayed from local airports to the aircraft via UHF,

then forwarded to the ground control station using VHF, and vice versa. Satellite Communication (SATCOM) will be used to transmit live flight data and control inputs between the ground station and the aircraft.

C. Ground Control Station

Lobo will be flown by two ground stations. The aircraft's proximity to the ground station is generally irrelevant to the flight profile characteristics, as communication takes place solely over a satellite VHF communication band.

The aircraft's controllers will be split into two teams: the Launch & Recovery Element (LRE) and the Mission Control Element (MCE). Although not required, the LRE ground station will likely be located within proximity of the NATO airfield from which the aircraft is based. This will allow military personnel to maintain Visual LOS during takeoff, aiding in recovery operations in the case of an emergency.

The LRE will conduct all preparatory stages of flying. This includes warm-up, taxi, takeoff, and climb. Once Lobo is at its cruise point, control is transferred to the MCE, which will carry out the mission requirements. Upon completion, control will be transferred back to the LRE, who will descend and land the aircraft. Although more complex than on a traditional UAV, this approach enables the United States to sequentially launch multiple Lobo aircraft, optimizing for a swift yet effective response to any threat.

Although the LRE and MCE will operate independently, both groups will be briefed together. This will ensure mission objectives remain clear for both teams. In the case of error in transitioning control between the teams, the MCE is equipped to land Lobo as well.

D. Ground Station

To minimize equipment and personnel training costs, Lobo will be flown using General Atomic's Block 30 Ground Station. This station is equipped with 11 HD displays and is compatible with Lobo's LOS and SATCOM data links [42]. It is already used widely among military UAV applications, namely with the General Atomics MQ-9 Reaper.

Both the LRE and MCE will be comprised of two airmen: one pilot and one sensor operator. The pilot is responsible for directly providing control inputs to the aircraft and conducting maneuvers where necessary. The sensor operator aggregates data from sensor systems to assist the pilot in completing mission objectives [43].

E. Level of Autonomy

It is important to note that although Lobo is a remotely piloted aircraft, the extent of its autonomous operations is very limited. Lobo will utilize a standard Automatic Flight Control System (AFCS), which offers an additional level of guidance during flight. However, beyond this, the aircraft will require continuous input from the pilot.

The only exception to this occurs when Lobo loses connection to the ground station. Prior to flight, LRE and MCE personnel will program Lobo to a pre-defined crash point, which will serve as a temporary home base in case the data

link is broken. This location is selected based on its proximity to the base and sparse civilization. If the connection is lost, Lobo will circle its crash point until a secure data link is reestablished. If this does not occur before Lobo depletes its fuel, the aircraft will crash at the predefined point.

It is important to note that due to ethical considerations, Lobo will not be able to deploy ordnance while flying autonomously under any circumstances.

F. RADAR Selection

Given the requirements of the RFP, an Active Electronically Scanned Array (AESA) radar will be fitted onboard [1]. AESA, considered to be a more advanced variant of Passive Electronically Scanned Array (PESA), leverages many transmit-receive modules to produce multiple beams scattered in various directions simultaneously [44]. These beams are sent at various radio frequencies, making the radar much less susceptible to enemy RF jamming than PESA. Additionally, AESA has faster scan rates and enables the aircraft to track multiple targets at once, allowing the system to be more efficient overall.

A similarity analysis was conducted to compare radars on aircraft with related mission objectives to determine the most feasible Commercial-Off-The-Shelf (COTS) RADAR device. The AN/APG-81, AN/APG-77, AN/APG-70, and AN/APG-83 SABR RADARs were compared [45]. Table 35 displays the results:

Table 35 Northrop Grumman RADAR Similarity Analysis

	AN/APG-81	AN/APG-77	AN/APG-70	AN/APG-83 SABR
Max Detection Range [nmi]	150	210	110	370
Diameter [ft]	2.30		3.00	2.30
Aircraft	F-35	F/A-22	F-16	F-16 (Upgrade), B-1
Year	2016	2005	2004	2014
T/R Modules	1000	1956	1000	1000
Air-to-Air	Y	Y	Y	Y
High-res Mapping	Y	Y		Y
Multiple Ground Target Identification	Y	Y	Y	Y
Combat Identification	Y	Y		Y
Electronic Warfare	Y	Y		Y
AMRAAM Compatible	Y	Y	Y	Y
Ultra-High Band Communications	Y	Y		Y
Cost (2020) [$M USD]		4.8-5.4	6-7	2.6

Based on these results, the AN/APG-83 SABR was selected as the Radar to be used on Lobo. This device was developed in 2014 as an upgrade to the F-16, an aircraft with similar mission objectives. Additionally, the non-discounted price of USD $2.6M makes it a cost-effective solution for the requirements outlined in the RFP. The RADAR is also compatible with the AIM-120 AMRAAM missiles, which comprise a large portion of Lobo's ordnance.

The radome is tilted upwards at an angle of 15 degrees, as this minimizes the device's cross-sectional area while having minimal effect on its performance.

G. Avionics Specifications

Lobo's avionics components were carefully selected to balance cost and performance. Government-furnished equipment was selected for use whenever possible, but certain systems that offered superior performance or capabilities at a reasonable cost were sourced commercially instead, as stock equipment did not meet mission requirements in those cases.

Avionics selections are tabulated in Tables 36 and 37.

Table 36 Integrated Communication, Navigation, and Identification Avionics

Manufacturer	Product Name	Weight (lbs)	Volume (in^3)	Cost
BAE Systems	AN/ARC-231A	15.0	6912.0 [1]	343,000 [1]
BAE Systems	RT1987 SATCOM	20.0		
Northrop Grumman	LN-1000G INS	21.6		
Collins Aerospace	VIR-351 NAV Receiver	1.5		
Collins Aerospace	AN/ARC-210 UHF	12.2		
Collins Aerospace	AN/ARC-186 VHF	14.0		
L3Harris	KGV-135A Voice Encryption	18.0		
Collins Aerospace	MIDS JTRS (Link 16)	42.4		

Table 37 Integrated Electronic Warfare System

Manufacturer	Product Name	Weight (lbs)	Volume (in^3)	Cost (2025 USD)
Northrop Grumman	AN/AAR-56 Missile Warning System	24.0	5184.0 [1]	819,000 [1]
L3Harris	AN/ALQ-214 EWS	285.0		
BAE Systems	AN/ALE-47 Countermeasures Dispenser System	40.0		

15. Ordnance, MR

The ordnance configuration for our aircraft primarily involves the employment of two AIM-120 missiles, strategically positioned with their center of gravity at 310.4 in aft from the nose. The hard point locations were specifically chosen to accommodate not only these missiles but also to allow for the interchangeability with fuel tanks, aligning with alternative operational concepts that include refueling services during operations.

While the loadout of two missiles might seem limited, it is integral to the aircraft's design to operate within a larger fleet context. Each aircraft is designed to work in concert with one to three other identical units, each also equipped with two AIM-120s. This strategy enhances the collective defensive and offensive capabilities, allowing for coordinated, large-scale mission execution.

Additionally, ordnance safety considerations include emergency release systems to ensure quick and safe disengagement when necessary.

16. Survivability, CG

As the Lobo is a remote piloted interceptor and the loss of life is not a concern when engaging in combat, the Lobo was designed to defend itself against common ordinances, but not advanced threats. Because the Lobo is designed to be a low-cost aircraft, advanced countermeasures were traded for a reduced cost. Additionally, when flying in a fleet formation, it is a known possibility that one aircraft may need to provide a distraction for an advanced fighter which will allow the other aircraft to engage. The possibility of the Lobo being neutralized in combat is not a concern when in a fleet formation will be utilized against modern and advanced threats. Understanding that the Lobo is meant to be operated only when a threat appears, and that it will be primarily flown in friendly airspace, it was determined that cost of highly advanced countermeasures was not justifiable.

However, cost-effective solutions were implemented to enhance the Lobo's survivability chances. The Lobo will carry flare and chaff countermeasures, carrying 60 of each countermeasure, the same as the F/A-18 E/F [46]. The distribution of these countermeasures can be configured based on the threats the Lobo is more likely to encounter. To dispense these countermeasures, an AN/ALE 47 dispenser will be used. This dispenser is currently utilized by a multitude of United States' fighter aircraft and will allow for seamless integration of the Lobo into existing Air Force bases [47]. The Lobo utilizes four dispensers, placed below the inlets on the underside of the aircraft, allowing for ease of deployment of necessary countermeasures when pitching up to evade a missile. By carrying both flare and chaff, the Lobo can defend against both heat-seeking and radar-guided missiles. Additionally, the Lobo's SABR radar and onboard AN/ALQ-214 jammer can protect the Lobo from radar-guided technology present in advanced missiles, with the chaff being designed for redundancy for increased chances of survival [45] [48].

While the Lobo's role as a homeland defense interceptor does not require considerable survivability measures, other future variants of the Lobo may require these measures. If a future Lobo variant is used for carrier-based operations or an active combat area, a alternative use case would allow the Lobo to serve as a multi-role aircraft, for example as an aerial refueling aircraft in the presence of adversary air defense systems. If the Lobo is desired to fly in a high-risk airspace, future variants of the Lobo can tow an RF Decoy, which will mimic the Lobo's radar signature behind the aircraft, protecting it further from radar guided missiles.

17. Repair and Maintenance, NB

Repair and maintenance is a major factor in the operation and operational cost of an aircraft. All maintenance procedures will be compliant with MIL 516C part 16. This maintenance will include scheduled maintenance that takes care of normal service and inspections. There will also be unscheduled maintenance. Keeping both aspects of maintenance at a minimum will keep operational costs down and keep down the ratio of man hours to flight hours. At this point in the design stage, it is appropriate to begin a similarity analysis of what different aircraft and organizations have as maintenance procedures. A concise table shown in Fig. 38 shows a rough estimate of what checks should

consist of and when they should occur[49]. Inspections will be consistent to satisfy MIL 516C part 16.2.4. Unscheduled maintenance, by definition, is unpredictable. There is no schedule in which it occurs. Efforts will be made to minimize unexpected issues. As the design will be manufactured, an emphasis will be placed such that parts will be easily replaceable if repairs are not economical or practical. It can become increasingly difficult to repair an airplane that is built around itself. Another method that could be used to predict non-routine maintenance would be to create a digital twin of the aircraft. The idea is that this digital twin is created and anything that happens to the real aircraft will happen in simulation to the digital twin. This allows there to be a higher level of predictability to catch issues before they arise.

Table 38 Maintenance Timetable

Check Name	Maintenance Man Hours	Frequency
Line Check	2	1-6 FH
A-Check	10-20	80-100 FH
B-Check	100-300	500-600 FH
A-Check	10,000-30,000	2 years
A-Check	50,000	6 years

It is also important to design the aircraft such that it can be maintained. This includes the placement of maintenance hatches and access panels. These panels will be located such that any internal component that will need maintenance will need an access panel close enough to be able service the component. There will be several large access panels around the engine. This is because the engine will need the most maintenance. Additionally, there will need to be panels near any of the systems. There needs to be one to give access to the radar. There will need to be periodic access panels in the wings and fuselage to inspect internal structures. A good rule of thumb is that if a component can be expected to be worked on or replaced, there needs to be an access panel to do so. This is shown in Fig. 78. One other component to think about is the use of ground equipment designed for other common aircraft. For example, the Lobo landing gear was sized to make sure that the Lobo could use the same engine removal cart as the F-16. This is possible because the engine height on the F-16 is about 50 inches high and the Lobo is 60 inches high. This means that surplus equipment will be available for use on the aircraft.

((a)) Top view. **((b)) Side view.**

Fig. 78 Maintenance hatches.

18. Cost Analysis, AM

A. Research Development Test and Evaluation (RDT&E) and Flyaway Cost

In order to make a preliminary estimate of the aircraft's RDT&E and Flyaway costs, the RAND DAPCA IV Model, taken from Raymer 18.4.2 [5], was employed. The DAPCA model was initially chosen because it required parameters that were available during the preliminary design phase. The DAPCA model estimates the cost in 2012 dollars, so an inflation factor derived from the consumer price index [50] was applied to adjust to 2025 dollars in accordance with the RFP requirements. The model parameters and output RDTE + Flyaway cost can be found on Table 39(a). The engine cost was derived from the cost of a contract made with GE for 329 units of the F110-GE-129 engine for $1.59 Billion [51], and the avionics cost was provided by systems and derived from the cost of government furnished equipment as outlined in the RFP [1]. Additionally, a detailed cost breakdown can be seen in Fig. 79.

To test the accuracy of the DAPCA model as well as to improve the RDT&E estimate, the Roskam cost model [52] was implemented with the same initial parameters, alongside some additional parameters, which serve to account for more cost variables. These additional parameters are listed in Table 39(b). Additionally, weights dependent on the amount of composite and titanium used in the airframe were applied to the Engineering, Tooling, Manufacturing, and Quality Control hours as well as cost of materials for the Roskam model to further improve the model's accuracy. These added weights drove the Roskam Model's predicted RDTE + Flyaway cost up from $22.3M to $23.5M. The weights were derived from [53]. A cost breakdown of the Roskam model's RDT&E cost is shown in Fig. 80. Sine the Roskam model has a higher estimated RDTE + Flyaway cost this model was used throughout the rest of the cost analysis.

Table 39 Cost Model Parameters

((a)) DAPCA IV Parameters

Inflation Factor	1.4
Empty Weight (lb)	15,570
Max Velocity (kt)	922
Production Quantity	1,000
Number of Flight Test Vehicles	6
Number of Engines	1
Avionics Cost	$3,441,000
Engine Cost	$4,802,000
RDT&E + Flyaway (2025 Dollars)	$23,185,000

((b)) Roskam Cost Model Additional Parameters

Inflation Factor	2.49
Difficulty Factor	2
CAD Factor	0.8
Number of Static Flight Test Airplanes Built	2
Number of Flight Test Vehicles	6
Weight of Wheels, Brakes, Tires, Tubes	600 lb
Weight of Engine	3,940 lb
Weight of Starter	40 lb
Weight of Cooling Fluid	20 lb
Weight of Fuel Cells	630 lb
Weight of Batteries, Electrical Power Suppler, and Power Conversion	385 lb
Weight of Instruments, Avionics, Electronic Equipment	600 lb
Weight of Armament and Fire Control Systems	700 lb
Weight of Airconditioning Units and Fluid	140 lb
Fiberglass Percent Airframe Weight	3.4%
Carbon Fiber Percent Airframe Weight	10.9%
Titanium Percent Airframe Weight	20.5%
RDT&E (2025 Dollars)	$23,965,000

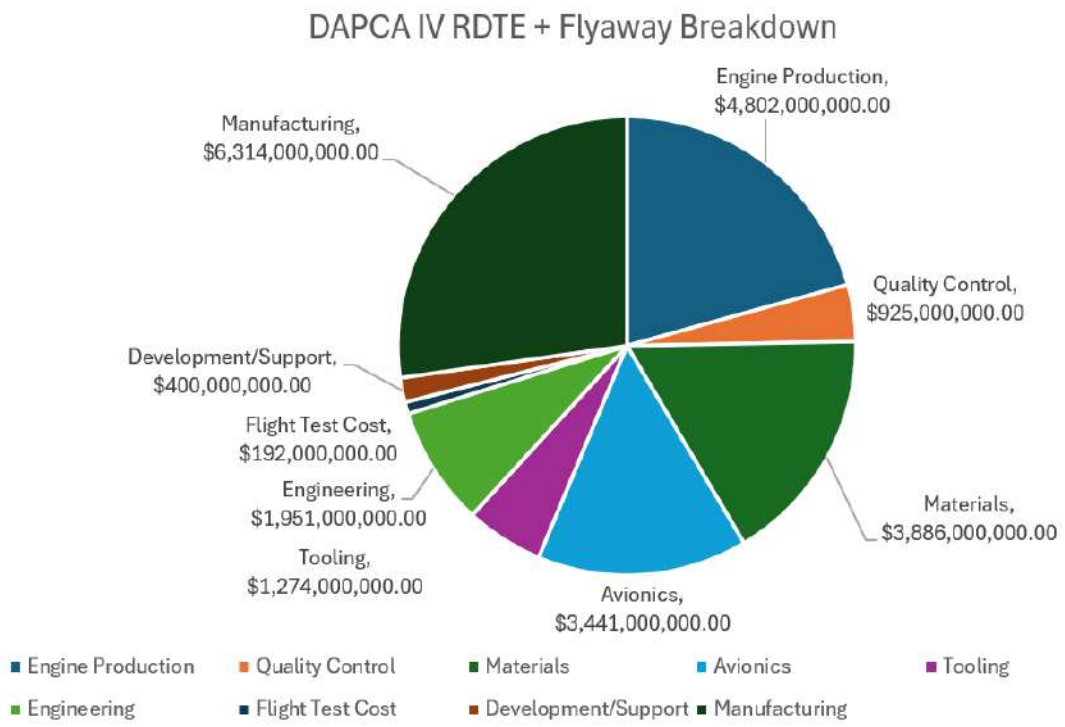

Fig. 79 DAPCA IV cost model breakdown (2025 Dollars).

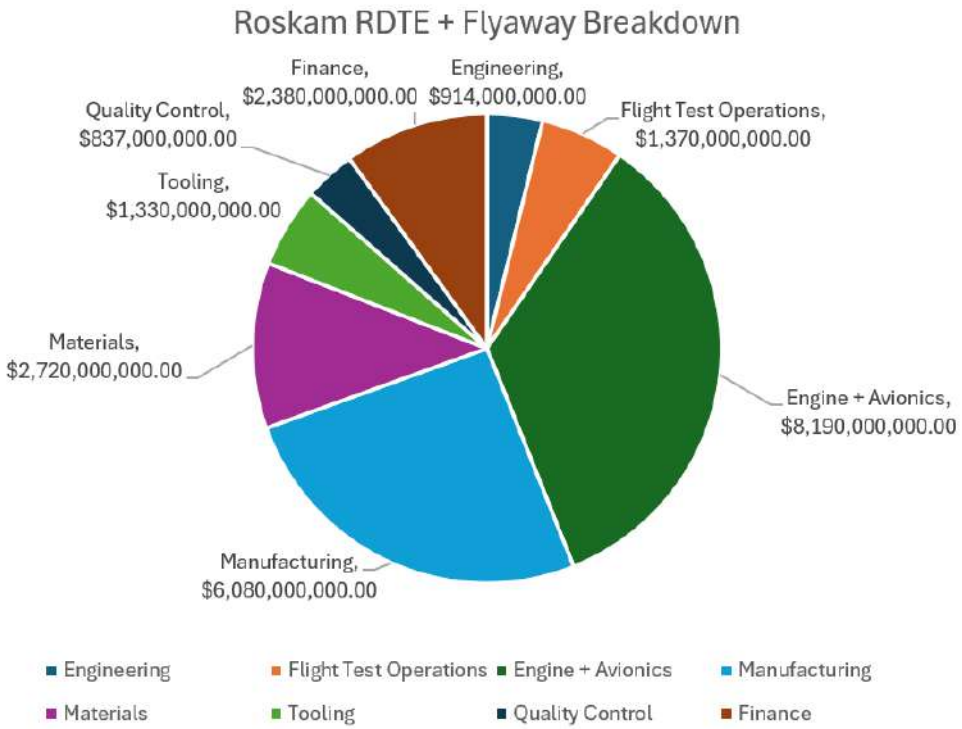

Fig. 80 Roskam cost model breakdown (2025 Dollars).

B. Operating Costs

The Roskam model section for estimating the operating costs of military airplanes was utilized to create an operating cost breakdown for the team's aircraft, as well as to provide an accurate estimate to the overall and unit life cycle cost. The operating costs for the aircraft program are made up by the program fuel, oil, and lubrication cost, the program direct personnel cost, the cost of indirect personnel, the cost of maintenance and consumable materials, the cost of spares, the cost associated with depots, and a factor for miscellaneous cost, which include the cost to acquire technical data for maintenance, the training, training data, and training equipment costs, and the costs for support equipment.

The Roskam model was used to determine the total operating costs, based primarily on the Defensive Counter-Air Patrol Mission in the RFP [1]. This mission was chosen as the baseline as it would likely incur the highest Operating costs due to the four hour air patrol portion of the mission expended a large amount of fuel. Additionally, the mission calls for the aircraft to fire all missiles, with the missiles being a significant expense. Figure 81 shows a breakdown of the individual components of operating cost as well as operating cost per hour and a comparison to the F-16C. The price of fuel was estimated at $6.31/gal, the crew pay was approximated as $115,000, with one remote pilot. Additionally it was assumed that the aircraft would have a 20 year service life, and operate for about 300 flight hours a year, with each mission averaging about five hours. The loss rate was assumed to be similar to the F-15. This high loss rate would be due to the fact that most interception missions will occur around the coast, most likely over the open ocean, in which case the light interceptor aircraft will likely become unrecoverable once damage incurs.

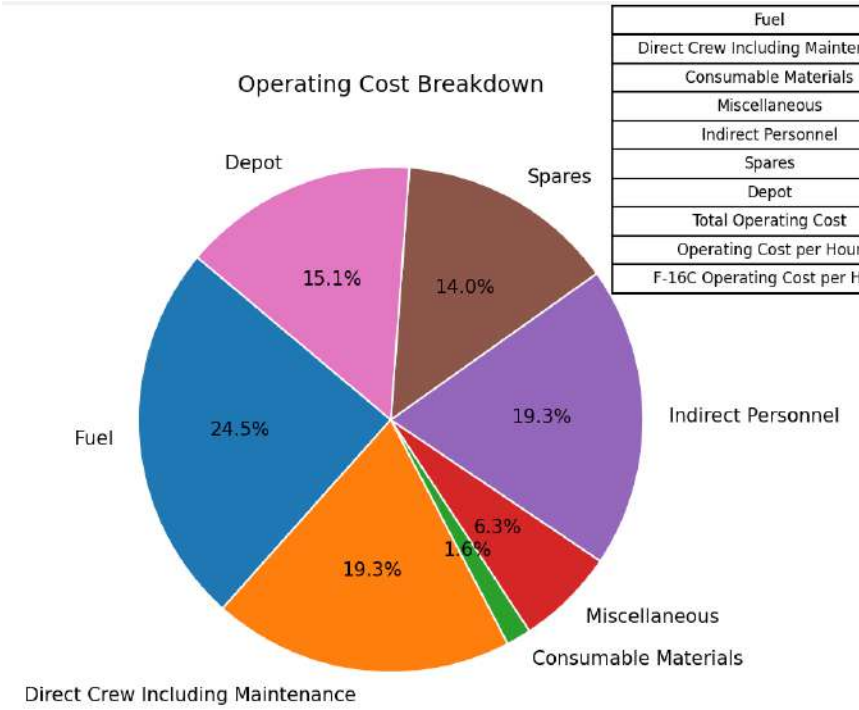

Fuel	$14,000,000,000
Direct Crew Including Maintenance	$11,000,000,000
Consumable Materials	$910,000,000
Miscellaneous	$3,600,000,000
Indirect Personnel	$11,000,000,000
Spares	$8,000,000,000
Depot	$8,600,000,000
Total Operating Cost	$57,000,000,000
Operating Cost per Hour	$12,300
F-16C Operating Cost per Hour	$13,200

Fig. 81 Operating cost breakdown.

C. Life cycle Cost

Table 40 shows the life cycle cost breakdown of the aircraft using the Roskam cost model. In order to further minimize life cycle costs, the team could incorporate advanced manufacturing techniques such as 3D printing of titanium to significantly reduce manufacturing hours. The production quantity was varied with life cycle and unit cost and the result are given in Fig. 82.

Table 40 Roskam Model Per Unit Costs

Life Cycle Cost	87,400,000
RDT&E	2,850,000
Acquisition Cost	26,000,000
Operating Cost	58,000,000
Disposal Cost	870,000
Unit Cost	23,541,000

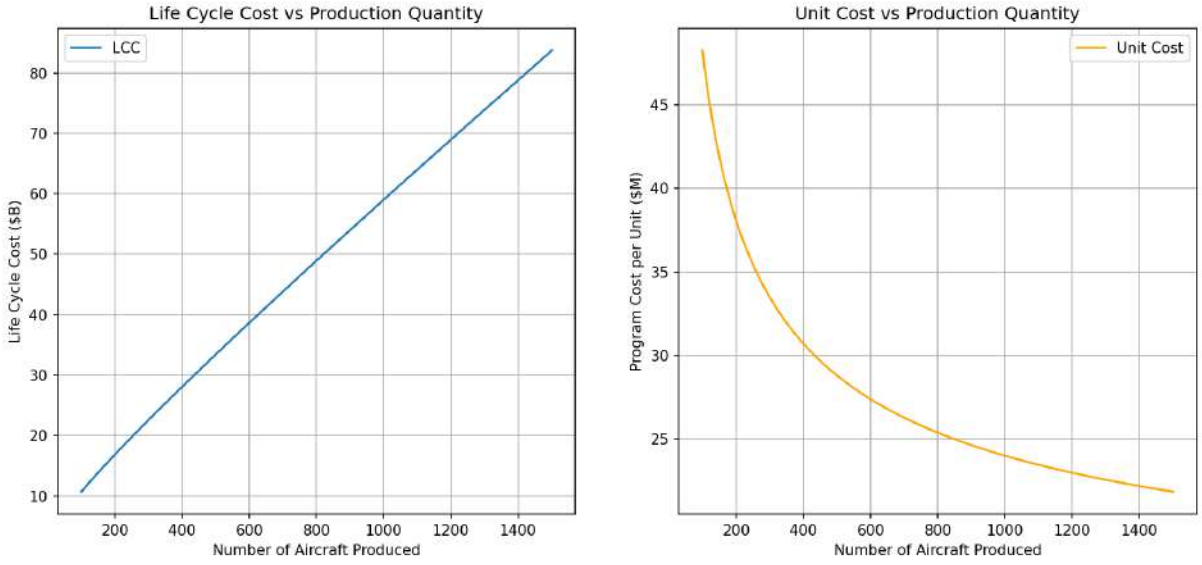

Fig. 82 RDTE and unit cost variation with production quantity.

D. Titanium Trade Study

Utilizing the methods from [53], A trade study was conducted to see how much more titanium could be applied to the airframe while still remaining under the $25M Flyaway cost constraint outlined in the RFP [1]. From Fig. 83, it was found that an estimated 2,400 lb of aluminum could be replaced by titanium. This added titanium would serve to reinforce the airframe structure and increase the aircraft's load limits.

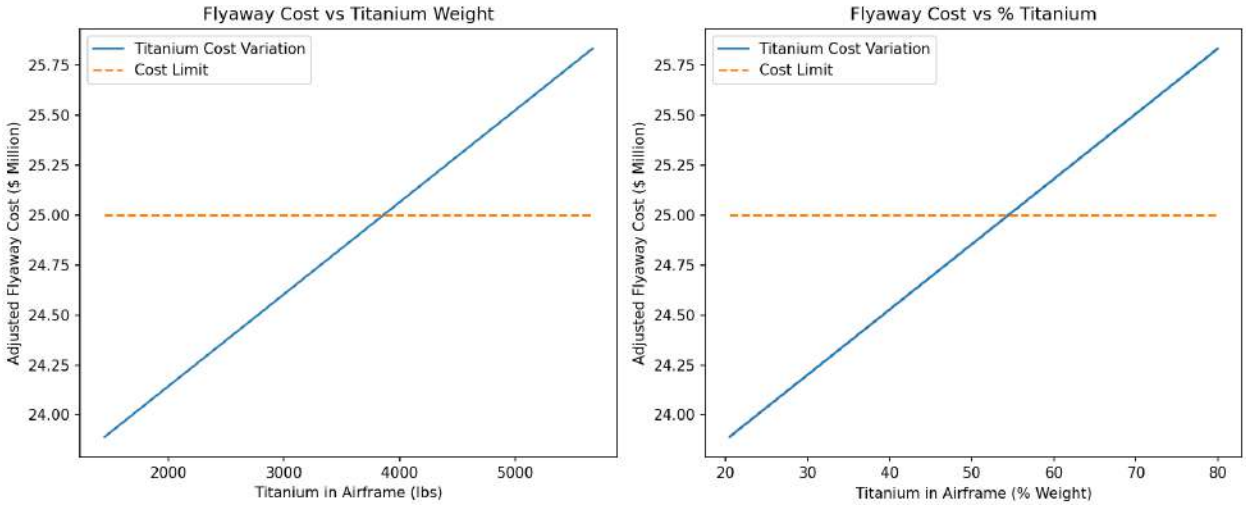

Fig. 83 Titanium trade study.

19. Conclusion

The Lobo was developed in response to a need for a low-cost, rapidly deployable homeland defense interceptor. Designed for quick response to threats over domestic airspace, the Lobo performs it's required missions at a highly affordable flyaway cost of $23.5M. The team's primary design objectives included achieving Mach 1.6 dash at 35,000 ft, Mach 1.2 dash capability at sea level, 4-hour combat air patrol endurance, and remote piloting functionality, all while staying below a unit flyaway cost of $25 million.

The finalized configuration features a single-engine, swept-wing design powered by the F110-GE-129 engine, with a blended fuselage optimized for reduced drag and internal fuel volume. The aircraft integrates two AIM-120 missiles, robust sensor and communication systems, and a remotely piloted avionics suite for real-time control and situational awareness.

The Lobo's primary differentiators are its cost-effective use of COTS systems, simplified maintenance architecture, and focus on remotely piloted operations with limited autonomy. These design choices reduce development and life cycle costs and make the aircraft a flexible platform to deploy in fleet formations. In the future, by enabling support for multiple mission types through the design of variants, the Lobo will reduce the need for separate specialized aircraft, thereby streamlining training, maintenance, and logistical demands.

Several design challenges were encountered, including CG management across fuel burn, minimizing structural deformation under 10.5g loads, and integrating compact landing gear within the fuselage. Recommendations for future study include refining structural load paths via high-fidelity FEA simulations, developing aerial refueling compatibility, and expanding Lobo's operational envelope for maritime or carrier-based variants.

The Lobo demonstrates that modern intercept capabilities can be achieved without compromising cost, adaptability, or mission readiness.

References

[1] AIAA, "Homeland Defense Interceptor Request for Proposal," https://www.aiaa.org/docs/default-source/uploadedfiles/membership-and-communities/university-%students/design-competitions/undergraduate-team-aircraft-design-2024-2025-homeland-defense-interceptor.pdf, 2024. Accessed: 2025-02-10.

[2] P. Jackson, L. P., K. Munson, *Jane's All the World's Aircraft 99th Edition*, Jane's Information Group Ltd., 2008.

[3] J. W. R. Taylor, K. M., *Jane's All the World's Aircraft 73rd Edition*, Jane's Publishing Company, 1982.

[4] Anduril Industries, "Fury: Anduril's Long-Endurance, Multi-Mission Unmanned Aircraft," , 2024. URL https://www.anduril.com/fury/, accessed: 2024-09-08.

[5] Raymer, D. P., *Aircraft Design: A Conceptual Approach*, AIAA educational series, American Institute of Aeronautics and Astronautics, 2018.

[6] Ackers, D. J. R., *PART VII: AIRPLANE FLIGHT DYNAMICS AND AUTOMATIC FLIGHT CONTROLS*, Roskam Aviation and Engineering Corporation, 2001.

[7] Ackers, D. J. R., *PART VI: Preliminary Calculation of Aerodynamic, Thrust and Power Characteristics*, Roskam Aviation and Engineering Corporation, 2004.

[8] Nicolai, L., and Carichner, G., *Fundamentals of Aircraft and Airship Design. Volume 1*, AIAA educational series, American Institute of Aeronautics and Astronautics, 2010.

[9] Meier, N., "Military Turbojet/Turbofan Specifications," , 2021. URL https://www.jet-engine.net/miltfspec.htm, accessed: 2025-02-13.

[10] Élodie Roux, *Turbofan and Turbojet Engines Database Handbook*, Éditions Élodie Roux, 7 rue Carrière, 31700 Blagnac, France, 2007. Printed by Lulu.com; internal reference document.

[11] GE Aviation, "F110-GE-132 Turbofan Engine Data Sheet," https://www.geaerospace.com/sites/default/files/datasheet-F110-GE-132.pdf, Jun. 2014. AE-44043B (06/14); Printed in U.S.A.; internal reference document.

[12] GE Aerospace, "F110-GE-129 Engine Datasheet," , 2025. URL https://www.geaerospace.com/sites/default/files/datasheet-F110-GE-129.pdf, accessed: 2025-03-09.

[13] Lockheed Martin Corporation, "HAF Series Aircraft F-16C/D Blocks 50 and 52+ Flight Manual Supplement," , 2002. URL https://info.publicintelligence.net/HAF-F16-Supplement.pdf, technical Order No. F33657-90-C-2002.

[14] Powrie, H. E. G., and Novis, A., "Gas Path Debris Monitoring for F-35 Joint Strike Fighter Propulsion System PHM," *Proceedings of the Prognostics and Health Management Conference for Aerospace Systems*, 2006. Figure 5: IDMS/EDMS Hardware Configuration for F-35; accessed via ResearchGate.

[15] Ibrahim, I. H., "Fluid Flow Studies of the F-5E and F-16 Inlet Ducts," Master's thesis, Nanyang Technological University, 2008. URL https://dr.ntu.edu.sg/bitstream/10356/14581/1/Fluid%20Flow%20Studies%20Of%20The%20F-5E%20and%20F-16%20Inlet%20Ducts.pdf, accessed: 2025-05-07.

[16] Selig, M., "UIUC Airfoil Data Site," , Accessed 13 February 2025. URL https://m-selig.ae.illinois.edu/ads.html/.

[17] Hoerner, S. F., *Fluid-Dynamic Drag*, Hoerner Fluid Dynamics, 1965.

[18] Massie, W., "Delta method, an empirical drag buildup technique," *NASA Technical Reports*, 1978. URL https://ntrs.nasa.gov/api/citations/19790009630/downloads/19790009630.pdf.

[19] Nelson, D. R. C., *Flight Stability and Automatic Control*, Department of Aerospace and Mechanical Engineering University of Notre Dame, 1998.

[20] "Aluminum 6061-T6: 6061-T651," , retrieved 2 February 2025. URL https://web.archive.org/web/20250126104629/https://asm.matweb.com/search/specificmaterial.asp?bassnum=ma6061t6.

[21] "Cost of Aluminum 6061 Per Kg in 2024: An Overview of Pricing and Market Trends," , 8 October 2024. URL https://www.unionaluminium.com/news/industry_news/cost_of_aluminum_6061_per_kg_in_2024_an_overview_of_pricing_and_market_trends.html#:~:text=As%20of%20early%202024%2C%20the%20average%20cost%20of,applied%2C%20bringing%20the%20cost%20per%20kg%20slightly%20lower.

[22] "7075 aluminum plate," , retrieved 5 February 2025. URL https://www.enzemfg.com/7075-aluminum-alloy/.

[23] Cavallo, C., "All About 4130 Steel (Properties, Strengths, and Uses," , 12 August 2020. URL https://www.thomasnet.com/articles/metals-metal-products/all-about-4130-steel-properties-strength-and-uses/?msockid=34a67feb5452620324a76af65052609b.

[24] "AISI 1045 Carbon Steel (UNS G10450)," , 17 June 2013. URL https://www.azom.com/article.aspx?ArticleID=9153.

[25] "ASTM SAE AISI 1045 Carbon Steel Heat Treatment, Chemical Composition, Properties," , retrieved 8 February 2025. URL https://www.theworldmaterial.com/astm-sae-aisi-1045-carbon-steel-material/.

[26] "Grade 1045 Steel," , retrieved 8 February 2025. URL https://www.mcmaster.com/products/grade-1045-steel/steel~/.

[27] "Carbon Fiber Selector Guide," , retrieved 6 February 2025. URL https://www.toraycma.com/wp-content/uploads/Carbon-Fiber-Selector-Guide.pdf.

[28] Naskar, A., "Carbon Fiber and Composite Manufacturing for Hydrogen Storage Tanks," , 25 May 2022. URL https://www.energy.gov/sites/default/files/2022-07/h2-mach-7-naskar.pdf.

[29] de Naoum, K., "All About Fiberglass," , 18 October 2023. URL https://www.xometry.com/resources/materials/what-is-fiberglass/.

[30] "Fiberglass Cost Calculator for Any Project," , retrieved 13 February 2025. URL https://fiberglass-engineering.com/fiberglass-cost-calculator/.

[31] Ackers, D. J. R., *PART V: COMPONENT WEIGHT ESTIMATION*, Roskam Aviation and Engineering Corporation, 1990.

[32] "2022 Goodyear Aviation Data Book," , 2022. URL https://www.goodyearaviation.com/resources/pdf/Aviation-Databook-2022.pdf.

[33] "Code of Federal Regulations," Vol. 14, 2025. URL https://www.ecfr.gov/current/title-14.

[34] Tanks, R. A. F., "Ballistic Treated Fuel Tanks," , retrieved 6 May 2025. URL https://atlinc.com/pdfs/Ballistic/balllit.pdf?file=pdfs/Ballistic/balllit.pdf.

[35] RADCO, "A Brief History of U.S. Military Aviation Hydraulic Fluids." , retrieved 5 May 2025. URL https://www.radcoind.com/blog-post/a-brief-history-of-u-s-military-aviation-hydraulic-fluids/.

[36] Ian Moir, A. S., *Third Edition Aircraft Systems*, John Wiley Sons Ltd., 2008.

[37] Quinty, G., "Thermal Management Techniques in Avionics Cooling," , Accessed 10 February 2025. URL https://www.mobilityengineeringtech.com/component/content/article/39672-thermal-management-techniques-in-avionics-cooling.

[38] Bellamy, W., "Liquid Cooling: Thermally Managing Next-Generation Avionics," , Accessed 10 February 2025. URL https://interactive.aviationtoday.com/avionicsmagazine/april-2019/liquid-cooling-thermally-managing-next-generation-avionics/.

[39] Proteus, "PAO (polyalphaolefin)," , Accessed 11 February 2025. URL https://www.proteusind.com/pao-polyalphaolefin/.

[40] AMETEK, "Liquid Cooling Systems," , Accessed 10 February 2025. URL https://www.pd-tech.com/products/thermal-management-systems.

[41] Grumman, N., "F-25 DAS," , Accessed 1 March 2025. URL https://www.youtube.com/watch?v=e1NrFZddihQ.

[42] Atomics, G., "Block 30 Ground Control Station," , retrieved 6 May 2025. URL https://www.ga-asi.com/ground-control-stations/block-30.

[43] Force, U. S. A., "REMOTELY PILOTED AIRCRAFT (RPA) SENSOR OPERATOR," , retrieved 6 May 2025. URL https://www.airforce.com/careers/aviation-and-flight/remotely-piloted-aircraft-rpa-sensor-operator.

[44] MISO, R., "Difference Between AESA Radar And PESA Radar," , 7 August 2023. URL https://www.rf-miso.com/news/difference-between-aesa-radar-and-pesa-radar-aesa-radar-vs-pesa-radar-2/.

[45] Grumman, N., "Active Electronically Scanned Array (AESA) Radars," , Accessed 10 March 2025. URL https://www.northropgrumman.com/what-we-do/air/active-electronically-scanned-array-aesa-radars.

[46] Newdick, T., "The Instant Flares are Released from an F/A-18 Hornet Seen in Incredible Photo," , 2018. URL https://www.twz.com/the-instant-flares-are-released-from-an-f-a-18-hornet-seen-in-incredible-photo.

[47] Systems, B., "ALE-47 Airborne Countermeasures Dispenser System," , retrieved 28 April 2025. URL https://www.twz.com/the-instant-flares-are-released-from-an-f-a-18-hornet-seen-in-incredible-photo.

[48] L3Harris, "AN/ALQ-214," , retrieved 5 May 2025. URL https://www.l3harris.com/sites/default/files/2020-08/l3harris-an-alq-214-idecm-sell-sheet-sas.pdf.

[49] for Business Innovation Skills, D., "UK Aerospace Maintenance, Repair, Overhaul Logistics Industry Analysis," *BIS Research Paper*, Vol. 275, 2016. URL https://assets.publishing.service.gov.uk/media/5a75b99fed915d506ee8105a/bis-16-132-uk-mrol-analysis.pdf.

[50] "CPI Inflation Calculator," , retrieved 7 March 2025. URL https://www.bls.gov/data/inflation_calculator.htm.

[51] Feagin, R., and Morrison, W., "GE awarded $1.6 billion contract to power full U.S. Air Force F-15EX fleet," 2021. URL https://www.geaerospace.com/news/press-releases/defense-engines/ge-awarded-16-billion-contract-power-full-us-air-force-f-15ex-fleet.

[52] Ackers, D. J. R., *PART VIII: AIRPLANE COST ESTIMATION: DESIGN, DEVELOPMENT, MANUFACTURING AND OPERATING*, Roskam Aviation and Engineering Corporation, 1990.

[53] Shen, A. W., "Analysis of the influence of advanced materials for aerospace products RD and manufacturing cost," *IOP Conf*, 2015. URL https://iopscience.iop.org/article/10.1088/1757-899X/103/1/012004/pdf.